ABSTRACT

Dissertation Title: Electronically Tailored Functionalization of Carbon Nanotubes

Yanmei Piao, Doctor of Philosophy, 2014

Dissertation Directed By: Professor YuHuang Wang
Department of Chemistry and Biochemistry

Carbon nanotubes (CNTs) were chemically tailored on the electronic level to enhance their optical and electrical properties.

Incorporation of sp^3 defects into the sidewalls of CNTs significantly improved quantum efficiency of CNT photoluminescence (PL). Nanotube PL is intrinsically inefficient, usually less than 1%, due to the presence of dark excitons. This low efficiency makes nanotubes impractical for many applications, especially bio-imaging and optoelectronics. The nanotube PL was increased by up to 28 times through the chemical creation of a new defect induced state. This new state is optically allowed and resides below the predicted energy levels of the dark excitons, allowing the dark excitons to be harvested from this new defect state. Emission from the new state

generates a distinct, structure-specific, and chemically tunable photoluminescence peak. This new peak is red-shifted by as much as 254 meV from the original excitonic transition and located within the tissue transparent window, which merits bio-imaging and bio-sensing. This work opens the door to harnessing dark excitons and lays the foundation for chemical control of defect quantum states in low dimensional carbon materials.

Unlike atom-thick materials such as SWCNTs and graphene which are prone to chemical attacks because all constituent atoms are exposed, double-walled carbon nanotubes (DWCNTs) provide a chemically tailorable surface and an inner-tube with intact electronic properties. Even when the outer walls were selectively functionalized up to 6.9% (percent of carbon that are covalently modified), the inner tubes were electrically intact. Correlated Raman and optical absorption spectroscopy unambiguously confirm that the covalent modification was outer wall-selective. Nearly 50% of the electrical conductivity was retained in thin films of covalently functionalized nanotubes owing to the protected inner-tube conducting channels. Lacking such channels, SWCNTs became insulators after similar functionalization. Further experiments demonstrated that the covalently attached aryl groups could be selectively removed by optical annealing. These results suggest the possibility of high performance DWCNT electronics with important capabilities of tailored surface chemistry on the outer walls while the inner walls are chemically protected.

ELECTRONICALLY TAILORED FUNCTIONALIZATION OF CARBON NANOTUBES.

By

Yanmei Piao

Dissertation submitted to the Faculty of the Graduate School of the
University of Maryland, College Park, in partial fulfillment
of the requirements for the degree of
Doctor of Philosophy
2013

Advisory Committee:
Professor Wang, YuHuang, Chair
Professor Blough, Neil
Professor Lee, Sang Bok
Professor Reutt-Robey, Janice
Dean's Representative: Professor Cumings, John

To my parents and grandmother

Acknowledgements

Most of all, I would like to express my sincere gratitude to my advisor and mentor Professor YuHuang Wang for his continuous support over the past few years. I can't thank him enough for his belief in me when I was lost in the study and research and for giving me the opportunity to work on the cutting edge research topics with him. His continuous support made me find the joy of research and his enthusiasm and insights for the science will inspire me throughout my career.

I would like to thank Professor Neil Blough, Professor Sang Bok Lee, Professor Janice Reutt-Robey and Professor John Cumings for kindly accepting to serve on my committee and for their suggestions on the research and supports along the way.

I thank Brendan Meany for his excellent technique and hard work in preparing purified carbon nanotube samples. I thank Brendan, Lyndsey Powell and Dr. ChuanFu Sun for their careful editing of my thesis. I thank Dr. Alexandra Brozena, Dr. Jarrett Leeds, Dr Yin Zhang and Hyejin Kwon for the inspiring discussions and help along my graduate studies. I thank Dr. Shunliu Deng, Dr. Cai Shen, Dr. ChienFu Chen, Dr. Jia Huang and Dr. Chunyan Wang for their advice on my research on diverse topics. I would like to thank all the other Wang group members and alumni; I couldn't have come this far without their support and help.

I thank Professor Mark Hersam and Dr. Alexander Green for the preparation of double-walled carbon nanotube samples that can't be obtained anywhere else. I thank Professor George Schatz and Nichols Valley for the theoretical calculations that have greatly enriched my research. I thank Dr. Karen Gaskell for her help with Raman and XPS. I thank all my other collaborators for their support.

I thank all the friends I met in Maryland and I wish them a bright future.

Finally, I would like to thank my parents and grandmother for their unconditional love and support.

Contents

List of Figures

List of Tables

1 Introduction

1.1 Introduction to carbon nanotubes

Single-walled carbon nanotubes (SWCNT) feature a cylindrical, honeycomb lattice that is composed of entirely sp^2 bonded carbons. The typical diameter of a SWCNT is ~1 nm yet its length can be microns to a few centimeters. Due to their unique structures, SWCNTs exhibit extraordinary optical and electronic properties[1], tremendous mechanical strength and flexibility[2,3], superior electrical[4] and thermal conductivity[5,6] and high chemical stability[7,8]. Since their discovery in 1993[9,10], SWCNTs have found interesting applications in a variety of areas[11], for example, electronic[12,13,14] and optical devices[15–17], medicine,[18] and industrial composites[19,20].

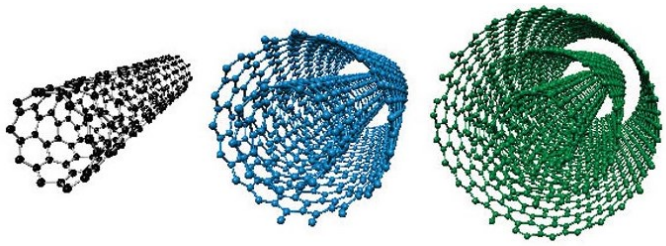

Figure 1-1 Molecular models of single-, double- and multi-walled carbon nanotubes

The intensive research on CNTs has already entered its third decade. Improved production techniques of carbon nanotubes as well as a much better understanding of their physical properties have helped make some of the proposed applications become a reality. Examples include CNT atomic force microscopy (AFM) tips[21,22], lithium[23] and hydrogen[24] storage, bio-imaging/bio-sensors[18], and field effect transistors (FET)[12].

However, creating applications with marketability remain challenging. First, none of the existing production techniques produce high purity, single chirality SWCNTs required for advanced applications such as high-performance FETs and bio-sensors. Another obstacle is the extremely low fluorescence quantum efficiency of SWCNTs, which is a deal breaker for their applications in bio-imaging and opto-electronics. Lack of SWCNT solubility in conventional solvents is a fundamental challenge for many applications. To make SWCNT water soluble or environmentally compatible, covalent modification is desirable; however, it also introduces defects in the sp^2 lattice which can destroy their optoelectronic properties and weaken the mechanical strength.

Over the years, tremendous effort has been made to overcome these obstacles towards SWCNT applications. Post-synthesis separation of SWCNTs by electronic types has recently became possible by DNA wrapping[25], size exclusion chromatography,[26] and density gradient ultracentrifugation[27].

Several previous reports have proposed routes to brighten the SWCNT photoluminescence but there are debates. By adding reducing agent and removing the hole-defects on SWCNTs, the Krauss group raised the upper limit of SWCNT quantum yield (QY) by 30%[28]. Papadimitrakopoulos and co-workers claimed that tightly wrapped SWCNTs that are excluded from oxygen exhibit a 20% quantum yield[29]. However none of these achievements provide a satisfactory answer to the low quantum yield issue or a robust proposal to apply brightened SWCNTs in various environments without degradation.

Functionalizing SWCNTs allows for easy manipulations carbon nanotubes such as dispersion in aqueous solvents. However, covalent sidewall functionalization of SWCNTs creates sp^3 defects in the sp^2 carbon lattice, which was long thought to destroy their electrical and optical properties. Therefore, the tradeoff between functionality and electronic properties of SWCNTs has been believed to be unavoidable.

Recently interesting consequences of defects on nanomaterials has begun to draw attention. Due to the low dimensionality, even a single defect can dominate the electron transport properties. Collins et al. demonstrated that a single defect is capable of completely altering the electrical properties of the entire SWCNT[30].

My thesis is directed toward development of chemically tailored CNTs with enhanced, or otherwise unattainable, optical and electrical properties with respect to the pristine CNTs. Under this central theme, my thesis work will address the fundamental challenges of SWCNTs by controlled sidewall functionalization for improved material properties. Chapter 2 and 3 illustrate how deliberate and controlled engineering of defects unexpectedly enhanced the optical and electrical properties of CNTs. Incorporation of defects on SWCNTs creates a new optically allowed state that harvests dark excitons leading to a maximum 28-fold brightening of nanotube photoluminescence. In chapters 4 and 5, outer wall selectively functionalized double-walled carbon nanotubes with independent optical and electrical properties from the inner tube will be discussed.

1.1.1 A brief account of the history of carbon nanotubes

The first documented transmission electron microscopy (TEM) images of nano-scale hollow filament of carbon, which closely resemble carbon nanotubes, were reported in 1952 by Radushkevich *et al.*[31,32]. The carbon filaments exhibit a continuous inner cavity with a diameter about 50 nm, which may indicates the synthesis of multi-walled carbon nanotubes. But due to the resolution of the TEM technique, neither the wall numbers nor the fine carbon structure was resolved at that time. After more than three decades, in 1991 Somio Iijima reported images of carbon nanotubes [33]revealing the graphene-like walls of carbon nanotubes, which intrigued the scientific community and significantly boosted interest in carbon nanotubes.

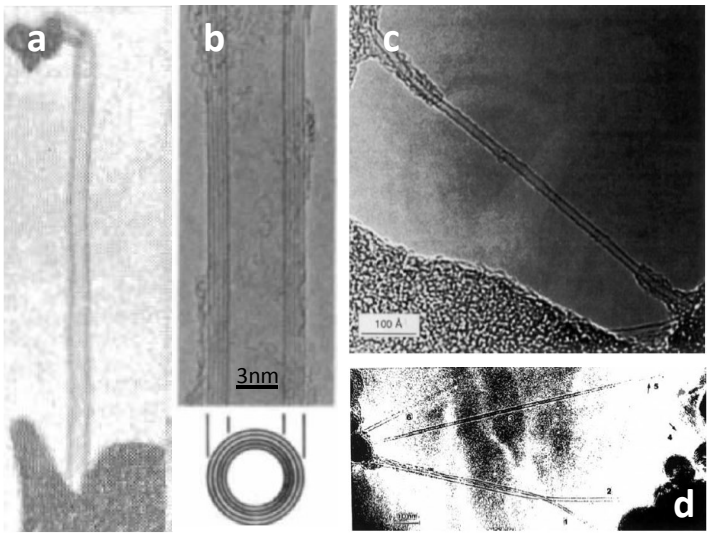

Figure 1-2 (a) The first documented TEM image of a carbon nanotube taken in 1952[32]. Although no scale bar was shown in the original paper, Monthioux *et al.* estimated the diameters of the tube is about 50nm[31]. (b) Five walled carbon nanotube with diameter 6.7 nm reported by Iijima in 1991[33]. (c) and (d) are the first scanning transmission electron microscope (STEM) images of SWCNTs reported in 1993[9,10].

A multi-walled carbon nanotube (MWCNT), as shown in Figure 1-1, consists of multiple layers of coaxial SWCNTs with increasing diameters. The wall-to-wall distance in MWCNTs is approximately 0.34 nm[34,35]. MWCNTs have been widely used in industrial applications due to their mechanical, thermal and electrical properties[19,20], and the fact that MWCNTs are easier to produce compared to that of SWCNTs. However, due to the strong inter-wall interactions, MWCNTs do not possess the distinct electronic and optical properties of SWCNTs.

DWCNTs are coaxial structures composed of exactly two nested SWCNTs[36]. A DWCNT is the simplest MWCNT structure but their properties differ from MWCNT in many aspects. The wall-to-wall distance in a DWCNT varies between 0.33 and 0.42 nm[37]. In addition, the energy dispersion between two walls is less significant than that in the MWCNT, making a DWCNT the perfect system to study interlayer interactions in carbon nanotubes.

Imijia[9] from NEC and Bethune[10] from IBM independently reported back-to-back in *Nature* their findings of SWCNTs in 1993. SWCNTs have unique electronic properties. The earliest prediction of such properties superseded the discovery of SWCNT. Hamada *et al*. computed the electronic band structure of SWCNTs[38]. However, most research in the 1990s was focused on the macroscopic mechanical and electrical properties of CNTs.

Optical spectra of SWCNTs were resolved by Smalley and co-workers using sonication and centrifugation methods to generate a homogeneously dispersed, surfactant-wrapped SWCNT solution which shows discrete absorption and

fluorescence peaks. This work has allowed researchers to explore the optical properties of SWCNTs as macromolecules.

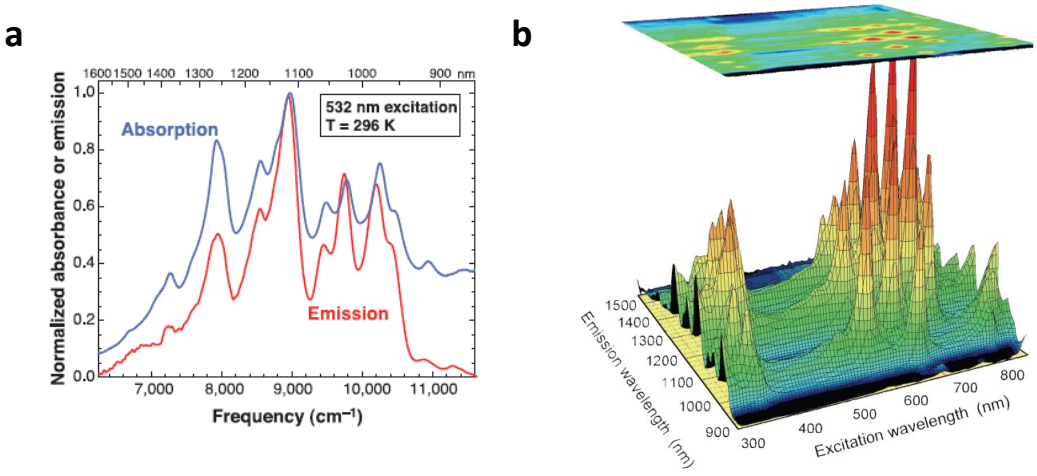

Figure 1-3 (a) Absorption spectrum (blue) and 532 nm excited fluorescence spectrum (red) of individually dispersed SWCNTs solution[39]. (b) 3D fluorescence map of individually dispersed SWCNTs solution. The x and y axes are excitation and emission wavelength, respectively. The z-axis is the intensity of fluorescence[39].

The confirmation of excitons in SWCNTs is another important event in carbon nanotubes development. Exciton – a strongly bound electron-hole pair –arises in SWCNTs due to the one dimensional structure and strong Coulomb interactions[40,41,42]. Nanotube fluorescence was initially attributed to electronic transitions between covalent and valence bands. However, in semiconductor carbon nanotubes, Coulomb interactions are significant due to the 1-D confinement giving rise to strong excitonic effects.

The prediction of excitons in SWCNT[43,44] was unambiguously confirmed by Heinz and co-workers using a two photon absorption method[42]. In this experiment, SWCNTs are excited in a two-photon absorption process using a high power pulse laser

at energy slightly above half the E_{11} transition energy and emission is observed at E_{11}. The result showed two-photon excitation peaks red-shifted substantially with respect to the emission energy which is due to the excitonic nature of the SWCNT.

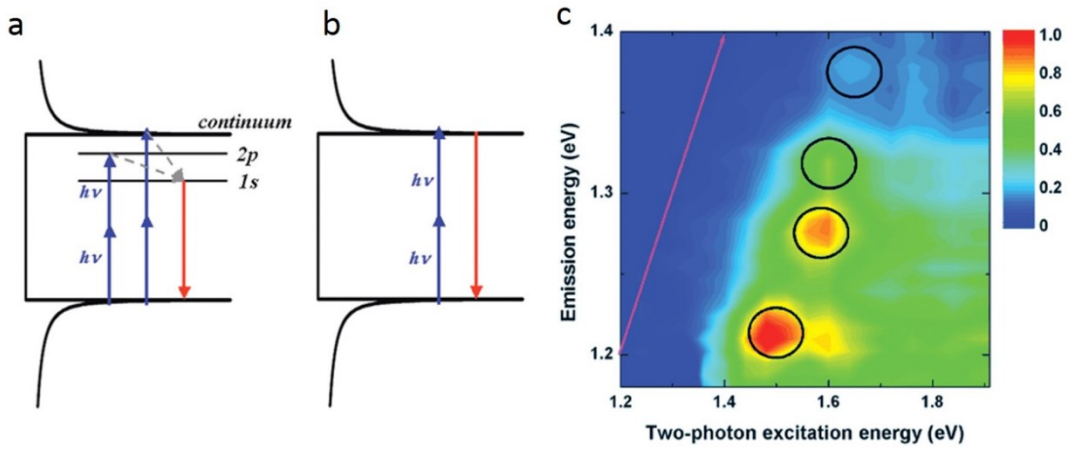

Figure 1-4 Schematic illustration of the SWCNT density of states showing the two-photon absorption and the one-photon emission process with (a) and without (b) excitons. Under two photon excitation the 1s excitation state is forbidden and 2p excitation and continuum states are excited. (c) A contour plot of the two-photon excitation spectra of SWCNTs. The color scale represents the fluorescence intensity. The red line is where emission energy equals excitation energy. The black circles indicate (7,5), (6,5), (8,3) and (9,1) SWCNTs from bottom to top[42].

1.1.2 Synthesis of carbon nanotubes

The most used synthetic methods for carbon nanotubes include high-pressure carbon monoxide disproportionation[45,46,47] (HiPco), catalyst CoMoCAT deposition[48] (CCVD), arc discharge[49], and laser oven[50].

The HiPco method was discovered by the Smalley group in 1998 and is known for producing high quality (>99%), small diameter (~0.8-1.2 nm) SWCNTs.[45] The SWCNTs produced by this method have a broad distribution of diameters. All the above methods donot proved a path to selective synthesis of metallic or semiconductor SWCNTs.

The most common catalysts in CCVD methods is silica supported Co-Mo catalyst (CoMoCAT)[51]. By controlling the cobalt to molybdenum ratio, the diameter of the produced SWCNTs can be controlled within a very narrow range[52]. Particularly (6,5) and (7,6) chirality enriched SWCNT samples have become commercially available through Southwest Nanotechnologies, Inc. The latest CoMoCAT (6,5) sample available contains >40% (6,5) and less than 5% metallic carbon nanotubes.

Arc discharge is the first method used to produce carbon nanotubes. This method tends to produce mixtures of SWCNTs and MWCNTs with large diameters and very few defects due to higher synthesis temperature (~2000°C) compared to CCVD methods (~600-1000°C).

MWCNTs and DWCNTs are produced by CCVD by adjusting temperature, pressure, carbon feedstock material, and catalytic composition. Since all as-synthesized carbon nanotubes are mixture of MWCNTs, SWCNTs and catalytic metals, purification of CNTs is often essential.

1.1.3 Electronic structure of carbon nanotubes

Structurally a SWCNT can be conceptually viewed as a rolled up graphene sheet. Since its discovery, the intriguing structure has sparked tremendous interest. But

the complete understanding of the electronic structure of carbon nanotubes remain incomplete, partly due to a broad range of possibilities in SWCNT structures.

To understand the electronic properties of SWCNTs, an easy way is to compare it with that of graphene[53–55]. Electronically, unlike graphene where charge carriers are mobile on the surface of the whole sheet in any direction[56], the electrons in SWCNT are confined to one dimension. More specifically, the electrons are mobile along the tube axis, while in the circumference direction, the electrons are confined. This confinement effect causes the quantized effect from which optical properties of SWCNT arise.

In real space, two adjacent carbon atoms of a graphene sheet form a unit cell. In figure 1-5-a, the hexagonal carbon lattice in graphene and the unit cell is shown in x-y coordinates. The unit cell can be defined by two basis vectors $\vec{a}_1$ and $\vec{a}_2$. In reciprocal space, the $\vec{b}_1$ and $\vec{b}_2$ are the basis vectors in the Brillouin zone of graphene (equation 1-2).

Using a tight binding model, the energy dispersion of $2p_y$ orbital variations versus kx and ky is shown in figure 1-5-c. Because the only free electrons in graphene are π electrons in $2p_y$ orbital, this plot also represents the energy dispersion of graphene. The lower and upper half energy curve indicates the bonding (π) and anti-bonding (π^*) orbitals, respectively. As shown in figure 1-5, in graphene, the conduction and valence band touch at the K and K' points, which makes graphene a zero band gap material. But also because the upper and lower bands only touch at six Dirac points, graphene is also known as semi-metal.

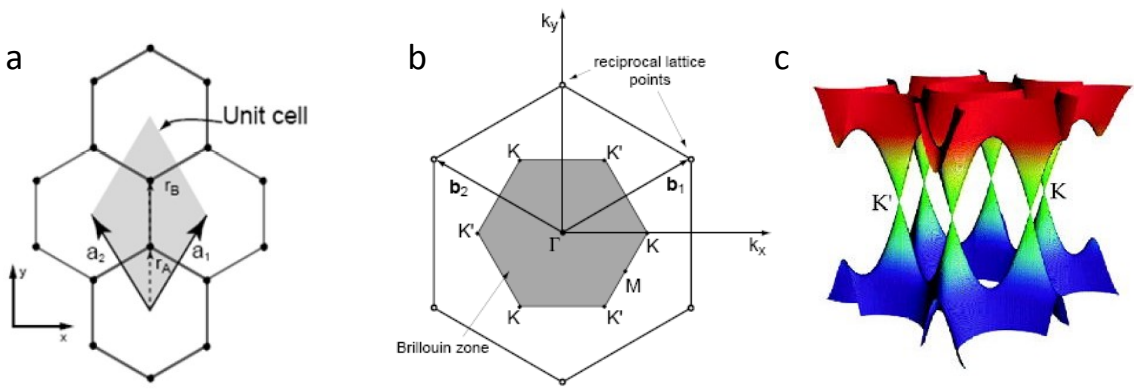

Figure 1-5 Unit cell of graphene in real space (a) and Brillouin zone (b). (c) energy dispersion of graphene. Figures are adapted from reference [57] and [58].

In a SWCNT, due to confinement, the wave number of the electrons in the circumferential direction $k_\perp$ is quantized while the electron wavenumber of parallel direction $k_\parallel$ is continuous. The continuum of $k_\parallel$ states are called sub-bands. The boundary condition for $k_\perp$ is defined as $k_\perp \cdot \pi \cdot d = 2\pi \cdot j$, where d is the diameter of the SWCNT and j is an integral.

When considering the band structure of SWCNT, the energy dispersion of graphene at K points become important. Figure 1-6 shows the electronic density of states (DOS) related to the nanotube electronic band structure. Each of the sub-bands in Figure 1-6 gives rise to a maximum in the DOS, known as a van Hove singularity (vHS). When the sub-bands pass the Dirac points, the carbon nanotubes are metallic; when the sub-bands miss the Dirac points, the nanotubes are semiconductors.

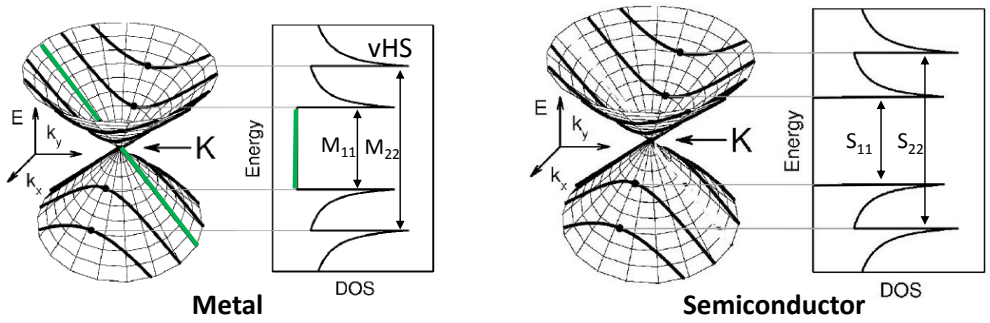

Figure 1-6 Energy dispersion of graphene at K point. The solid cutting lines denote the sub-bands in SWCNT. Sub-band passing the K point (left) result in zero band gap in DOS therefore a metal SWCNT; When the sub-bands miss the K point (right) and resulting in a band gap, the SWCNTs are semiconductors. Figures are adapted from reference [53].

A SWCNT is represented by a pair of chiral vectors (*n, m*). As shownin figure 1-7, by rolling the graphene sheet at different directions, the carbon hexane unit on the surface of nanotubes will point at different directions. Integer n and m denote the number of unit vectors along two directions, $\vec{a}_1$ and $\vec{a}_2$ in the honeycomb lattice of graphene. Zigzag and armchair nanotubes are formed in the situation when *m*= 0 and *n*=*m*, respectively. Depending on how the graphene sheet is rolled up, the SWCNT can be either metal or semiconductor. When (*n*-*m*)/3 is an integral, SWCNTs behave like metals, otherwise they are semiconducting. The diameter of a SWCNT is related to n and m in terms of: $d_t = \frac{|\vec{C}|}{\pi} = \frac{a\sqrt{n^2+m^2+nm}}{\pi}$

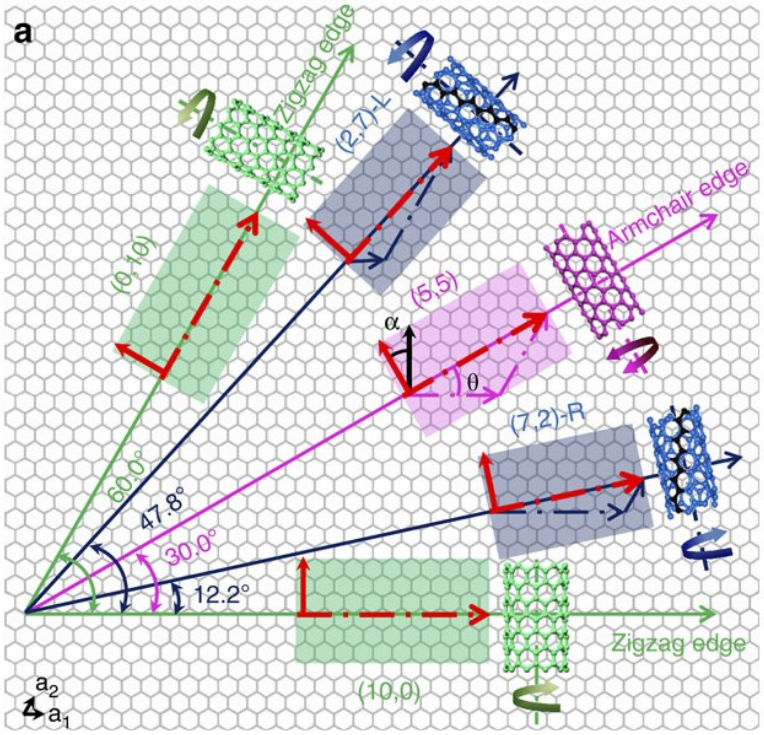

Figure 1-7 A schematic graphene sheet used to illustrate the (n,m) concept. Specifically, (0,10) and (5,5) are shown for zigzag and armchair tubes. (2,7) and (7,2) share the same diameter but they are chiral due to the fact that they are not mirror imaging of each other[59].

1.2 Spectroscopy of carbon nanotubes

The most important optical characterization methods of carbon nanotubes include absorption, fluorescence and Raman spectroscopy.

Aggregated carbon nanotubes have broad absorption from the UV to the NIR region. Due to strong electronic coupling, no peak features associated with individual carbon nanotube species are present in the absorption spectrum of bundled CNTs. The same principle can be applied to MWCNTs, where, due to strong inter-tube interactions,

there is no distinct absorption peak. Isolation of individual tubes to decouple the optical behavior is crucial for optical and electronic studies of CNTs.

One of the most common methods to solubilize carbon nanotubes involves mechanical methods with the aid of surfactants or polymers. Generally high shear force is introduced into an aqueous mixture of CNTs and surfactants to overcome the van der Waal interactions among CNTs, by vigorous ultrasonication.[60–62] High speed ultracentrifugation is then used to remove metals catalysts and small nanotube bundles. The supernatant solution prepared by this method contains individually dispersed CNTs with resolvable spectroscopic features.

Typical surfactants that are used to disperse carbon nanotubes include sodium dodecyl sulfate (SDS), sodium dodecylbenzenesulfonate (SDBS), sodium cholate (SC) and also nonionic surfactants, such as Triton X-100.[62] The exact morphology of the surfactant on carbon nanotubes is not well understood and may include formation of cylindrical micelles, bead-like structures or random adsorption to the CNT.[63] The general consensus is that SDBS and SC pack the carbon nanotubes tighter than SDS.[64] Due to different structures of the surfactant, the interaction between tube and surfactant result in shifting absorbance and fluorescence peak positions. For example, SDBS, structurally similar to SDS, contains an aromatic ring allowing energy stabilization caused by π-π stacking which give rise to the red-shifted E11 absorption peak[61].

Several parameters of surfactant will affect the carbon nanotubes dispersion status and optical spectra, such as concentrations of surfactant and pH of the solution. [65,66] Typical ionic-surfactant concentration used to effectively solubilize CNT is 1-2%.

The properties and spectra aforementioned are mostly from surfactant dispersed SWCNTs. Due to the perturbed electronic structure between the walls, MWCNT spectra are different from that of SWCNTs. In most cases MWCNT will not show measurable of optical features, for example, RBM and absorption peaks, due to strong inter tube interactions.

1.2.1 Absorption and fluorescence spectra

Absorption spectroscopy is an important and powerful tool for CNT characterization. Electronic transitions in pristine SWCNTs result in sharp absorption features that are closely related to the structure of SWCNTs and can be used to identify nanotube chirality. Compared with Raman and fluorescence, absorption spectra of SWCNTs are advantageous in the following three aspects: 1) unlike fluorescence which only detects semiconducting tubes, absorption spectroscopy reveals a broad range of SWCNT structures including metals and semiconductors, 2) a single absorption spectrum contains all the sample information while in Raman and PL spectra, in order to obtain information about all the structures, multiple excitation energies are required to probe individual species and 3) one can calculate the carbon concentration in SWCNT solutions from the absorption spectrum[67].

Fluorescence is only capable of characterizing the semiconductors due to the fact that metals do not fluoresce. However, for semiconducting SWCNTs, fluorescence spectroscopy is the most sensitive characterization method among absorbance, fluorescence and Raman.

1.2.2 Raman spectra

Before the discovery of absorption and fluorescence features of CNTs, Raman scattering spectroscopy was the most popular characterization method. Raman spectra provide detailed information about the carbon nanotube, including structure, chirality, and purity[68]. The sample preparation requirement for Raman characterization is minimal because the Raman signal is strong and consistent in both single and bundled tubes. In Raman spectra of CNTs, there are four important features radial breathing mode (RBM), G-band, D-band and G' band.

Typically, in the Raman spectra, the RBM of carbon nanotubes will appear at 150-350 cm^{-1}. As one can ascertain from the name, RBMs correspond to the expansion-contraction vibration of the carbon atoms in the tube's radial direction. Out of all the Raman features, RBM is the only one whose peak position strongly depends on the diameters of the tubes. The dependence can be expressed as:

$$\omega_{RBM} = \frac{218}{d} \qquad \text{Equation 1-2}$$

where ω_{RBM} and d are the Raman frequency and diameter of the SWCNT, respectively.

G band, also known as tangential mode, usually appears around 1500-1600 cm^{-1}, and corresponds to the vibrational modes of carbon atoms in the graphite structure. The G band is a universal feature in all graphitic materials, including graphene, carbon nanotubes and graphite. Due to the vibrational modes of the carbon atoms parallel and perpendicular to the tube axis, the G band is usually degenerated into two peaks, G+ and G- peaks, respectively. An important characteristic of the G mode appears for metallic CNTs where the G- peak is more pronounced than that of semiconducting

CNTs[69]. Although some research shows the position of G peak is also related with the chirality of a SWCNT, it is with much lower accuracy compared with the RBM.

The D-band appearing at ~1300 cm^{-1} originates from the presence of sp^3 defects in the graphitic structure. There is also a G' peak around 2500 cm^{-1} in the carbon nanotubes' Raman spectrum which is due to the second overtone of the defect mode. The ratio of D over G (D/G) can be used as an indicator of the quality of the graphite lattice. The higher the D/G value, the more sp^3 defects are present in the carbon lattice. Therefore, the D/G ratio is used to compare the degree of functionalization for carbon nanotubes during covalent treatment. However, the D/G ratio only provides qualitative, not quantitative, information about the defects. X-ray Photoelectron Spectroscopy (XPS) is a more quantitative method for determination of the functionalization degree of carbon nanotubes.

Raman spectra of SWCNTs, DWCNTs and MWCNTs share some similarity but also differ in many ways. The RBMs of a DWCNT are separated into two different regions, inner tube RBM and outer wall RBM. Because the diameters of a CNT are inversely proportional to the RBM Raman shift, the inner tubes correspond to the higher shift region while the outer walls are related to the lower shift region[37].

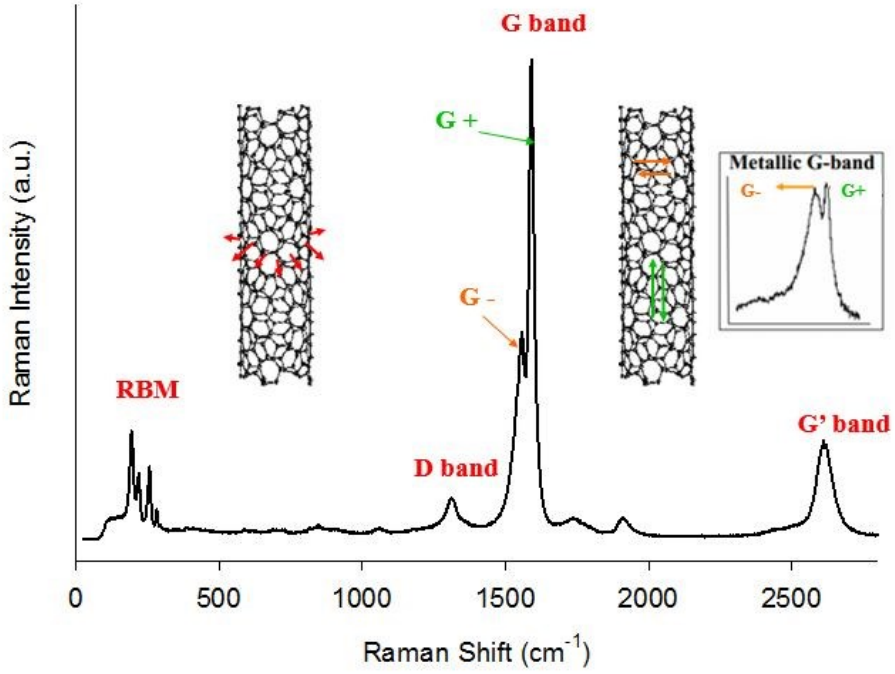

Figure 1-8 Typical Raman spectra of carbon nanotubes. The inset carbon nanotubes illustrate the concept of radial breathing vibration (red) and tangential vibrations along (green) and perpendicular (orange) to the tube axis. Figure adapted from reference [70].

1.2.3 Kataura plot

Carbon nanotubes with different diameters have a different set of transition energies. The Kataura plot was first proposed by Hiromichi Kataura in 1999 to connect band gap energy and diameter information of carbon nanotubes.[71] A typical Kataura plot uses nanotube diameter and transition energies as the x and y axes. Because the Raman shift is inversely proportional to tube diameters and can be calculated with equation 1-2, Raman shift can instead be used in place of tube diameter as the x-axis. If the y-axis has band gap energy converted to wavelength, a Kataura plot can also be

used to investigate the absorption and fluorescence versus the tube diameter. It is a very useful plot, so much so that it has been cited over 1000 times in scientific publications.

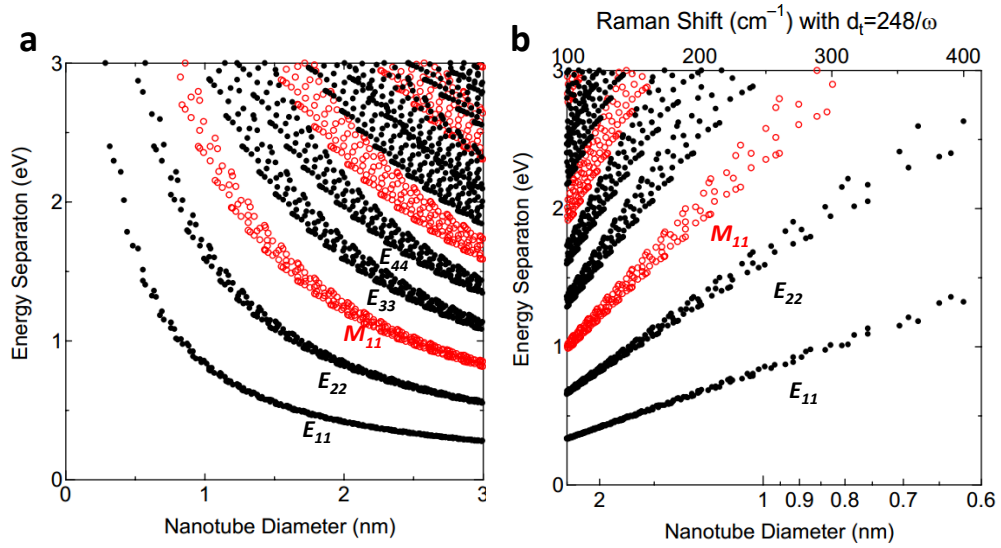

Figure 1-9 Kataura plots[72]. (a) Energy vs. nanotube diameter (b) Energy vs. Raman shift.

1.3 Carbon nanotube separation

Individual carbon nanotubes tend to bind together to form bundles because of van der Waals interactions between the tubes[73]. Mechanically, bundled carbon nanotubes are weaker than individual tubes. Electronically, the bundling effect causes energy interruption of the electronic states[74]. For many applications, de-bundling and obtaining individual carbon nanotubes is highly desirable.

High purity, single chirality carbon nanotubes are crucial for both scientific study and industrial applications including high-performance field-effect transistors and optoelectronics. However, it remains extremely difficult to synthesize mono-

chirality carbon nanotubes. Post-synthesis separation is therefore an attractive methodology to separate specific chirality of SWCNTs from as-prepared mixtures. DNA separation[25], size exclusion chromatography[26] and density gradient ultracentrifugation (DGU)[27] are the most efficient post-synthesis separation methods.

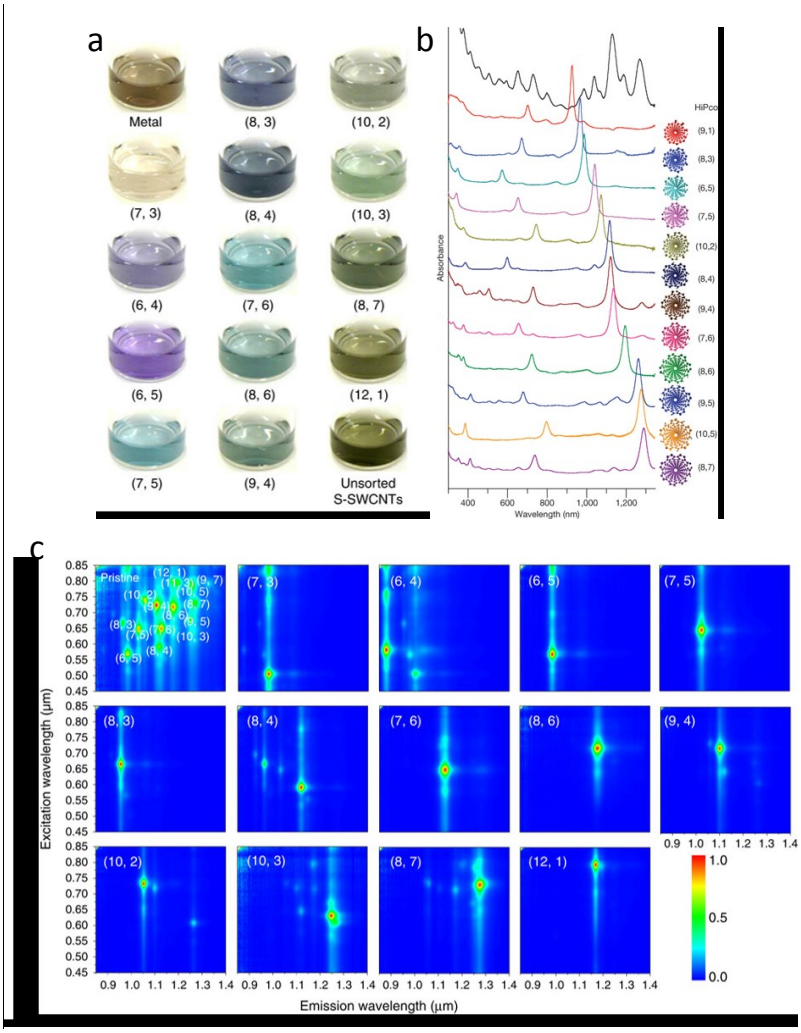

Figure 1-10 (a) Photographs of solutions of chirality-enriched SWCNTs[26]. (b) Absorption[25] and (c) fluorescence[26] spectra of chirality-enriched SWCNTs.

Solutions made of as-synthesized carbon nanotubes are black. Until carbon nanotubes are separated according to their structures, the true colors of nanotubes are

not revealed. By choosing DNA with different sequences, Zheng and co-workers separated 12 chiralities of SWCNTs with extremely high purity as determined by absorbance spectroscopy[25]. Even today DNA purification methods produce the purest single chirality nanotubes reported; however, the cost is considerably high and the scale of separation is very low. The exact separation mechanism is unclear but it is proposed that the selection arises from the electrostatic and electrodynamic interactions between DNA–SWCNT hybrids.

Allyl dextran-based size-exclusion gel chromatography was introduced by the Kataura group in 2011 to separate carbon nanotubes on the basis of their chirality[26] (Figure 1-10(a)). Compared with DNA separation, this chromatography method is highly effective, scalable and easy to operate with low cost.

In 2006, Hersam and co-workers[27] reported an electronically purified carbon nanotube separation technique based on the subtle differences in densities resulting in diameter variation of carbon nanotubes. Specifically, purification is induced by ultracentrifugation in a density gradient media. Carbon nanotubes settle within the media with respect to their buoyant densities resulting in spatial separation as seen in Figure 1-11.

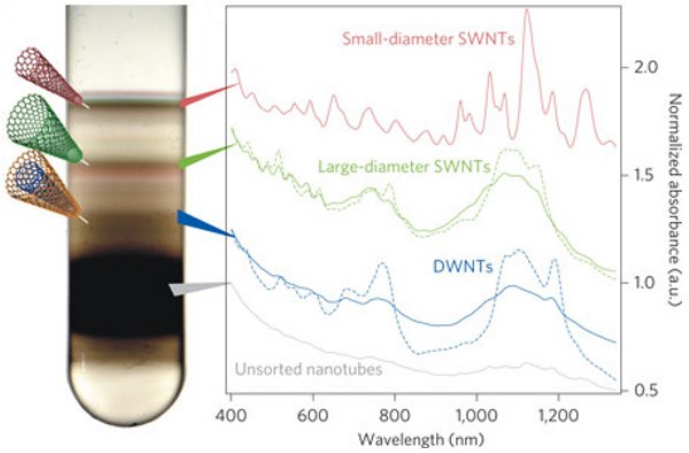

Figure 1-11 photograph of an ultracentrifuge tube after sorting the CNT by DGU. Each distinct layers contains CNTs with different wall numbers or SWCNTs of different diameters. Absorption spectra of small and large diameter SWCNTs and DWCNTs are shown to compare with unsorted CNTs[27].

1.4 Diazonium functionalization of carbon nanotubes

The CNT is made of sp^2 carbons. The difference in sidewall reactivity of carbon nanotubes is in part due to local strain arising from misalignment of the π-orbitals between the neighboring carbons and pyramidalization on the carbons that is caused by the curvature[75].

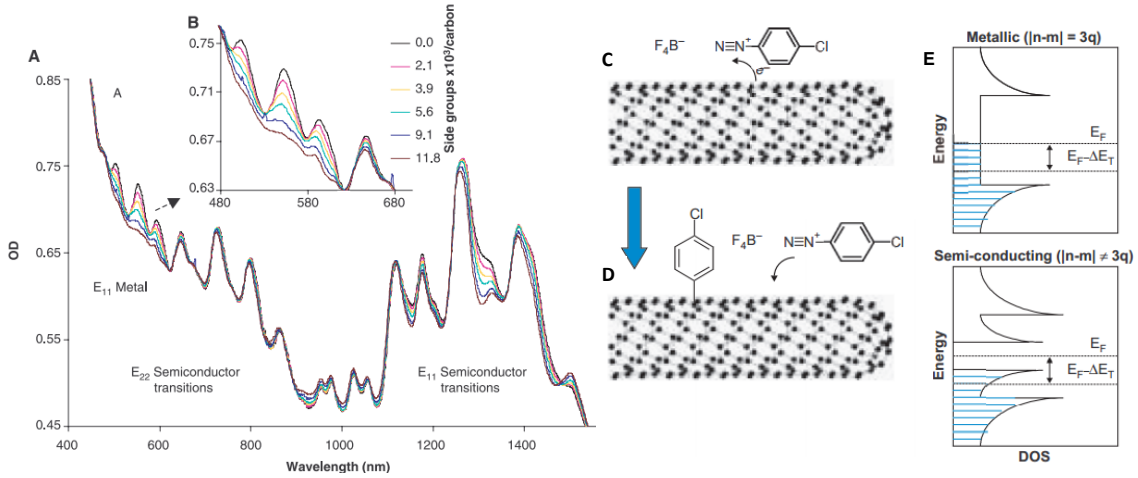

Figure 1-12 (a) and (b) are absorption spectra evolution of SWCNT upon reaction with diazonium[76]. Clearly the metallic tubes are selectively functionalized. Schematic illustration of diazonium chemistry with SWCNT (c, d) and electron density near Fermi level leads to higher initial activity for metallic nanotubes (e)[76].

Aryl diazonium salts have been widely used to functionalize various materials, including graphite, [77,78] metal surfaces[79] and buckyballs[80]. This chemistry became particularly interesting with carbon nanotubes because it allowed selective functionalization of the metallic SWCNTs over semiconducting SWCNTs for the first time[76]. This process is shown in figure 1-12. One electron is transferred from the nanotube to the diazonium, then through reduction the diazonium loses a N_2 and covalently bonds to the surface of the SWCNT. The selectivity is believed to arise from the increased presence of electrons near the Fermi level in metallic SWCNTs, which reduces the diazonium faster than in semiconductor SWCNTs.

The diazonium reaction with SWCNTs is a two-step reaction[64]. First, long-lived intermediates formed from diazonium salts non-covalently adsorb onto the surface of carbon nanotubes. This step is fast and preferentially selective with the *m*-SWCNT

through charge transfer. Once the intermediate is adsorbed on the surface of SWCNT, a slow covalent bonding will occur without selectivity.

Although the exact intermediate structure and reaction route are still not well understood, the Gomberg–Bachmann reaction along with radical reaction can be adapted to explain the mechanism[81]. In the initiation step two diazonium ions will form a diazonium anhydride which cleaves into two aryl radicals. One aryl radical reacts with a SWCNT to generate an aryl-SWCNT·which is then terminated by the other aryl radical[82].

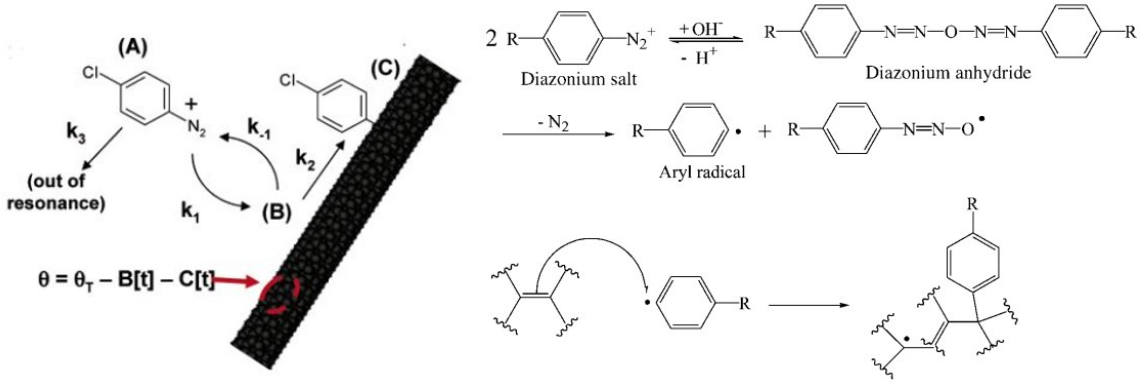

Figure 1-13 Two-step mechanism[64] of diazonium chemistry with SWCNT and possible reaction route[83].

Although the diazonium chemistry with carbon nanotubes is known for its selectivity, it is rather difficult to control the reaction to obtain such metal vs. semiconductor selectivity. The diazonium reaction is a radical reaction which means that the reagent will attack the carbon lattice in an arbitrary pattern[84,85]. This is highly desirable when a uniform functionalization of the carbon nanotube surface is needed.

2 Brightening of dark excitons in semiconducting carbon nanotubes with sp^3 defects

Adapted from Piao, Y.; Meany, B.; Powell, L. R.; Valley, N.; Kwon, H.; Shatz, G. C.; Wang, Y. Nat. Chem. 2013, 5, 840.

Y.W. and Y.P. conceived and designed the experiments. Y.P., B.M., L.R.P. and H.K. performed experiments. N.V. and G.C.S. performed DFT calculations. Y.W., Y.P. and G.C.S. wrote the manuscript with inputs from all authors.

2.1 Introduction

Semiconducting SWCNTs exhibit characteristic near-infrared photoluminescence, which creates substantial potential for a broad spectrum of applications, including imaging, sensing, quantum cryptography and optoelectronics[18,39,42,86–88]. However, the photon conversion efficiency (photoluminescence quantum yield, Φ) is surprisingly low in these nanostructures. Macroscopic samples of SWCNTs typically have $\Phi < 1\%$[28,89], which is much lower than for other semiconducting nanomaterials, such as nanowires and quantum dots[90]. Extrinsic factors, such as hole doping and covalent functionalization, are known to quench nanotube photoluminescence[29,91]. Minimizing these chemical effects by hole passivation[91] and oxygen-excluding surfactants[29] improves Φ significantly, but the overall efficiencies still remain relatively low. Quantum theory suggests that the low Φ is a consequence of the myriad of non-radiative 'dark' states that reside ~5–100 meV below the optically allowed E11 'bright' exciton[92–95], which facilitates efficient non-radiative relaxation of the excited states[94,96]. As a result, it has been experimentally

challenging to harness these inaccessible dark excitons, or even to elucidate or control their effects on the low photoluminescence Φ of SWCNTs.

Here, we demonstrate the brightening of nanotube photoluminescence by a factor of up to 28 through the chemical creation of a new, optically allowed state that lies below the predicted energy levels of dark excitons (Figure 2-1). Creation of this state is achieved by reacting individually suspended SWCNTs with aryl diazonium salts in deuterium oxide (or water) at room temperature. Covalent sidewall functionalization, and diazonium chemistry in particular, is widely known to induce undesired sp^3 defects in the sp^2 lattice of carbon nanotubes and to quench nanotube photoluminescence drastically[97,98]. Hence, our observation was completely unexpected and challenges our current understanding of defect quantum states in low-dimensional carbon materials.

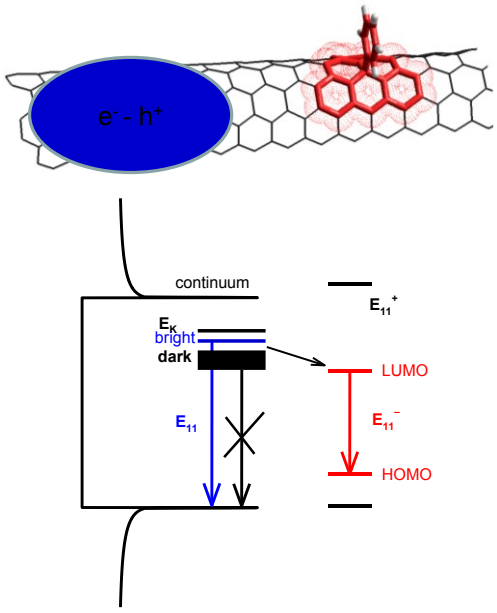

Figure 2-1 Controlled sp^3 defects brighten dark excitons. Local energy minimum created by a symmetry-breaking sp^3 defect in a SWCNT provides a pathway for low-lying dark excitons to optically recombine efficiently.

2.2 Materials and Methods

2.2.1 Materials:

Purified (6,5) SWCNTs individually suspended by 1 wt.% SDS in D_2O.

Chirality-enriched Semiconducting SWCNTs suspended by 1 wt.% SDS in D_2O.

Diazonium Salts (Table 2-4):

4-dizao-N,N-diethylaniline tetrafluoroborate: MP Biomedicals

4-*tert*-butylbenzenediazonium tetrafluoroborate: synthesized

4-methylbenzenediazonium tetrafluoroborate: synthesized

Benzenediazonium tetrafluoroborate: synthesized

4-methoxybenzenediazonium tetrafluoroborate: Sigma Aldrich, 98%

4-carboxylbenzenediazonium tetrafluoroborate: synthesized

4-bromobenzenediazonium tetrafluoroborate: Sigma Aldrich, 96%

4-nitrobenzenediazonium tetrafluoroborate: synthesized

3,5-dinitrobenzenediazonium tetrafluoroborate: synthesized

Chemicals:

HiPco SWCNTs, lot. no. 194.3, Rice University

Sephacryl™ S-200 High Resolution, Size-exclusion chromatography (SEC) resin, GE Healthcare

Deuterium oxide (D_2O): Cambridge Isotope Laboratories, Inc. 99.8%

Sodium dodecyl sulfate (SDS): Sigma Aldrich, ≥98.5%

Sodium Nitrite: Sigma Aldrich, ≥97.0%

Tetrafluoroboric acid solution: Sigma Aldrich, 48 wt. % in H_2O

Diethyl ether: Fisher Chemical, anhydrous, BHT-stabilized

R-aniline: 4-niroaniline (Sigma Aldrich, ≥99%), 4-aminobenzoic acid (Sigma Aldrich, ≥99%), 4-*tert*-butylaniline (Sigma Aldrich, ≥99%), p-toluidine (Sigma Aldrich, ≥99%), Aniline (Sigma Aldrich, ≥99.5%), 3,5-dinitroaniline (Sigma Aldrich, 97%)

Acetonitrile -D3: Cambridge Isotope Laboratories, Inc., D, 99.8%

2.2.2 Instruments

UV-vis-NIR absorption spectroscopy: Absorption spectra were measured using a PerkinElmer Lambda 1050 UV-vis-NIR spectrophotometer equipped with a photomultiplier tube (PMT; σ=2.03% over 48 hours of continuous run) and a broadband InGaAs (σ=1.56% over 48 hours of continuous run) detector. The instrument was warmed up for 15 minutes prior to each use.

Raman Spectroscopy: Raman spectra were collected using a Horiba Jobin Yvon LabRAM Raman microscope (model ARAMIS). The 632.8 nm output of a helium-neon ion laser was used as the excitation line due to its overlap with the resonant excitation window of (6,5) SWCNTs according to the Kataura plot. The power density of the incident laser was approximately 1.4 mW/μm^2.

Fluorescence Spectroscopy: Fluorescence spectra and excitation-emission maps were collected on a HORIBA Jobin Yvon Nanolog Spectrofluorometer equipped with a 450 W Xenon arc lamp and a multichannel InGaAs array detector. 10 nm and 20 nm bandpass were used for excitation and emission, respectively. The integration times were 1 sec for (6,5)-SWCNT enriched solutions and 8-10 seconds for other chirality-enriched samples.

X-ray photoelectron spectroscopy (XPS): Kratos Axis 165 (Manchester, U.K.)

1H-NMR: Bruker DRX-400 high resolution spectrometer

FT-IR Spectroscopy: Thermo Nicolet NEXUS 670 FTIR with ATR attachment

Ultrasonicator: MISONIX, model S4000

Bath sonicator: VWR, model B2500A-DTH

Ultracentrifuge: Beckman Coulter Optima LE-80K; 70 Ti rotor

Centrifuge: Beckman Coulter, Microfuge® 16

Nanopure water: Barnstead NANOpure DIamond Life Science (UV/UF) ultrapure water system, Thermo Scientific, Model D11931

2.2.3 Detailed Experimental Methods

*Preparation of Chirality-Enriched, Individually-Suspended SWCNT Solutions***.** Chirality-enriched SWCNT samples were separated from high pressure carbon monoxide (HiPco) SWCNTs (Rice University, Lot 194.3) using an adapted single-surfactant multicolumn gel chromatography procedure. SWCNTs were individually dispersed in an aqueous solution of 2 wt.% SDS by ultrasonication for two hours at 10°C (Misonex, S-4000) followed by ultracentrifugation (170,499*g* at 20°C for 4 hours) to remove nanotube bundles and metal impurities. The remaining solution of SWCNTs consisted of individually dispersed metallic and semiconducting nanotubes of various chiralities. Using gel chromatography, we isolated the chiral species (6,5) on a Sephacryl S-200 HR column (GE Healthcare). This column was washed with aqueous 2 wt.% SDS solution followed by a solvent exchange wash with 2 wt.% SDS in D_2O. Finally, the purified (6,5)-SWCNTs were eluted from the column with a solution of 5 wt.% SDS in D_2O. Chirality-enriched solutions, including CES1, which is the mixture of (7,5), (7,6), (8,3), and (8,4); CES2, which is the mixture of (8,3), (8,4), (9,2); and CES3, which contains mostly (7,6) and (8,4) were prepared by simplified

chromatographic purifications to remove undesired semiconducting and metallic SWCNTs. The final concentration of SDS was adjusted to 1 wt.% SDS in 99.8% D_2O.

The concentration of purified (6,5) was diluted with 1 wt.% SDS in D_2O for an absorbance of 0.12 at its peak wavelength of E_{11} (using a standard 1-cm path length cuvette). According to previous work by Zheng et al., this concentration corresponds to approximately 0.66 mg/L. The concentration of chirality-enriched solutions (CES1, CES2 and CES3) was adjusted with 1 wt.% SDS in D_2O so that the absorption baseline of the solution matched that of purified (6,5), more specifically the O.D. of both solution at 800 nm is 0.17.

Synthesis and 1H-NMR Characterization of Diazonium Salts. 4-bromobenzenediazonium tetrafluoroborate (Sigma Aldrich, 96%) and 4-methoxybenzenediazonium tetrafluoroborate (Sigma Aldrich, 98%) were stored at 4°C and -20°C, respectively. 4-dizao-N,N-diethylaniline tetrafluoroborate (MP Biomedicals) was stored at room temperature as the company instructed. 4-nitrobenzenediazonium tetrafluoroborate, 4-carboxylbenzenediazonium tetrafluoroborate, 4-*tert*-butylbenzenediazonium tetrafluoroborate, 4-methylbenzenediazonium tetrafluoroborate, 3,5-dinitrobenzenediazonium tetrafluoroborate, and benzenediazonium tetrafluoroborate were synthesized by a modified literature method using aniline and nitrous acid Specifically, 4.8 mmol of aniline was added to a round bottom flask (RBF), which was cooled in an ice bath. 9.71 mmol of sodium nitrite (Sigma Aldrich, ≥97.0%) was dissolved in 2 mL of Nanopure™ water and added dropwise to the RBF with stirring. The precipitated tetrafluoroborate salt was washed with 200 mL of diethyl ether under vacuum filtration for ~20 minutes

while being protected from light. The salts were stored at 4°C and used within a week after synthesis.

The successful synthesis of high purity diazonium salts was confirmed with FT-IR and ^{1}H nuclear magnetic resonance (^{1}H-NMR). NMR samples were prepared by dissolving ~1 mg of a diazonium salt in 0.5 mL of acetonitrile-D3 (99.8%, Cambridge Isotope Laboratories, Inc.) in a 5 mm diameter NMR tube (NORELL, 507HP). All of the NMR analyses were performed on a Bruker DRX-400 high resolution spectrometer. The characteristic splitting patterns in ^{1}H-NMR and vibrational features are tabulated in Table 2-1. Chemical shifts are reported in ppm downfield from TMS and referenced to the solvent.

Diazonium Functionalization of (6,5) SWCNTs and Other Chirality-Enriched Samples. Each diazonium salt was dissolved in D_2O to give a series of concentrations ranging from 10^{-2} to 10^{-6} M for reaction with SDS-suspended (6,5)-SWCNT solutions at room temperature. The diazonium solutions were protected from light and used immediately. Aliquots of the diazonium solutions were added to (6,5)-enriched 1 wt.% SDS in D_2O, with stirring and protected from light to give molar ratios of starting reactants, [Dz]/[C], including 1:5000, 1:2500, 1:1000, 1:800, 1:600, 1:400, 1:300, 1:250, 1:200, and 1:100. These ratios were adjusted for each diazonium salt due to their different reactivity. Similar procedure was used for the functionalization of (7,6)(8,4)-enriched sample (CES3) with NO_2-Dz. Samples were monitored over time with UV-vis-NIR absorption and fluorescence spectroscopy. The spectral range for absorption was from 1700 nm to 200 nm; the fluorescence excitation range was 300-800 nm and emission was monitored from 812.9-1572.9 nm. The solutions showed predictable

increases in E_{11}^- fluorescence emission for up to 286 hours before stabilizing; they were monitored spectroscopically for up to 9 months under selected conditions.

The reaction conditions for Br-Dz with purified (6,5) solution were as stated above, except that the SWCNT solution used was 45 mL for each condition to meet XPS sample requirement. After 360 hours of reaction, the carbon nanotubes were precipitated in ethanol for XPS and Raman characterization.

For other chirality-enriched samples (CES1 and CES2), 3.3 μL and 4.0 μL of 5×10^{-5} M NO_2-Dz solutions were added to two 2 mL SWCNT solutions, respectively, and reacted in dark for 360 hours. We note that light may accelerate the decomposition of diazonium salts and their reactions with SWCNTs. For Raman spectroscopy and XPS characterization, the reaction by-products and the surfactant were removed. A BUCHI Rotavapor (R-3000) was used to remove the bulk of the D_2O. Once the solution volume reached ~5 mL, the sample was centrifuged (Beckman Coulter, Microfuge® 16) at 14,000g for 15 minutes to form a pellet of SWCNTs and clear supernatant. The pellet was collected and washed with ethanol, and then re-dispersed in ethanol by gentle sonication with a bath sonicator for ~1 minute. This centrifugation-wash-dispersion was repeated 8-10 times to ensure clean removal of SDS and salts. The aggregated nanotubes were drop-cast onto glass slides and gold substrates for Raman spectroscopy and XPS characterization, respectively.

Measurement of PL Quantum Yields. The PL quantum yields of SWCNTs were determined against a reference dye, Styryl 13 (Exciton, Dayton, Ohio).

$$\Phi_{CNT} = \frac{\Phi_S}{Grad_S} \frac{PL_{CNT}}{Abs_{CNT}}$$

where

Φ_{CNT}: quantum yield of SWCNTs in 1 wt.% SDS/D_2O solution

Φ_S: quantum yield of Styryl 13 in spectroscopic grade methanol.

$Grad_S$: the slope of integrated emission intensity vs. absorbance plot for Styryl 13 solution

PL_{CNT} : integrated emission intensity of SWCNT solution

Abs_{CNT} : absorbance of SWCNT solution at the excitation wavelength

We neglected solvent refractive indices since the difference between methanol and 1 wt.% SDS/D_2O is negligible. The experiments were performed in the low concentration regimes with linearity across the concentration ranges (absorbance ~ 0.10 for a standard 10 mm fluorescence cuvette) to avoid inner-filter effects. The gradient of Styryl 13 was determined from a linear plot of integrated PL intensity vs. absorbance at the excitation wavelength (565 nm for (6,5)-SWCNTs and 580 nm for (6,4)-SWCNTs). We note that for (8,4) and (7,6)-SWCNTs, Styryl 13 is not an ideal reference dye due to small overlap with the absorption spectra. For this reason, we measured the PL intensity of these two structures only relative to their pristine forms.

Spectral Fitting. Emission and absorption spectra were fitted with Voigt functions using PeakFit software v4.12. The peak widths were set to be varied and no baseline was used for emission spectra.

Spectral Evolution and Characterizations. The SWCNT samples were monitored over time with UV-vis-NIR absorption and fluorescence spectroscopy.

Absorption spectra were measured using a PerkinElmer Lambda 1050 UV-vis-NIR spectrophotometer equipped with a photomultiplier tube and a broadband InGaAs detector. Fluorescence spectra and excitation-emission maps were collected on a HORIBA Jobin Yvon Nanolog Spectrofluorometer equipped with a 450 W Xenon arc lamp and a multichannel InGaAs array detector. The emission and absorption spectra were fitted with Voigt functions using PeakFit software v4.12. The PL quantum yields of SWCNTs were determined against a reference dye, Styryl 13 (Exciton, Dayton, Ohio). The experiments were performed in the low concentration regimes with linearity across the concentration ranges to avoid inner-filter effects. We note that for (8,4) and (7,6)-SWCNTs, Styryl 13 is not an ideal reference dye due to small overlap with the absorption spectra. Hence, the PL intensity of these two structures were measured relative to their respective pristine forms.

For Raman spectroscopy and XPS characterization, the reaction by-products and the surfactant were removed by centrifugation and repeated wash with ethanol. XPS experiments were performed on a Kratos Axis 165 spectrometer (Manchester, U.K.). Raman spectra were collected using a Horiba Jobin Yvon LabRAM Raman microscope (model ARAMIS) with the 632.8 nm output of a helium-neon ion laser as the excitation source. The power density of the incident laser was approximately 1.4 $mW/\mu m^2$.

DFT Calculations. DFT calculations were performed on a 4-nm long (6,5)-SWCNT using the BP86 functional. The nanotube ends are terminated by hydrogen atoms to minimize edge effects. An aryl group is covalently attached to the middle of

the nanotube and an additional hydrogen atom is attached at varying distances to create a closed-shell structure.

Table 2-1. Organic diazonium salts used in this study and their FT-IR and 1H-NMR characteristic signatures.

Name	Abbreviation by Substituent Group	Molecular Structure	Chemical Shifts (ppm)[a]	Characteristic IR Features (cm^{-1})[b]	Source
4-diazo-N,N-diethylaniline tetrafluoroborate	$N(CH_2CH_3)_2$-Dz	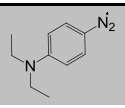 BF_4^-	δ 7.45 (ABq, *J* = 8.8 Hz, Δν = 419.2 Hz, 4H), 1.24 (t, *J* = 7.2 Hz, 6H), 3.60 (q, *J* = 7.2 Hz, 4H)	3122, 3084, 2980, 2940, 2135, 1579	MP Biomedicals
4-tert-butylbenzenediazonium tetrafluoroborate	$C(CH_3)_3$-Dz	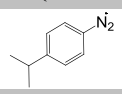 BF_4^-	δ 8.17 (ABq, *J* = 8.8 Hz, Δν = 176.8 Hz, 4H), 1.38 (s, 9H)	3106, 2972, 2903, 2275, 1574,	Synthesized
4-toluenediazonium tetrafluoroborate	CH_3-Dz	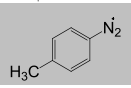 BF_4^-	δ 8.55 (ABq, *J* = 8.8 Hz, Δν = 254.4 Hz, 4H), 2.64 (s, 3H)	3112, 3039, 2287, 1581	Synthesized
benzenediazonium tetrafluoroborate	H-Dz	 BF_4^-	δ 8.50 (d, J = 8.8 Hz, 2H), 8.34 – 8.25 (m, 1H), 7.97 (dt, J = 8.0 Hz, 2H)	3107, 3018, 2295, 1570	Synthesized
4-methoxybenzenediazonium tetrafluoroborate	OCH_3-Dz	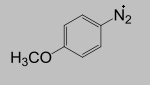 BF_4^-	δ 8.40 (dd, J = 9.4, 9.5 Hz, 2H), 7.34 (dd, J = 9.4, 9.5 Hz, 2H), 4.06 (s, 3H)	3122, 3106, 2250, 1583, 1572	Sigma Aldrich, 98%
4-carboxybenzenediazonium tetrafluoroborate	COOH-Dz	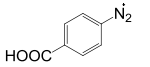 BF_4^-	δ 8.49 (ABq, *J* = 9.0 Hz, Δν = 67.2 Hz, 4H)	3279, 3113, 3042, 2302, 1729, 1581	Synthesized
4-bromobenzenediazonium tetrafluoroborate	Br-Dz	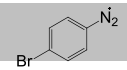 BF_4^-	δ 8.22 (ABq, *J* = 9.1 Hz, Δν = 98.4 Hz, 4H)	3106, 3092, 2286, 1554	Sigma Aldrich, 96%
4-nitrobenzenediazonium tetrafluoroborate	NO_2-Dz	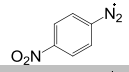 BF_4^-	δ 8.68 (ABq, *J* = 9.2 Hz, Δν = 58.5 Hz, 4H)	3104, 3023, 2306, 1614, 1537	Synthesized
3,5-dinitrobenzenediazonium tetrafluoroborate	3,5-(NO_2)-Dz	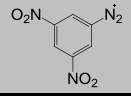 BF_4^-	δ 9.78 (s, 1H), 9.69 (s, 2H)	3075, 3042, 2316, 1548	Synthesized

[1]CD_3CN was used as the solvent, [2]Monitored from 4000-400 cm^{-1}; the frequencies shown indicate O-H stretch (3279 cm^{-1}), sp^2 (3023~3122 cm^{-1}), sp^2-CH stretch (2903~2980 cm^{-1}), N≡N stretch (diazonium bond, 2135~2316), C=O stretch (1614 cm^{-1}) and aromatic C=C bending (1537~1614 cm^{-1}), respectively.

2.3 Result and Discussion

2.3.1 New PL peak (E_{11}^-) in functionalized SWCNT

As a first example, we observe a new PL peak, E_{11}^-, at 1137 nm in sodium dodecyl sulfate (SDS)-suspended (6,5)-SWCNTs that have been covalently functionalized with 4-nitrobenzenediazonium tetrafluoroborate (Figure 2-1 (a)). Unambiguous assignment of spectral features was made possible by using high-purity SWCNTs that had been separated using dextran gel chromatography[26]. The observed new peak is red-shifted by 162 nm (181 meV) from the original E_{11} excitonic transition, with the full width at half maximum (FWHM) of the peak increased from 41 meV to 57 meV (39%). The E_{11}^- feature is 8.4 times brighter than the E_{11} PL of pristine (6,5)-SWCNTs.

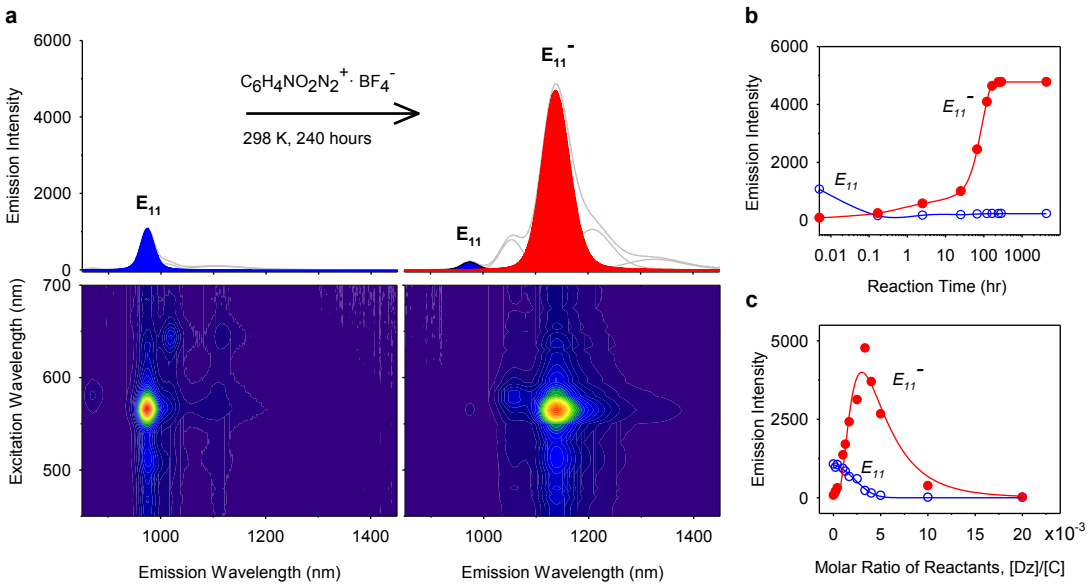

Figure 2-2 Spectrochemical evolution of exciton photoluminescence in diazonium functionalized (6,5)-SWCNTs. a, Covalent sidewall functionalization of (6,5)-SWCNTs with 4-nitrobenzenediazonium tetrafluoroborate gives rise to a new

fluorescent peak, E_{11}^{-}, that is red-shifted 181 meV and 8.4 times brighter (in integrated intensity) than the original E_{11} exciton photoluminescence. This new spectral feature is sensitive to b, reaction time and c, relative concentration of diazonium salts. The peak grows as the reaction proceeds over a course of 240 hours, after which it has remained stable for more than 9 months. This new feature occurs in a small window of extremely low density of functional groups, beyond which it is completely lost. The peaks are fitted with a Voigt function with FWHM of 41 and 57 meV for E_{11} and E_{11}^{-}, respectively. The peak at 1058nm is E11- from trace of (6,4) and the origin of the peaks beyond 1134nm are unclear.

The increase in PL quantum efficiency is strongly dependent on both the nanotube chirality and the functional group used (Table 2-2 and Table 2-3). The maximum brightening was observed for $C_6H_4NO_2$ functionalized (6,4)-SWCNTs, or (6,4)-$C_6H_4NO_2$, which increases Φ 28-fold (Figure 2-3). We measured Φ of SDS-suspended, covalently functionalized nanotubes against a reference dye with a known quantum efficiency[29,89]. Both (6,4)-$C_6H_4NO_2$ and (6,5)-$C_6H_4NO_2$ had Φ of approximately 16%, placing them among the brightest reported ensembles of SWCNTs in water[28,89,91]. Optimal individual nanotubes that are free of ensemble averaging over structural heterogeneity may be even brighter, as typically found with nanotube samples[28,91].

Table 2-2 Spectral characteristics of new PL peaks in SWCNT-$C_6H_4NO_2$ shows strong dependence on nanotube chirality.

(n,m)	*Pristine*		*Covalently Functionalized*				E_{11}^{-}-E_{11} (meV)	$\frac{\Phi_{E11^-}}{\Phi_{E11}}$
	E_{11} (nm)	FWHM (nm)	*f*-E_{11} (nm)	FWHM (meV)	*f*-E_{11}^{-} (nm)	FWHM (meV)		
(7,6)	1113	31	1113	34	1263	59	-132	0.5
(8,4)	1109	34	1109	35	1263	57	-136	1.0
(9,2)	1133	30	1134	33	1300	73	-140	
(7,5)	1015	34	1015	33	1179	70	-170	
(6,5)	972	35	975	41	1137	57	-181	8.4
(8,3)	942	40	942	36	1154	67	-241	
(6,4)	870	38	869	51	1058	65	-254	28.6

Table 2-3 Brightening of (6,5)-C_6H_4X PL strongly depends on the Hammett substituent constants (σ_p) of the terminating moieties, X.

X	σ_p	E_{11} (nm)	FWHM (meV)	E_{11}^{-} (nm)	FWHM (meV)	E_{11}^{-} E_{11} (meV)	$\frac{\Phi_{E11^-}}{\Phi_{E11}}$	
O-doped	n.a.		43		50	-154	~1.3	a)
-$N(C_2H_5)_2$	-0.72	973	40	1110	58	-157	3.9	
-OCH_3	-0.27	972	41	1114	58	-163	5.8	
-$C(CH_3)_3$	-0.20	972	42	1120	71	-169		
-CH_3	-0.17	972	40	1116	57	-165	6.0	
-H	0.00	972	42	1119	56	-168		
-COO^-	0.00	975	42	1124	59	-169		
-Br	0.23	972	41	1125	57	-174	6.9	
-NO_2	0.78	975	41	1137	57	-181	8.4	
3,5-$(NO_2)_2$	1.42	975	42	1148	58	-192	10.3	

(a) estimated based on Figure 1B of Ghosh et al.[99]

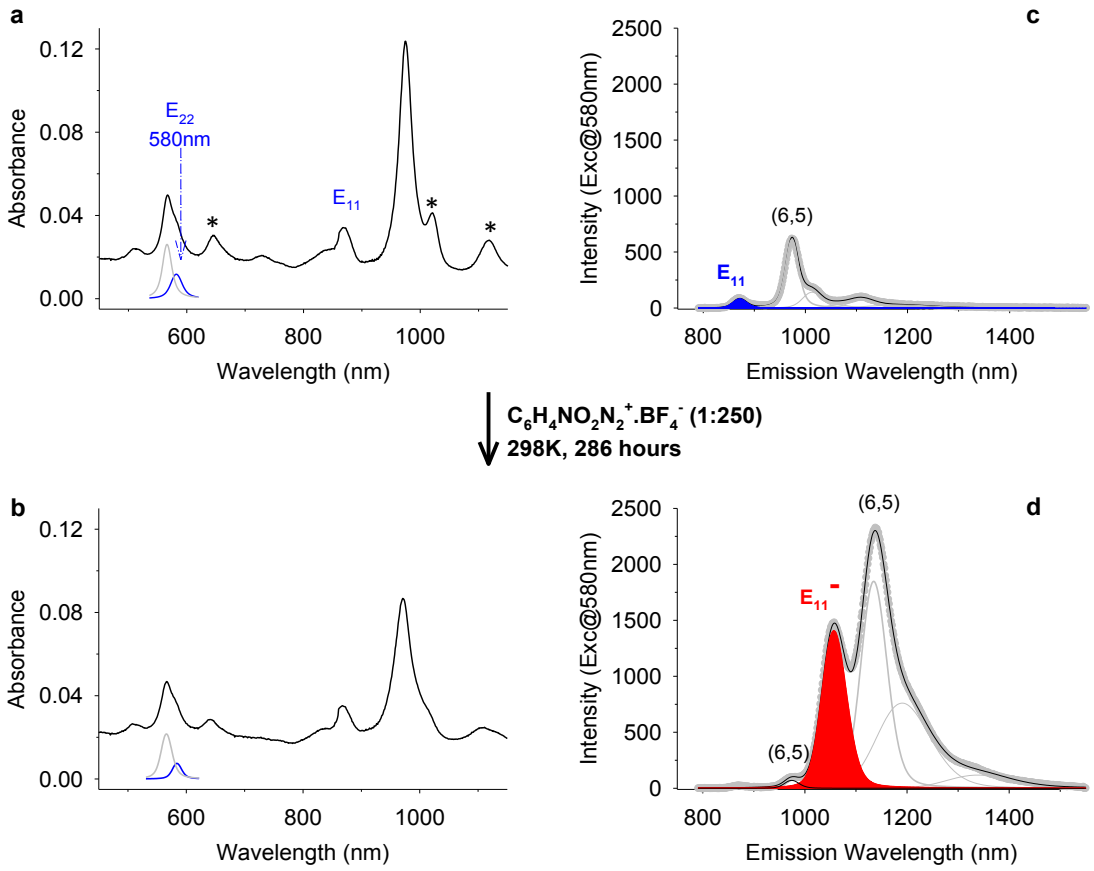

Figure 2-3 Bright E_{11}^{-} emission from (6,4)-$C_6H_4NO_2$. During the separation there are always small amount of (6,4) SWCNTs mixed in pure (6,5) solution. The E_{22} and E_{11} electronic transitions for (6,4) is 580nm and 870nm, respectively. Visible-NIR absorption (a, b) and fluorescence (c, d) spectra before and after covalent functionalization of (6,4) SWCNTs with $C_6H_4NO_2$ functional groups. The extra absorption peaks noted by asterisks in (a) are due to other small amount of SWCNT species in the solution.

This new PL feature and its brightening were observed within a narrow window of reaction conditions (Figure 2-2 (b,c)). We followed approximately 150 reactions with correlated visible/near-infrared absorption and fluorescence spectroscopy techniques over more than 240 hours (Figures 2-8, 2-9, 2-10). In every reaction, the

intensity of E_{11} emission dropped to noise level within 10 minutes after adding the diazonium salt (Figure 2-2 (b)). This observation is consistent with previous single-molecule fluorescence spectroscopy studies in which individual SWCNTs show step-wise quenching upon addition of 4-chlorobenzenediazonium tetrafluoroborate[100]. However, we found that the E_{11}^- peak arose shortly after the disappearance of the E_{11} PL. This new feature steadily grew as the reaction proceeded over a course of ~200 hours, after which it became remarkably stable, with more than 9 months of shelf life, with the exception of a 27% drop in PL intensity due to bundling effects (as similarly occurred in non-reacted nanotube controls).

The PL intensity of E_{11}^- strongly depends on the surface density of functional groups. In Figure 2-2 (c) we plot the PL intensity of (6,5)-$C_6H_4NO_2$ as a function of the initial relative reactant concentration of 4-nitrobenzenediazonium tetrafluoroborate. The E_{11}^- PL peak grows at the expense of E_{11}, and ultimately becomes much stronger than the original E_{11} emission, reaching a maximum at a relative reactant concentration of 0.4 mole% 4-nitrobenzenediazonium tetrafluoroborate. To quantify the functional groups that ultimately attached covalently to the nanotubes, we replaced the NO_2 substituent with Br, which has an unambiguous X-ray photoelectron spectroscopy (XPS) signature and a higher X-ray cross section than nitrogen, and characterized the covalently functionalized SWCNTs with Raman spectroscopy and XPS (Figures 2-4, 2-11).

For samples with the maximum E_{11}^- PL, we estimate that 0.06 ± 0.01% of the carbon atoms were bonded with an aryl group, corresponding to approximately one functional group per 20 nm length of (6,5)-SWCNT. This distance is roughly 5 times

less than the exciton diffusion length[19]. In agreement with this measurement, the low concentration of functional groups on the nanotube sidewall caused little change in the E_{11} and E_{22} absorbance (Figures 2-8, 2-9, 2-16). When the functional density approached a 5 nm pitch, the new PL feature diminished in intensity. An increase in excess defects along the (6,5)-SWCNT wall irreversibly quenches both the E_{11} and E_{11}^- PL, therefore careful control over the diazonium chemistry is necessary.

This small window of reaction conditions explains why this remarkably bright new feature has remained unnoticed despite the more than a decade of intense research in nanotube wet chemistries[97,98]. We initially suspected that the E_{11}^- emission might share the same physical origins with that of the PL features recently observed or predicted in nanotubes doped with oxygen[99,101] or hydrogen atoms[57,102], or alkylated[103]. However, previous studies note that the PL intensity of these sidebands is weak[57,101] to modestly bright at best[99,102,103], in stark contrast to the more than 28-fold brightening observed here.

2.3.2 Calculation results and explanations of the brightening effect

We attribute the observed anomalous brightening to the creation of a new, low-lying bright defect state that allows the previously inaccessible, presumably more populated low-lying excitons to be harvested through defect-enhanced exciton-phonon coupling (Figure 2-1). Covalent bonding of an aryl functional group to nanotube sidewalls introduces an sp^3 defect in the sp^2 carbon lattice. This defect causes a considerable perturbation in local electronic properties[104] while coupling strongly to the lattice vibrations, giving rise to a symmetry-breaking, defect-induced Raman scattering (D phonon, ~1,300 cm^{-1})[64,105]. The intensity of this Raman band with respect

to the in-plane stretching mode (E_{2g}) of the sp^2 bonded carbon lattice (G band, ~1590 cm^{-1}) is roughly proportional to the degree of diazonium functionalization (Figure 2-4).

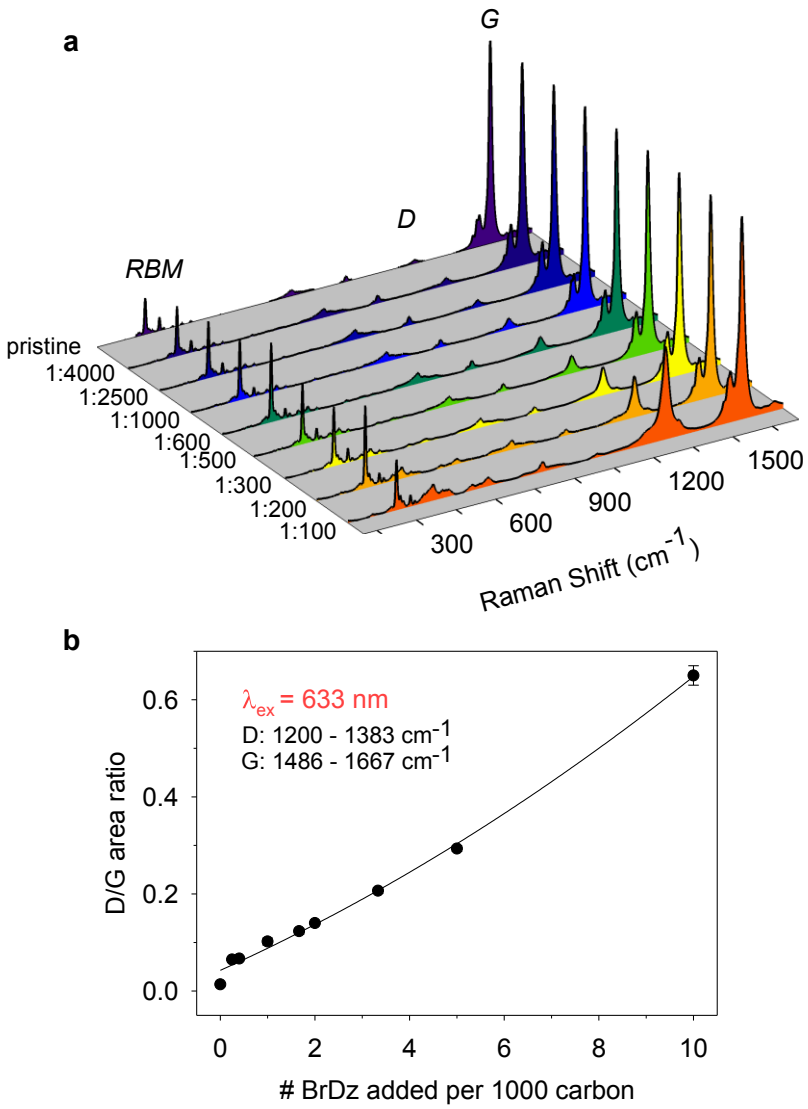

Figure 2-4 Raman spectra of (6,5)-C6H4Br. (a) Raman spectra of (6,5)-enriched solutions after reacting with BrDz at different [Dz]:[C] molar ratios. (b) Raman D/G area ratio increases monotonically as a function of [Dz]:[C] molar ratios.

To elucidate the molecular origin of this defect state, we calculated the electronic structure of an aryl-functionalized 4-nm long (6,5)-SWCNT using BP86 density functional theory (DFT) (Figure 2-5). The highest occupied molecular orbital (HOMO) and the lowest unoccupied molecular orbital (LUMO) of a pristine nanotube are two-fold degenerate. In the presence of an aryl functional group we found a substantial split (105-326 meV) in the frontier orbital energy levels, regardless of where the pairing H is attached (Table 2-4 and Figure 2-12 in Supporting Information). Similar splitting is found in oxygen-doped (6,5)-SWCNTs[99], although semi-empirical PM3 modeling suggests that the oxygen atom is incorporated into the carbon lattice without breaking sp^2 hybridization, which makes it structurally different from the sp^3 defect considered here. The splitting of E_{11} gives rise to two dipole-allowed optical transitions, E_{11}^- and E_{11}^+. These two optical transitions have not been experimentally confirmed in oxygen-doped SWCNTs, probably due to low concentrations of the oxygen defects or the different chemical nature of the defects. However, under our experimental conditions, as more $C_6H_4NO_2$ is covalently added to the nanotube sidewall, the splitting features grow more prominent at a peak position that is red-shifted by 48 meV from the phonon sideband, which is 133 meV lower than the E_{11} emission energy[106,107]. This feature allows us to identify these transitions in correlated absorption and fluorescence spectra, and thereby to determine the energy levels of E_{11}^- and E_{11}^+ (Figure 2-6 (a)). We found that E_{11}^- and E_{11}^+ split asymmetrically about the bright E_{11} exciton, giving rise to one peak (E_{11}^-) 181 meV below E_{11} in both PL and absorption spectra, and another peak, E_{11}^+, 225 meV above the bright exciton. The E_{11}^- absorption occurs at exactly the E_{11}^- PL energy.

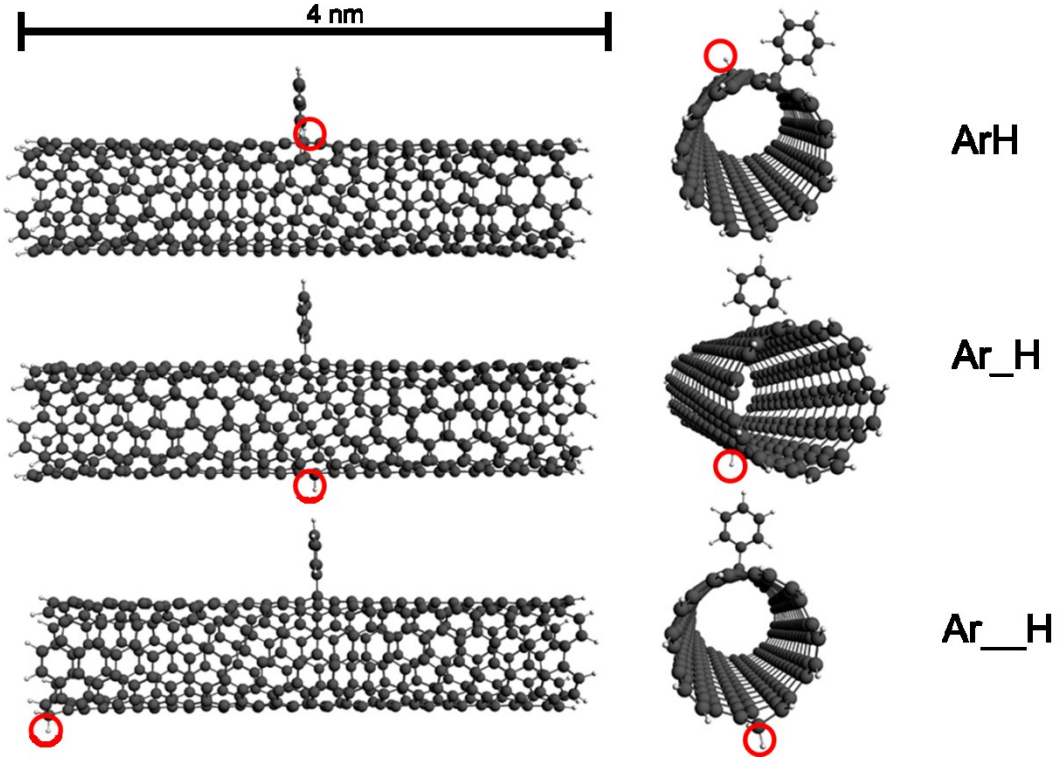

Figure 2-5 Optimized structures of (6,5)-C_6H_5 at BP86 density functional theory levels. The SWCNT is 4 nm long, with hydrogen-terminated ends. The aryl group is covalently attached in the middle of the nanotube sidewall. To avoid open shell structure, a hydrogen atom is added to the para position (ArH), at the farthest point along the radial direction (Ar_H), or at the end of nanotube, creating a CH_2. The calculations were performed using the Amsterdam Density Functional package. A DZP Slater basis set with a frozen 1s core was used for carbon.

The red shift of E_{11}^- from E_{11} shows a $1/d^2$ dependence (where d is nanotube diameter) combined with a dependence on nanotube family in which the SWCNTs are grouped by mod(n-m)=1 or 2 (Figure 2-6 (b), Figure 2-14 in Supporting Information). These trends are remarkably similar to what was predicted by Louie et al.[12] for dark

excitons. Notably, the energy difference between E_{11}^- emission and the predicted low-lying singlet dark exciton approximates the energy of the observed D-phonon (1301 cm^{-1}; 161 meV), suggesting a vibronic coupling mechanism for internal conversion. As the nanotube diameter increases, this energy matching relation gradually transitions from low-lying dark excitons to the K-momentum dark exciton that resides ~25 meV above the bright E_{11} exciton.

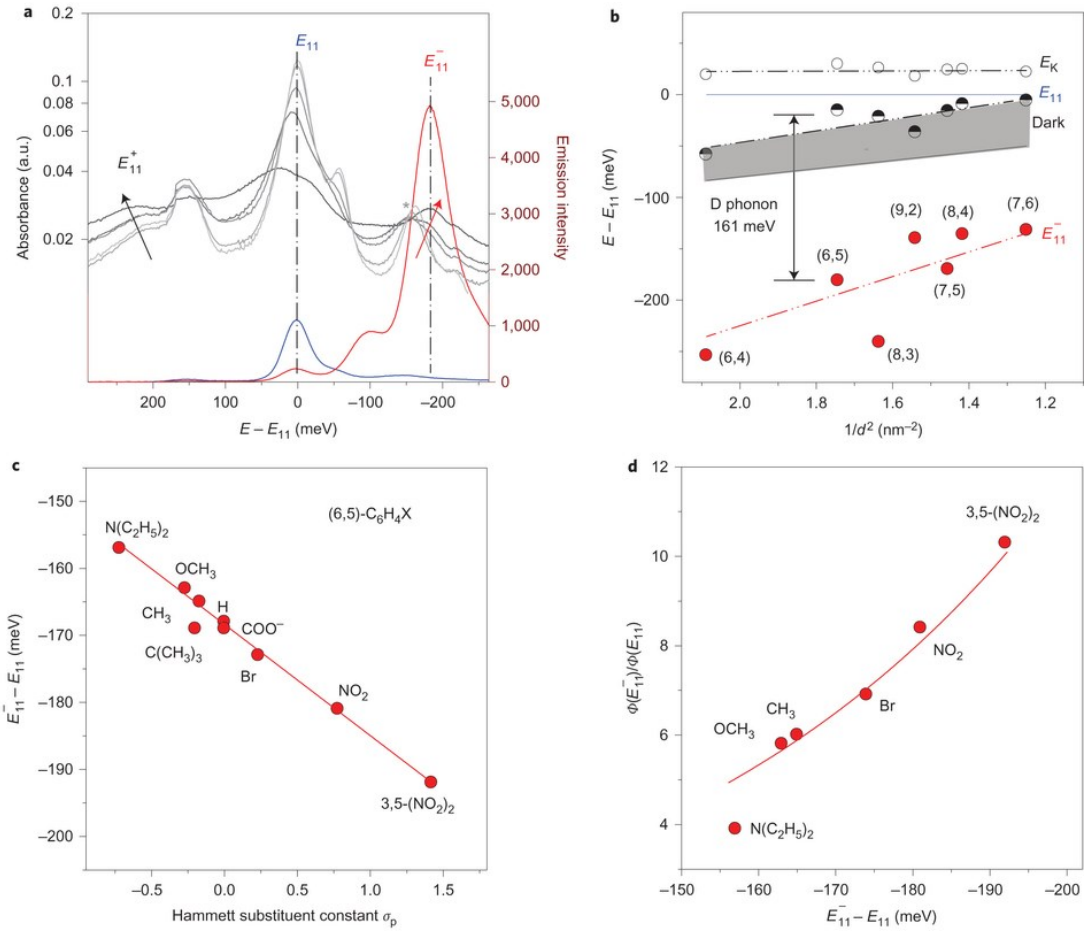

Figure 2-6 Experimental evidence of low-lying dark exciton brightening. a, Correlated visible near-infrared absorption (gray to dark lines) and PL (colored) spectral evolution revealed energy splitting of E_{11} frontier orbitals in (6,5)-$C_6H_4NO_2$. The arrows highlight the rising of E_{11}^+ and E_{11}^- as the degree of functionalization increases. The asterisk denotes the phonon sideband of K-momentum exciton. Unlabeled peaks are

due to trace (6,4) and (8,3). For PL the SWCNTs were resonantly excited at the E_{22} transition. b, Experimentally observed PL energy shifts (red dots and lines) show chirality dependence and family behavior (grouped by mod(n,m)=1 or 2 as highlighted by the dashed lines) that are consistent with theoretically predicted dark exciton energy (black symbols), plotted using analytical forms proposed by Louie *et al.*[93]. Resonant exciton-phonon coupling occurs when the energy difference between E_{11}^- and dark states matches the energy of a D-phonon. The coupling gradually transitions from the low-lying singlet dark exciton in small diameter SWCNTs to the K-momentum exciton in larger diameter SWCNTs. c, The new PL peak of covalently functionalized (6,5)-SWCNT occurs at a red-shifted energy that is linearly correlated with the Hammett substituent constant of the terminating moieties on the aryl functional group. d, The maximum PL brightening, $\Phi(E_{11}^-)/\Phi(E_{11})$, of covalently functionalized (6,5)-SWCNTs increases exponentially as a function of the red-shifted energy.

These energy relations strongly suggest that the bright E_{11}^- emission in (6,4) and (6,5) arise mainly from brightening of low-lying dark excitons due to sp^3 defect-enhanced exciton-phonon coupling. The dark excitons, like the bright ones[100], may migrate to a defect site and emit through the new, optically-allowed state. In (6,5)-SWCNTs, resonant coupling between the D-phonon and the less populated K-momentum dark exciton, which lies ~25 meV above the bright E_{11} exciton, gives rise to a relatively weak sideband red-shifted 133 meV from the E_{11} emission[106,107]. Coupling to the low-lying dark excitons, which lie ~5-100 meV below the bright E_{11} exciton, is made possible in the aryl-functionalized (6,5)-SWCNTs because of the considerably lower energy level of the E_{11}^- state. This coupling gives rise to the observed substantial brightening in E_{11}^- PL and more red-shift in emission energy (181 meV vs. 133 meV). In the two larger diameter nanotubes investigated, (7,6) and (8,4),

the E_{11}^- state lies at an energy level too high to allow phonon coupling to the significantly more populated low-lying dark states, thereby leading to the observed negligible brightening in the covalently functionalized nanotubes (Table 2-2 and Figure 2-14 in Supporting Information).

We further show that it is possible to control the energy level of the LUMO (or HOMO) of the defect site by adding electron-withdrawing (or electron-donating) substituents to the aryl functional groups, such that both the E_{11}^- emission energy and PL efficiency can be chemically tailored (Figure 2-7 and Figure 2-13, 2-14 in Supporting Information). Table 2-3 lists 9 different substituent groups that we were able to add to the aryl functional groups by custom synthesis. The new PL peak of aryl-functionalized (6,5)-SWCNTs occurs at a red-shifted energy that is linearly correlated with the Hammett constant[108], which characterizes the electron donating or withdrawing capability of the substituent group (Figure 2-6 (c)). This trend of lowered frontier orbital energy levels is consistent with those observed in conjugated polymers[109], in which electron-withdrawing groups push down the energy level of the LUMO. The observed large range of chemically tunable energy shifts, over 35 meV, is comparable to the bright-dark splitting. Consistently, we found that the maximum PL brightening, $\Phi(E_{11}^-)/\Phi(E_{11})$, of the covalently functionalized (6,5)-SWCNTs increases exponentially as a function of the red-shifted energy, E_{11}-E_{11}^-, closely following the Boltzmann distribution (Figure 2-6 (d) and Figure 2-7). The only deviating data point, $N(C_2H_5)_2$, has an energy shift that is slightly smaller than the D-phonon energy, suggesting a non-resonant, weaker phonon coupling to the low-lying dark excitons. Hence, the chemical nature of the functional groups may induce subtle differences in

the defect energy level that significantly affects the exciton dynamics. Although there are theoretical predictions of nanotube brightening[102,110], both the high strength of brightening and the extreme sensitivity to the functional groups that we observe in this study were not anticipated.

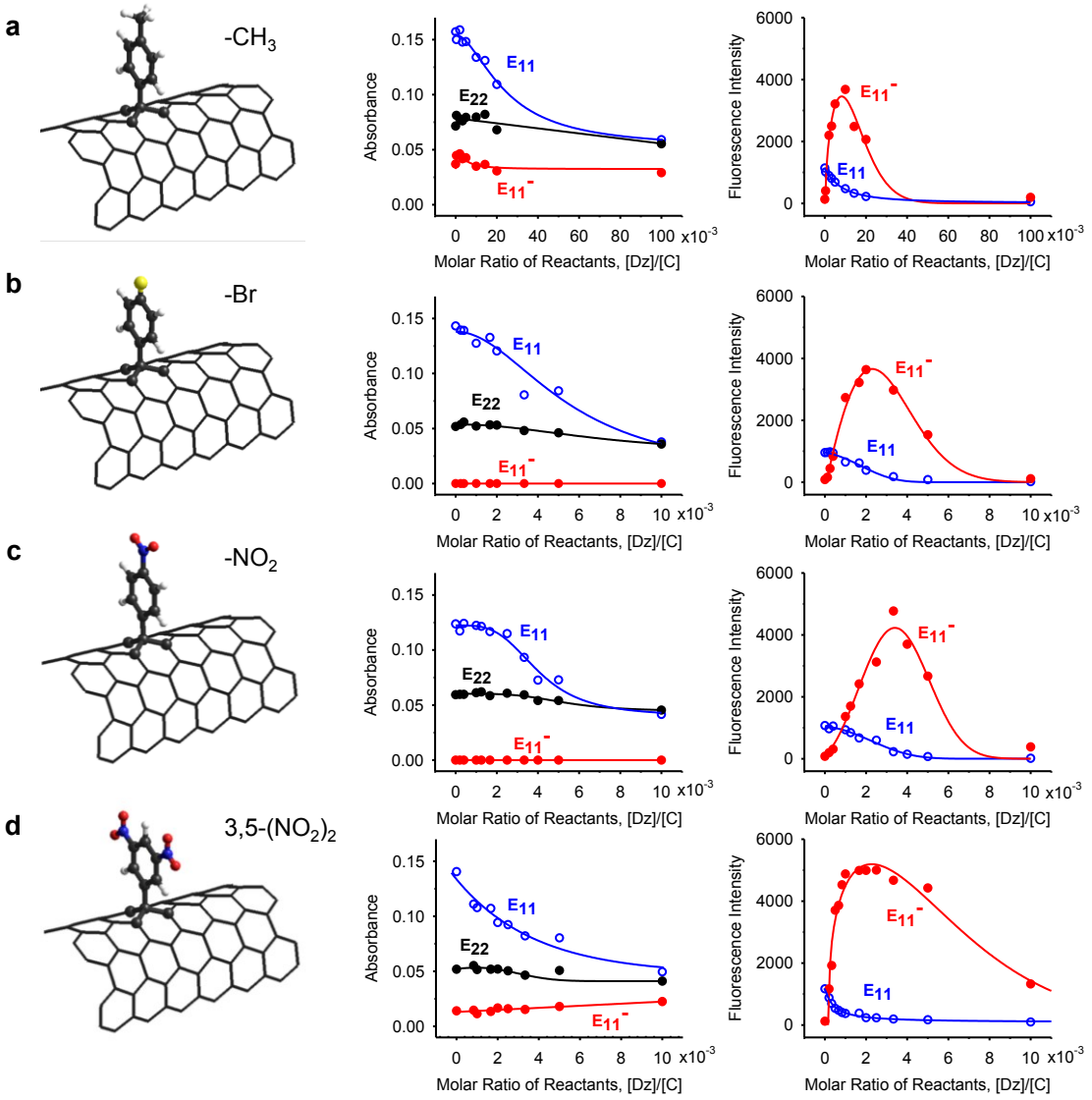

Figure 2-7 Absorption and PL spectral evolution of (6,5)-SWCNTs covalently functionalized with (a) CH_3, (b) Br, (c) NO_2, and (d) 3,5-$(NO_2)_2$, substituted aryl

functional groups. Shown in the left panels are molecular models of the covalently functionalized nanotube structures. The plots depict peak absorbance (middle panels) and emission (right panels) as a function of [Dz]:[C] molar ratio of reactants. The time of reaction is 240 hours.

2.4 Conclusions

In summary, we found substantially enhanced PL in semiconducting SWCNTs that are covalently functionalized with a controlled number of aryl functional groups. Both the emission energy and the maximum PL brightening are chemically tunable using electron withdrawing/donating substituents on the aryl functional group. These phenomena can be understood based on emission from states in which sp^3-defect enhanced exciton-phonon coupling brightens a low-lying dark exciton state. This work has thus opened the door to harvesting dark excitons in SWCNTs. The controlled functionalization fundamentally alters the optical and correspondingly, electronic properties of carbon nanotubes in a highly predictable manner. We expect these findings will broadly impact existing near-infrared fluorescence imaging and optoelectronics applications and may lead to new single photon sources and quantum devices where chemical control of the quantum state of defects would be highly desirable.

2.5 Supporting Information

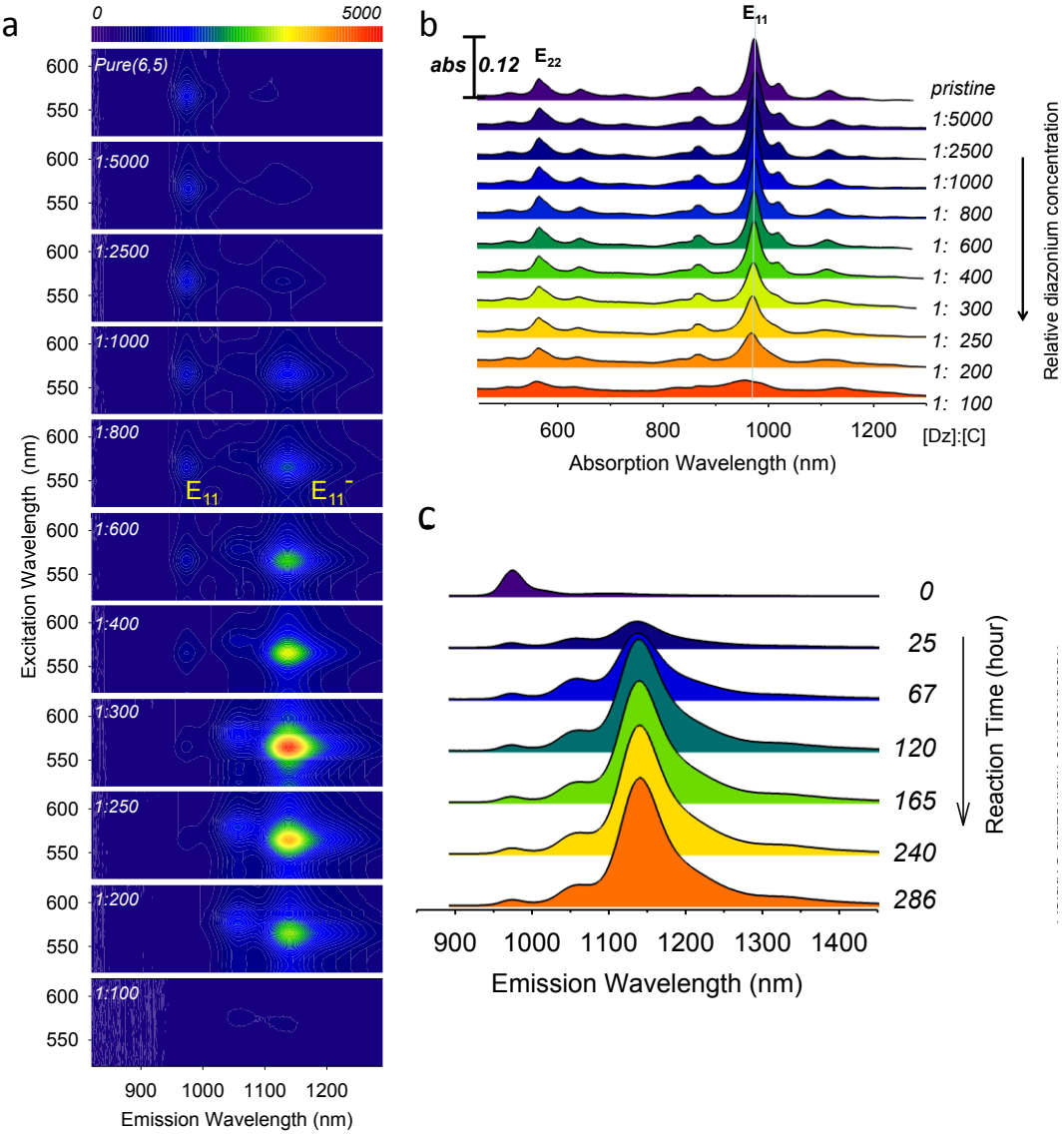

Figure 2-8 (a) The rise of E_{11}^- PL in NO_2-Dz functionalized (6,5)-SWCNTs. Excitation-emission PL maps of (6,5)-enriched SWCNT solutions covalently functionalized with increasing [Dz] : [C] molar ratio of 4-nitrobenzenediazonium tetrafluoroborate to SWCNT carbon for 268 hours. (b) Absorption spectral evolution of NO_2-Dz functionalized (6,5)-SWCNTs. Visible-NIR absorption spectra of (6,5)-enriched SWCNT solutions after reacting with increasing relative concentrations of 4-

nitrobenzenediazonium tetrafluoroborate for 268 hours. (c) Evolution of E_{11}^- emission as (6,5)-SWCNTs reacts with NO_2-Dz at a 1:300 [Dz]:[C] molar ratio of starting reactants. The PL intensity of E_{11} emission dropped significantly within 25 hours, while E_{11}^- emission peak gradually grew to approximately 5 times that of the original E_{11} after 240 hours. The asterisked peaks are due to trace (6,4)-SWCNTs in the solution.

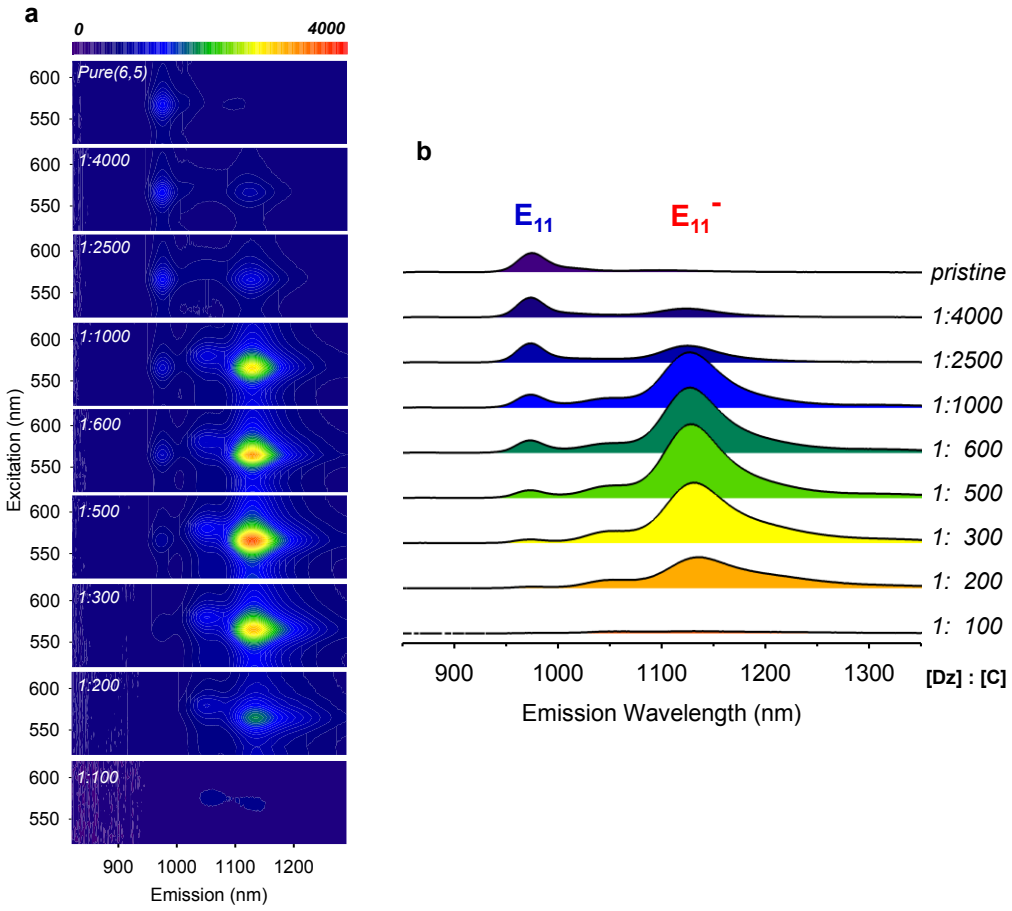

Figure 2-9 (a) Excitation-emission PL maps of (6,5)-enriched SWCNT solutions covalently functionalized with increasing [Dz] : [C] molar ratio of 4-bromobenzenediazonium tetrafluoroborate to SWCNT carbon at 240 hours. (b) Emission spectra extracted from the maps at 565nm excitation.

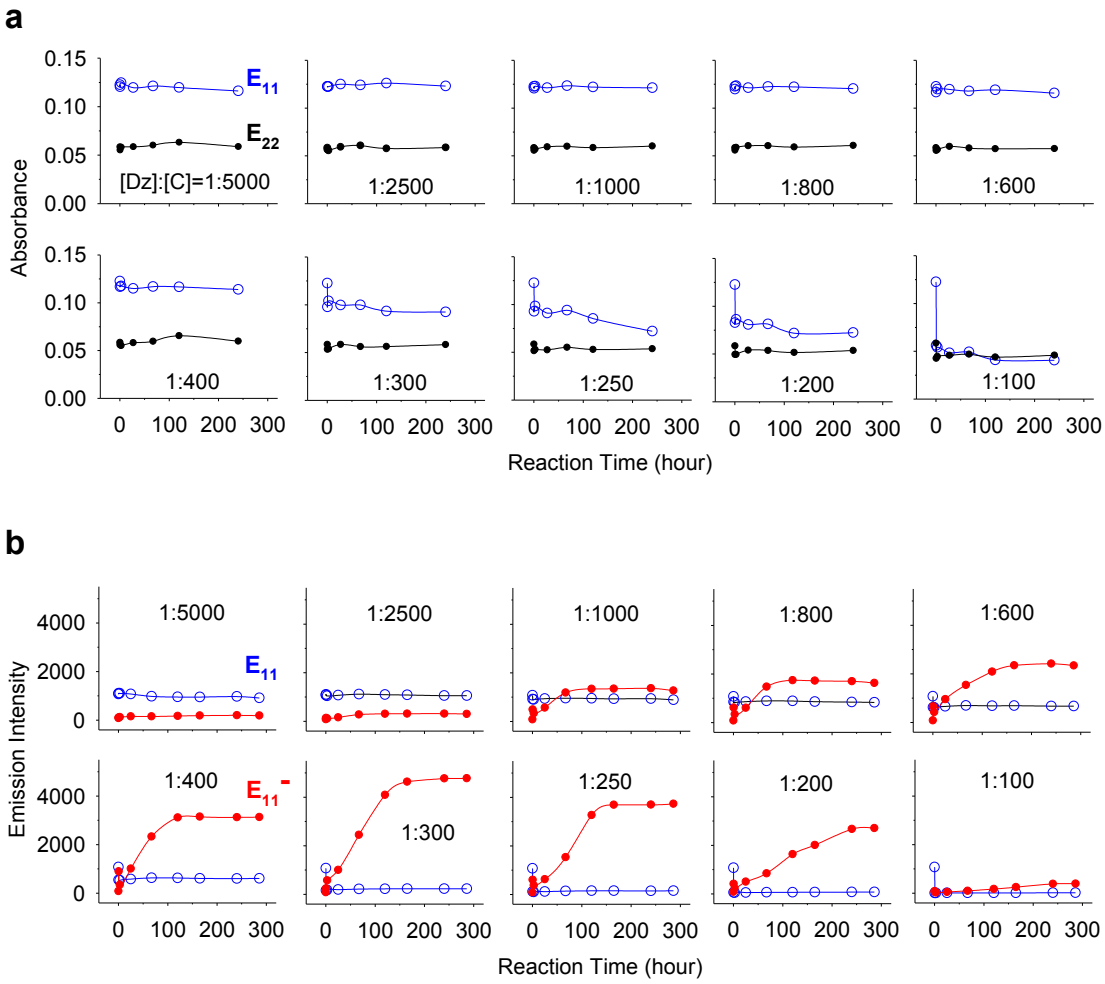

Figure 2-10 Spectral evolution of (a) E_{11} and E_{22} absorbance, and (b) E_{11} and E_{11}^- emission of (6,5) as a function of reaction time with nitrodiazonium at increasing [Dz]:[C] relative molar concentration of 4-nitrobenzenediazonium tetrafluoroborate. The peak intensity of E_{11} emission dropped immediately upon addition of diazonium and remained stable for all samples; E_{11}^- peak intensity grew gradually until saturated at a high concentration.

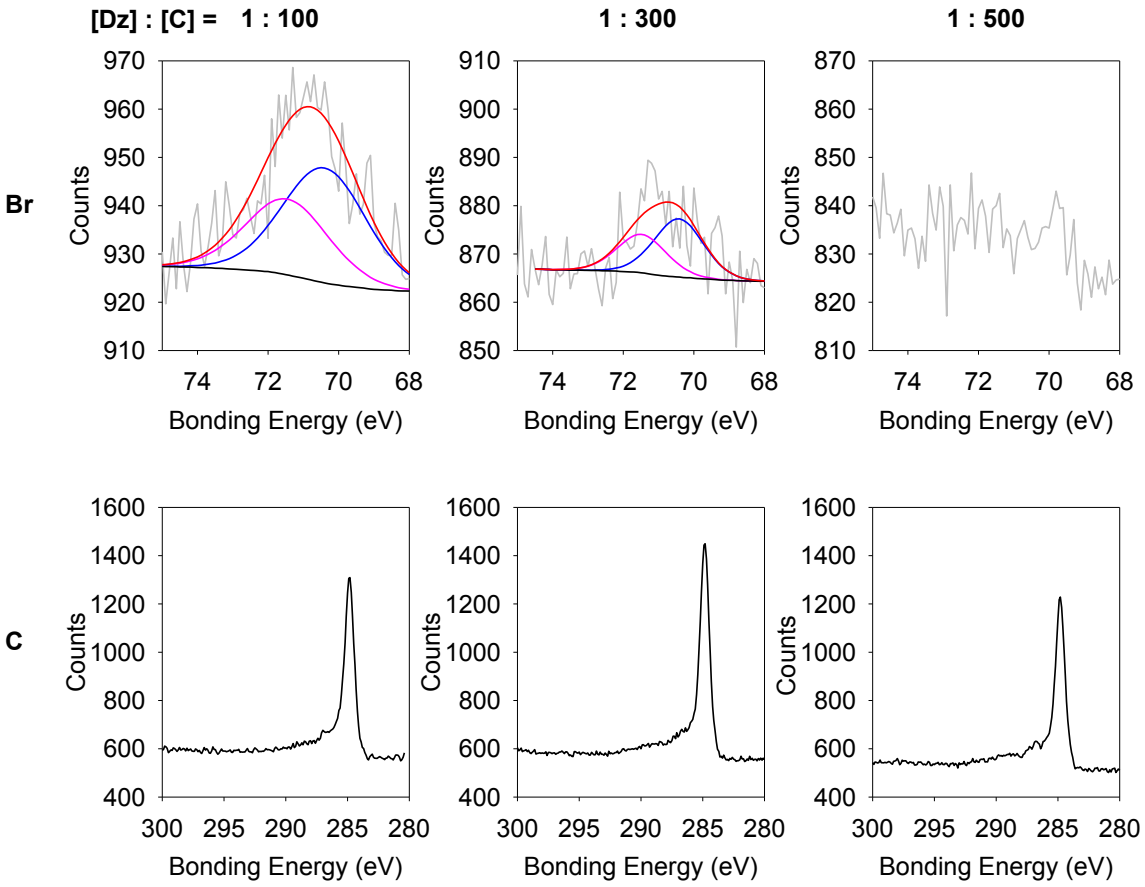

Figure 2-11 XPS spectra of (6,5)-C_6H_4Br. The covalently functionalized samples show a decreasing intensity of Br relative to carbon at decreasing [Dz]:[C] molar ratios of starting reactants.

Table 2-4 Orbital energies of the three functionalized (6,5) structures considered in Figure 2-5 (unit: eV).

Molecular Orbital	Pristine	ArH	Ar_H	Ar__H
HOMO-1	-5.995	-5.964	-5.954	-5.912
HOMO	-5.973	-5.859	-5.789	-5.586
LUMO	-4.924	-5.010	-5.254	-5.391
LUMO+1	-4.908	-4.809	-4.806	-4.819

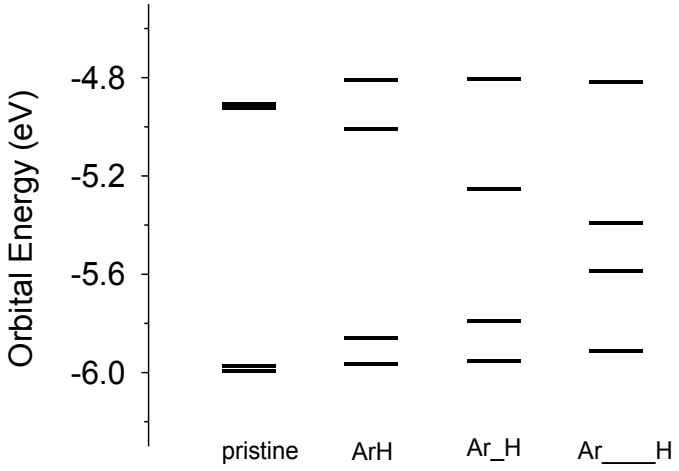

Figure 2-12 The doubly degenerate frontier orbitals in a nanotube split regardless of the positions of the functional groups.

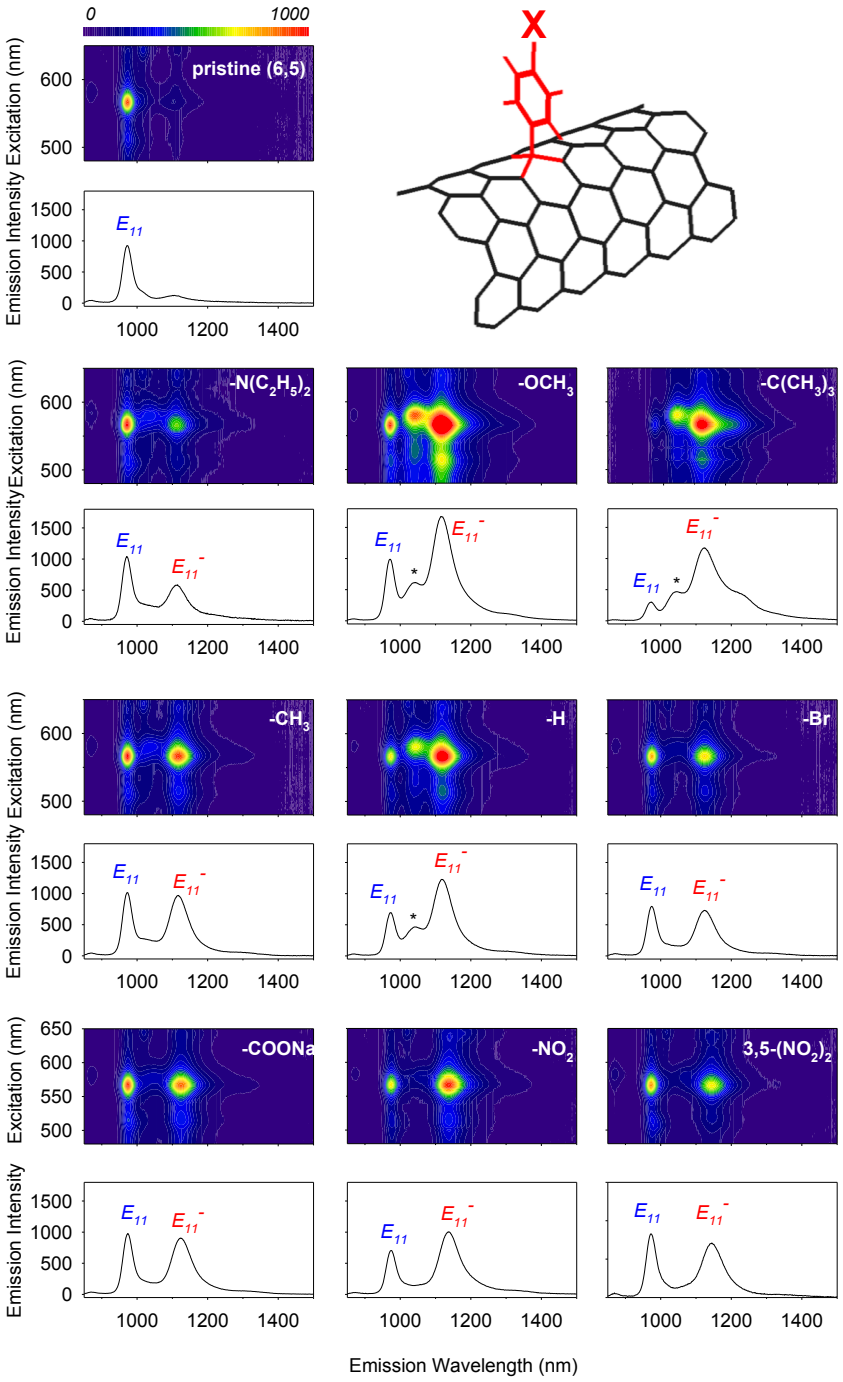

Figure 2-13 Excitation-emission maps and fluorescence spectra of (6,5)-C_6H_4X, where X=$N(C_2H_5)_2$, OCH_3, $C(CH_3)_3$, CH_3, H, Br, COONa, NO_2, and 3,5-$(NO_2)_2$, respectively, in comparison with those from the pristine starting (6,5)-enriched SWCNT solution. Note that the asterisk denotes E_{11}^- emission from (6,4).

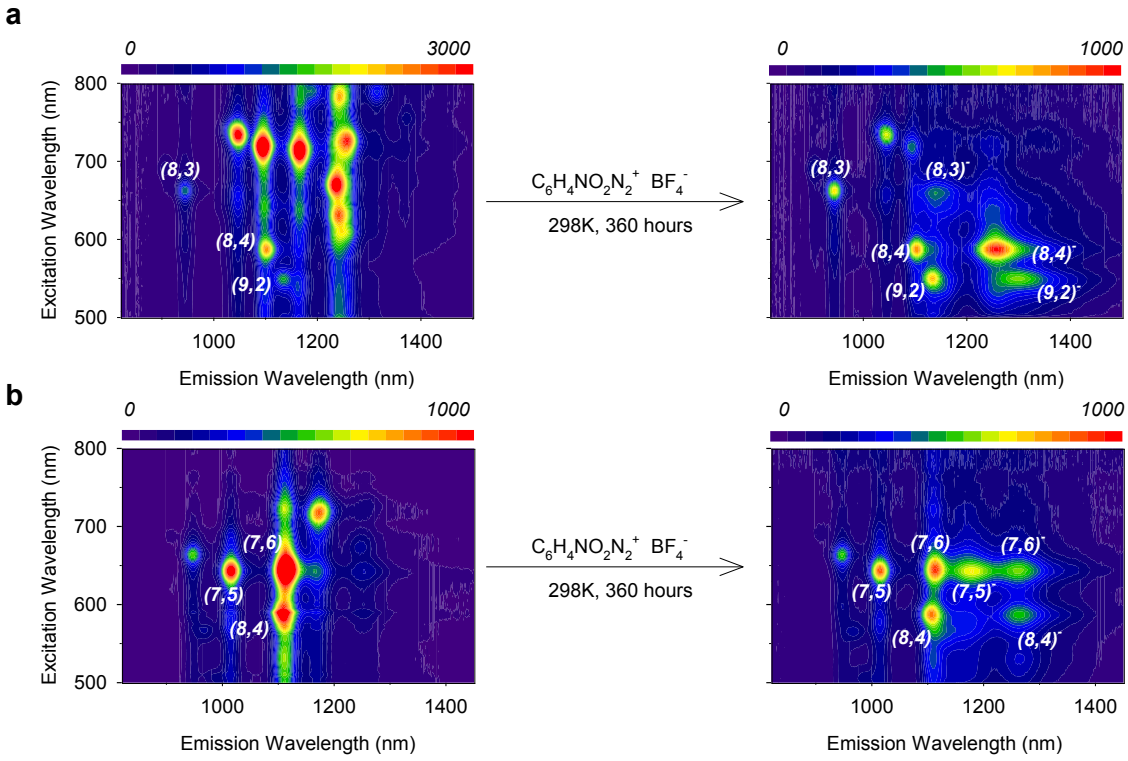

Figure 2-14 Excitation-emission fluorescence maps of chirality-enriched samples, (a) CES1 and (b) CES2, before and after reacting with NO_2-Dz for 360 hours.

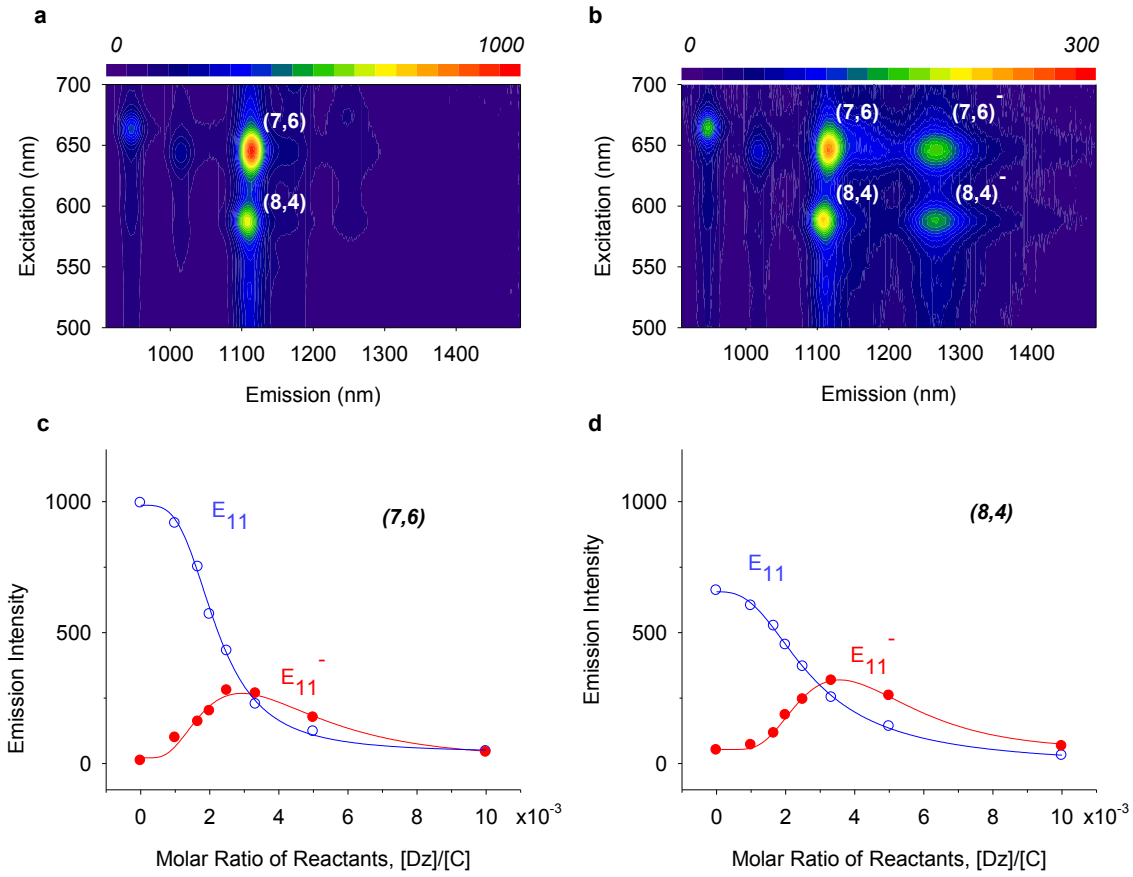

Figure 2-15 Spectral evolution of (7,6) and (8,4)-SWCNTs as a function of [Dz]:[C], molar ratio of NO_2-Dz to nanotube carbon. The excitation-emission PL maps of (7,6) and (8,4)-SWCNTs before (a) and after (b) reacting with NO_2-Dz at a 1:400 [Dz]:[C] molar ratio of reactants for 3 months. (c, d) PL intensity evolves as a function of molar reactant ratio.

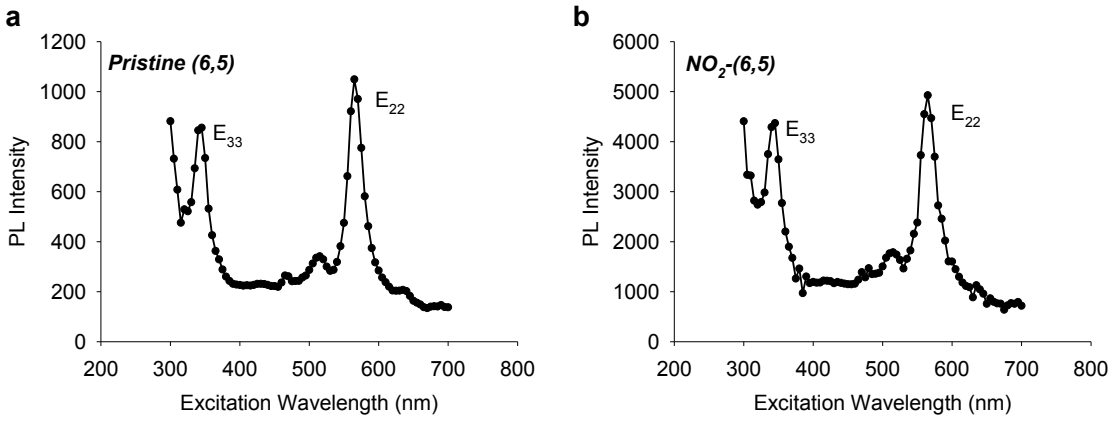

Figure 2-16 Excitation spectra of pristine (6,5) (a) and NO_2-(6,5) (b) at 976and 1134nm emission wavelength, respectively.

3 Optical and Electrical Properties of Inner Tubes in Outer Wall-Selectively Functionalized Double-Walled Carbon Nanotubes

Adapted from Piao, Y.; Chen, C. F.; Green, A. A.; Kwon, H.; Hersam, M. C.; Lee, C. S.; Shatz, G. C.; Wang, Y. J. Phys. Chem. Lett. 2011, 2, 1577-1582

Y.P and C.F.C contribted equally to the work. Y.W., Y.P. conceived and designed the experiments. Y.P., C.F.C. and H.K. performed experiments. N.V. and G.C.S. performed DFT calculations. A.A.G and M.C.H. purified the DWCNTs. Y.W., Y.P. wrote the manuscript with inputs from all authors.

3.1 Introduction

A DWCNT is composed of exactly two concentric nanotubes separated by 0.37±0.04 nm, approximately the distance between two graphitic layers[37,111]. This emerging class of carbon nanomaterials has interesting structures and properties[36]. Recent experiments suggest that DWCNTs exhibit superior thermal[112] and mechanical properties[113] as compared to single-walled carbon nanotubes. The two walls have optical properties and Raman scattering characteristic of each wall[37,114,115]. Theoretically, if the two constituent walls are not strongly coupled each wall should behave like a SWCNT. Like a SWCNT, the structure of each wall can be uniquely indexed by a pair of integers, (n,m). For randomly distributed (n,m) values, each wall will have approximately 2/3 probability of being a semiconductor and 1/3 of being a metal. Experimental and theoretical studies however, suggest complicated overall electrical behavior[116], even when both constituent walls are semiconductors, a DWCNT may behave as a metal[117,118].

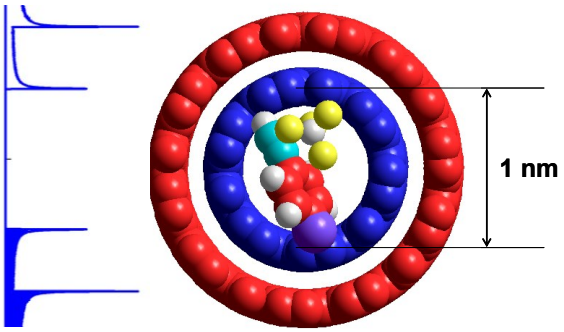

Figure 3-1 Scheme DW and diazonium

Herein, we report that 4-bromobenzenediazonium tetrafluoroborate reacts with the outer wall of DWCNTs selectively to the exclusion of the inner tube, resulting in significantly simplified van Hove absorption spectra and Raman scattering from inner tubes after the outer walls are heavily functionalized. This effect is evidenced in correlated optical absorption spectroscopy, resonance Raman spectroscopy and electrical transport measurement of thin film networks in comparison with SWCNTs. Unambiguous assignment of the spectroscopic features to each wall were made possible by the use of purified DWCNT samples, free of SWCNTs, multiwall nanotubes (MWNTs) and other by-products, prepared using a density gradient ultracentrifugation (DGU) technique[37].

3.2 Materials and Methods

Nanotube Materials. High purity DWCNTs were separated from a CVD grown sample (Unidym DW411UA) using DGU as previously reported.[37] The sorted DWCNTs have an average diameter of 0.86 nm and 1.61 nm for the inner and outer wall nanotubes, respectively.[37] Arc discharge and HiPco SWCNTs were used as

controls because their diameters are comparable to those of the outer walls and inner tubes of the sorted DWCNT sample, respectively. A stock solution of individually dispersed SWCNTs was prepared using a procedure derived from a previous publication[1]. Raw SWCNTs (10 mg, HiPco Lot R0513 or Sigma Aldrich arc discharge Lot 698695) were dispersed in a 25 mL D_2O solution of 1% sodium cholate (≥99.9% Sigma Aldrich) by tip-sonication (MISONIX ultrasonicator operated at a power level of 17 W) in a cooled (15^0C) stainless steel cup for 2 hours. The nanotube dispersion was centrifuged at 64,700 g for 2 hours (Beckman Coulter Optima LE-80K; 70 Ti fixed angle rotor) and the top 2/3 of the supernatant was collected. The concentrations of the SWCNT dispersions were adjusted with 1% sodium cholate D_2O solution to a similar optical absorbance (O.D. ~ 0.2 @ 1000 nm) as that of the DWCNT solution.

Diazonium Functionalization of CNTs. DWCNTs and SWCNTs solutions, each 15 mL, were kept in glass vials covered with aluminum foil. To each sample was added 70.8 μL of 0.10 M diazonium solution (~0.5 mM, approximately 1 molar equivalent of carbon) that was freshly prepared from 4-bromobenzenediazonium tetrafluoroborate (96%, Sigma Aldrich) and deuterium dioxide (99.8%, Cambridge Isotope). This addition of diazonium salt was repeated three times after 24, 48, and 72 hours, and the reactions were monitored for a total of 7 days. The reactions were performed at room temperature with constant stirring. Exposure to light was limited by covering the vials with aluminum foil.

Spectroscopy Characterization. Raman scattering spectrum were collected on Horiba Jobin Yvon LabRAM Raman microscopes (mdoels HR800 and ARAMIS) with all available excitation lines including 632.8 nm, 532 nm, 514.5 nm and 488 nm. For

the reactions in solution, 0.3 mL CNTs solution was sampled at each reaction condition and allowed to precipate as cloud-like aggregates in 5 mL ethanol. The nanotube aggregates were transferred to a glass slide for Raman measurement. For each sample, Raman sepectra were taken from 4 – 5 different areas of the sample and averaged to minimize the effects of sample inhomogeneity. Absorbance spectra were measured using a Perkin Elmer Lambda 1050 UV/Vis/NIR Spectrophotometer with both PMT and InGaAs detectors.

Thin Film Electrical Transport Measurement. CNT networks on a glass/quartz substrate were prepared using a modified assembly method[111] which allowed deposition of mono- to few-layer random networks of CNTs from the individually dispersed nanotube solutions. The glass/quartz substrates were pretreated in a piranha solution (mixture of sulfuric acid and hydrogen peroxide at 3:1 volume ratio) at ~90˚C for 45 minutes and then rinsed with copious amount of nanopure water. The nanotube thin film samples were dried at 60^{o}C on a hot plate for 1 hr, after which the samples were immersed in ethanol for 10 minutes and then rinsed with Nanopure water to remove sodium cholate. After the samples were dried, Shipley S1813 photoresist was spin coated at 4000 rpm to form a ~1.3 μm thick protective layer on the nanotubes. Nanotube stripes of 10 or 25 μm in width were patterned using a standard photolithography process. The unprotected nanotubes were removed by oxygen plasma etching using a March Jupiter III oxygen plasma system (operated at 200 W and 50 sccm O_2 for 24 seconds). The photoresist was removed by dipping the samples in methanol and then isopropanol, followed by rinsing with Nanopure water. The fabrication process was monitored using a stereo microscope, Raman spectroscopy

and scanning electron microscopy to ensure a well-defined channel, completely removed unwanted nanotubes, with no damage to the nanotubes in the conducting channel. Electrodes were defined at both ends of the CNT stripes by e-beam deposition of Pd (30 nm)/Ti (1 nm) or Au (30 nm)/Ti (1 nm) through a shadow mask, followed by lift-off processes. The final nanotube channels were 10 or 25 μm wide with a length of 30, 50, 100 or 200 μm. The nanotube devices were functionalized by immersing the devices in a diazonium solution with increasingly reactive conditions (0.5 mM x 1-48 hrs, and 100 mM x 24 hrs at room temperature). The devices were cleaned with ethanol and Nanopure water, followed by drying with N_2. *I-V* curves were measured using an Alessi probe station equipped with an Agilent 4155C Semiconductor Parameter Aanalyzer.

3.3 Results and Discussions:

3.3.1 Absorption and Raman spectra of f-DWCNT

Diazonium chemistry was chosen to illustrate this concept because the chemistry has been well established in the case of SWCNTs[76,119,120] and successfully applied to SWCNT devices[121]. This chemistry has also been applied to investigate the fluorescence properties of inner tubes[122]. By following the structural evolution of the reacting DWCNTs with visible-NIR absorption spectroscopy and Raman spectroscopy, we were able to find the optimal reaction conditions that allowed functionalization of the outer wall to the highest degree possible by the diazonium chemistry. The reaching of a saturation point is evidenced by little further changes in both the optical absorbance and Raman intensity (*vide infra*) as more diazonium salts were added and the reaction time extended up to seven days. This saturation point is experimentally determined by

X-ray photoelectron spectroscopy (XPS) to be approximately 69 functional groups (covalently attached aryls) per 1000 surface carbons (see Supporting Information). The existence of such a saturation point is understandable since diazonium chemistry was mainly initiated by electron transfer from the nanotube to the diazonium precursors[76]. As the reaction proceeded, electrons in a nanotube will eventually deplete to a level low enough to prevent further reaction. Furthermore, steric hindrance likely limits the attachment of aryls to only a small fraction of the carbon sites.

The inner tube of a heavily functionalized DWCNT exhibits optical absorption, Raman scattering, and electrical conductivity strikingly similar to those of a pristine SWCNT. Figure 3-3 shows the visible-NIR absorption spectra of individually dispersed DWCNTs before and after reacting with 4-bromobenzenediazonium tetrafluoroborate to the highest degree possible by this chemistry. The pristine DWCNT sample shows various absorbance peaks from both outer walls and inner tubes of a variety of DWCNT structures. After functionalization, most absorption peaks diminished in strength, while the surviving ones became sharper. Under the same reaction conditions, SWCNTs lose all absorption peaks and become featureless in the absorption spectrum. This comparative study suggests that the diazonium reaction is surface limited, selectively functionalizing both SWCNTs and the outer wall of DWCNTs. The covalent modification eliminates the van Hove transitions in the outer walls, converting the DWCNTs to single-wall equivalents from the perspective of absorption spectroscopy.

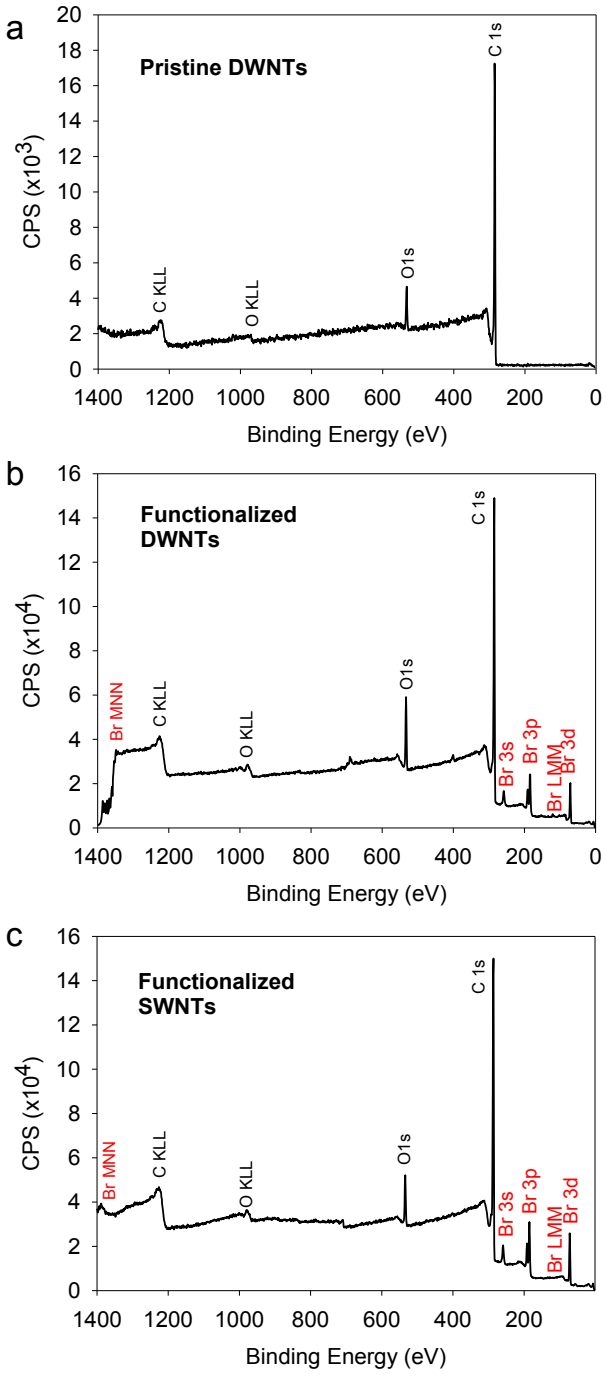

Figure 3-2 X-ray photoelectron spectroscopy (XPS) spectra for (a) pristine DWCNTs, (b) functionalized DWCNTs, and (c) functionalized HiPco SWCNTs. No bromine was observed in pristine DWCNTs sample. At the saturation point of diazonium functionalization, 69 functional groups (4-bromobenzene) per 1000 nanotube carbons were added to the outer walls, and 58 were added to the SWCNTs.

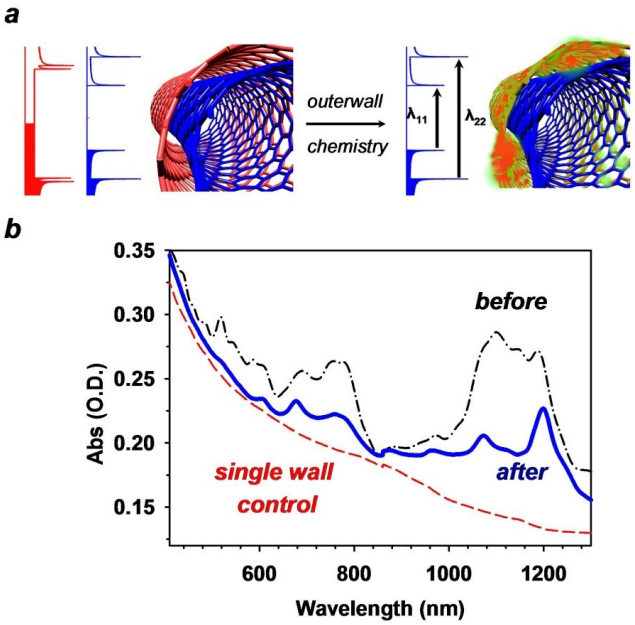

Figure 3-3 (a) Schematic of outer wall-selective covalent functionalization of DWCNTs. Illustrated is an example with a semiconducting inner tube and a metallic outer wall showing schematic density of electronic states. (b) Visible-NIR absorption spectra of DWCNTs before and after diazonium functionalization. The nanotubes were individually dispersed in D_2O solutions of 1% sodium cholate.

The corresponding Raman spectra of DWCNTs further support the presence of intact inner tube structures after the diazonium reaction (Figure 3-4). For a SWCNT, the most pronounced Raman signatures include a radial breathing mode (RBM) typically in the range of 100-350 cm^{-1}, tangential modes (G band) around 1500-1600 cm^{-1}, a disorder mode (D band) around 1310 cm^{-1}, and the second order harmonic of the D mode, known as the G′ mode, centered around 2600 cm^{-1} [105]. RBMs correspond to symmetric in-phase radial expansion and contraction of the nanotube, while the G band is related to the stretching mode of the C-C bond in the graphite plane. Covalent attachment of aryl functional groups to the nanotube sidewall introduces sp^3 defect

centers which activate the disorder mode (D band) and concomitantly depress the RBM, G and G′ modes due to reduced structural symmetry of the nanotube. A DWCNT displays two distinct sets of Raman signatures corresponding to the inner tube and outer wall, respectively. In particular, the inner tube and the outer wall have distinct RBMs positioned ~218*($1/d_{in}$-$1/d_{out}$) cm^{-1} apart because the low frequency Raman shifts are inversely proportional to the nanotube diameter[105,115]. With an average inner tube diameter of ~0.86 nm and outer wall diameter of ~1.61 nm in our samples, this corresponds to approximately 273 cm^{-1} and 155 cm^{-1}, respectively. After reaction with diazonium the RBM features for the outer walls completely disappear while the inner tube peaks remain almost unaffected (Figure 3-4, 3-5, 3-6). The retention of the inner tube RBM, G and G′ peaks and the concomitant disappearance of those of the outer walls, again suggest high outer wall selectivity of this diazonium chemistry.

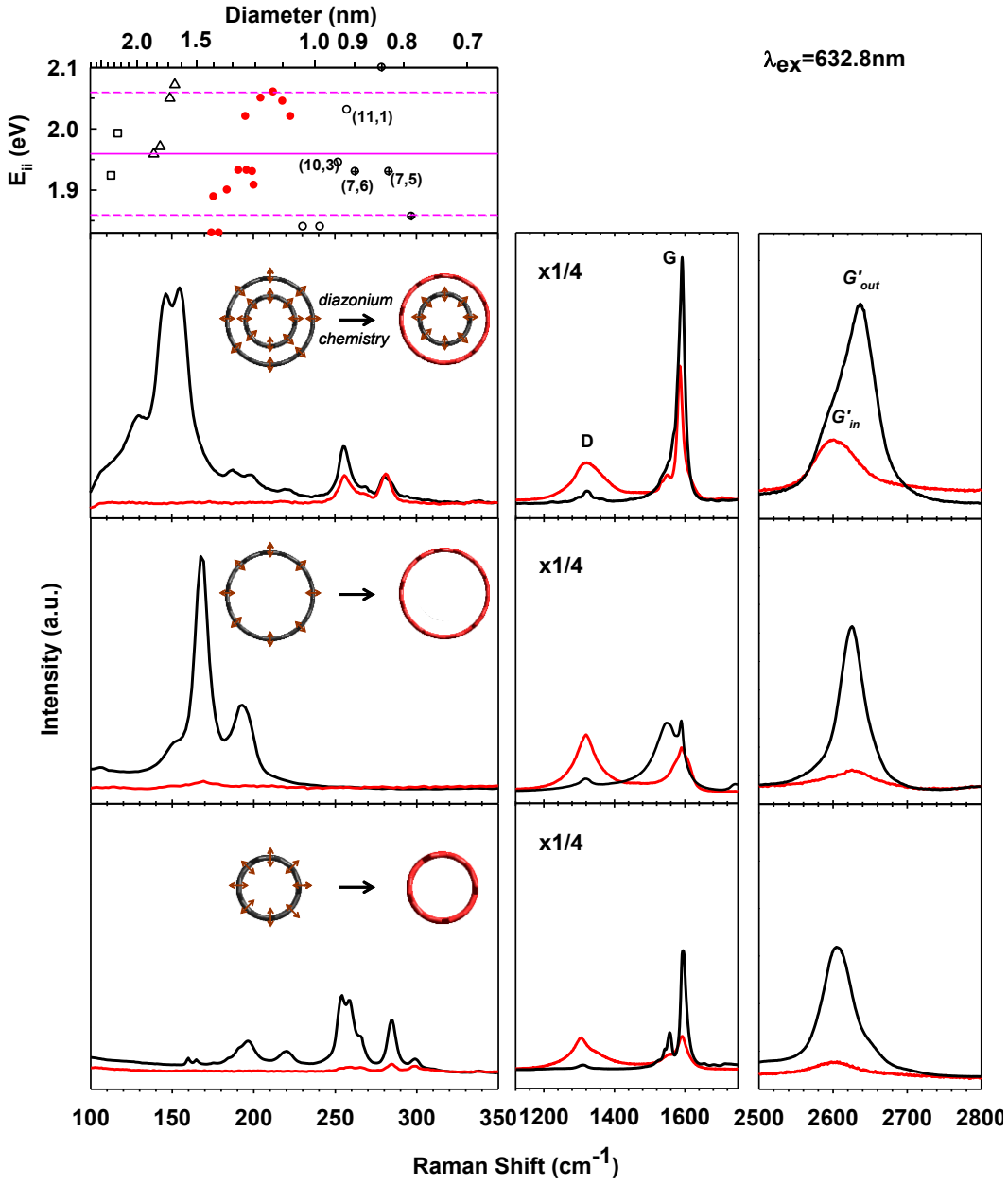

Figure 3-4 Comparative Raman spectroscopy studies of DWCNTs before and after functionalization by diazonium chemistry. The DWCNTs are compared with arc discharge SWCNTs and HiPco SWCNTs which have similar diameters to those of the outer walls and inner tubes, respectively. Insets are models showing the radial breathing modes before and after high degrees of diazonium functionalization. The excitation line is 632.8 nm and shown in the top panel is the Kataura plot for the corresponding excitation window.

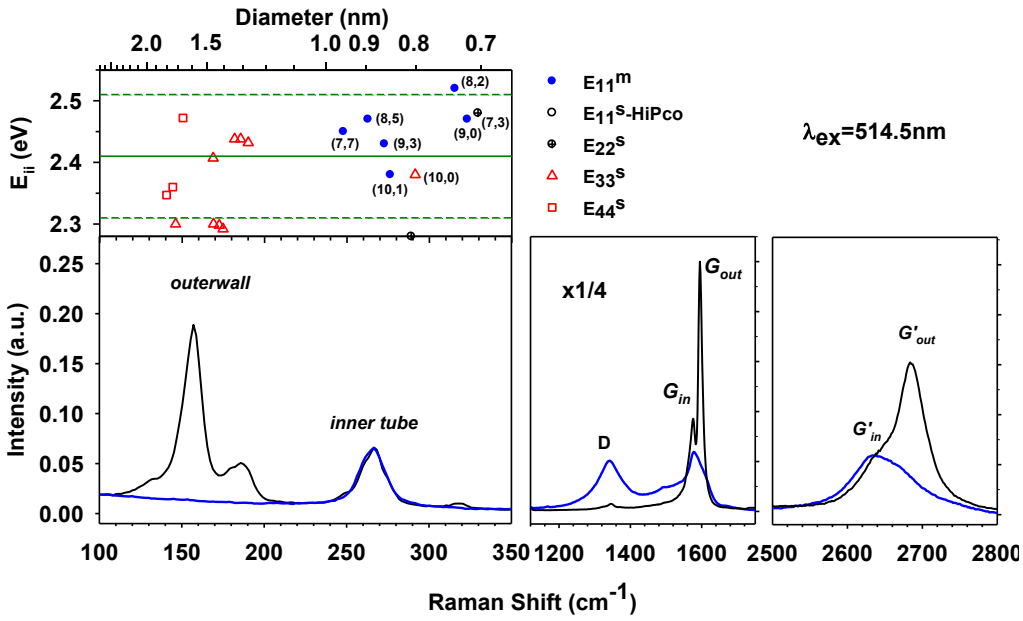

Figure 3-5 Raman spectra of DWCNTs before (black line) and after (blue line) functionalized by diazonium chemistry. The excitation line is 514.5 nm. The Kataura plot for the corresponding excitation window is shown.

It is important to note that for most DWCNT structures the outer wall and inner tube are not in the same resonance window[6]. The use of multiple laser lines and samples with a tight diameter distribution[1] are crucial for unambiguous assignment of the Raman spectra. Using an experimental Kataura plot which correlates electronic transitions and the RBM modes[123–125], we assigned the inner tubes within the Raman resonance window at 632.8 nm to semiconductors and at 514.5 nm to metals (Figure 3-4, 3-5, 3-6). The Raman spectra suggest that both semiconducting and metallic inner tubes are intact during the diazonium chemistry. Since diazonium is known to preferentially react with metallic SWCNTs[76] even under a concentration that is merely 5.3×10^{-13} M for 10 minutes[121], the preservation of metallic inner tubes after extensive reaction with more than 10^{10} higher concentration diazonium salts (0.005-0.1 M) for

extensive time (24 hours to 7 days) illustrates the robustness of the outer wall selectivity of the diazonium chemistry.

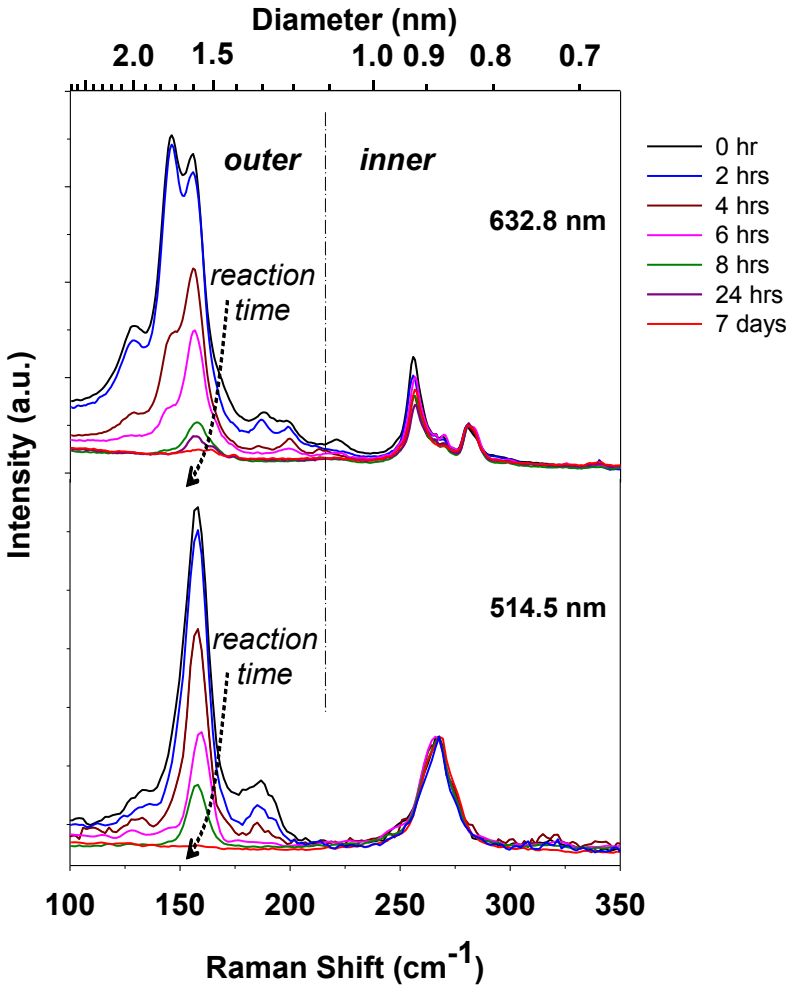

Figure 3-6 The evolution of Raman radial breathing modes of DWCNTs in the course of reacting with 4-bromobenzene diazonium salt over a time period of seven days. The outer wall RBMs decreased continuously until diminishing completely, while the inner tube survived intact. The excitation lines were 632.8nm and 514.5nm, respectively.

To more clearly see the correlation among the different features, we followed the evolution of the Raman radial breathing modes of the DWCNTs during the course of reaction with 4-bromobenzene diazonium salt over a time period of seven days (Figure

3-6). As the reaction proceeded, the RBM peaks of the outer walls continuously decrease until they vanish completely, while those from the inner tubes remain nearly unchanged. Similar trends were obtained by increasing the concentration from 1:1 to 1:100 carbon to diazonium molar ratio. Although Raman typically is not a quantitative method, the nearly unchanged inner tube intensity suggests that the inner tube can potentially serve as an internal standard to provide relatively quantitative information on the progress of reaction at the outer wall.

These spectroscopic studies unambiguously show that both the diazonium chemistry and the spectroscopic features of the inner tube can be cleanly decoupled from the outer wall. This observation is consistent with previous studies by others and us that suggest the inner tubes are generally protected from chemical doping[37,126], fluorination[127], and oxidation[128]. The outer wall selectivity can be attributed to the physical protection of the inner tube by the outer wall[37,126] and size exclusion from the small inner tubes. The DWCNT structures investigated in this study have small opening (< 1 nm) at the ends and high aspect ratio (>1,000)[37], which should significantly retard endohedral reactions[129] by minimizing diffusion of the reagents into the inner tubes. Unlike H^+ or F_2, a molecule as large as 4-bromobenzenediazonium tetrafluoroborate is unlikely to enter the open end of a 1 nm diameter inner tube. Even if it does, this relative large molecule is likely to covalently attach to the very end blocking entrance of more molecules. The use of diazonium chemistry, a covalent addition chemistry, rather than oxidation chemistry which tends to etch holes in the sidewall[128], further improves the outer wall selectivity. These mechanisms are consistent with the observed intact spectroscopic features from the inner tubes.

3.3.2 Electrical property of f-DWCNT network

The optical properties of inner tubes are corroborated with electrical properties that show markedly high conductivity compared to similarly functionalized SWCNTs. To probe the electrical properties of the inner tube, we have fabricated DWCNT thin film devices and measured their electrical conductivity before and after diazonium functionalization. It is well known that covalently attached functional groups strongly scatter electrons. A single defect can block one of the two transport channels of a SWCNT[30]. Because of the high degree of functionalization (approximately 69 functional groups per 1000 carbons based on XPS), it is not surprising that the SWCNT conductivity drops continuously as the reaction proceeds, until it is almost completely lost (Fig 4c). In stark contrast to SWCNTs, DWCNT devices retain a nearly constant conductivity, approximately 50% of the original value of each device after extensive diazonium functionalization (see Experimental Methods). This high retention is independent of the current level (which is proportional to the channel width and film thickness) and electrode materials (Pd vs. Au) (Figure 3-7 (d)). Pd provides ohmic contact for both semiconducting and metallic SWCNTs[130]. Hence, the observed high electrical retention is characteristic of the double-wall structure, not due to thin film inhomogenity or variation in contact resistance. Studies on multiwall nanotubes have shown that each wall can act as a conductive channel[131]. Similarly, the two walls that constitute a DWCNT presumably form two electrically conductive pathways. Diazonium functionalization selectively blocks the outer wall pathway, but the inner tube pathway survives intact. We note that a most recent work by Martel et al. has arrived at the same conclusion based on lightly functionalized DWCNT field effect

transistors using the same diazonium chemistry[132]. Our studies on nanotube networks (correlated with the spectral evolution of individually dispersed DWCNTs in solution) have further confirmed that the electronic properties of the inner tubes remain intact even at the saturation limit of the diazonium chemistry.

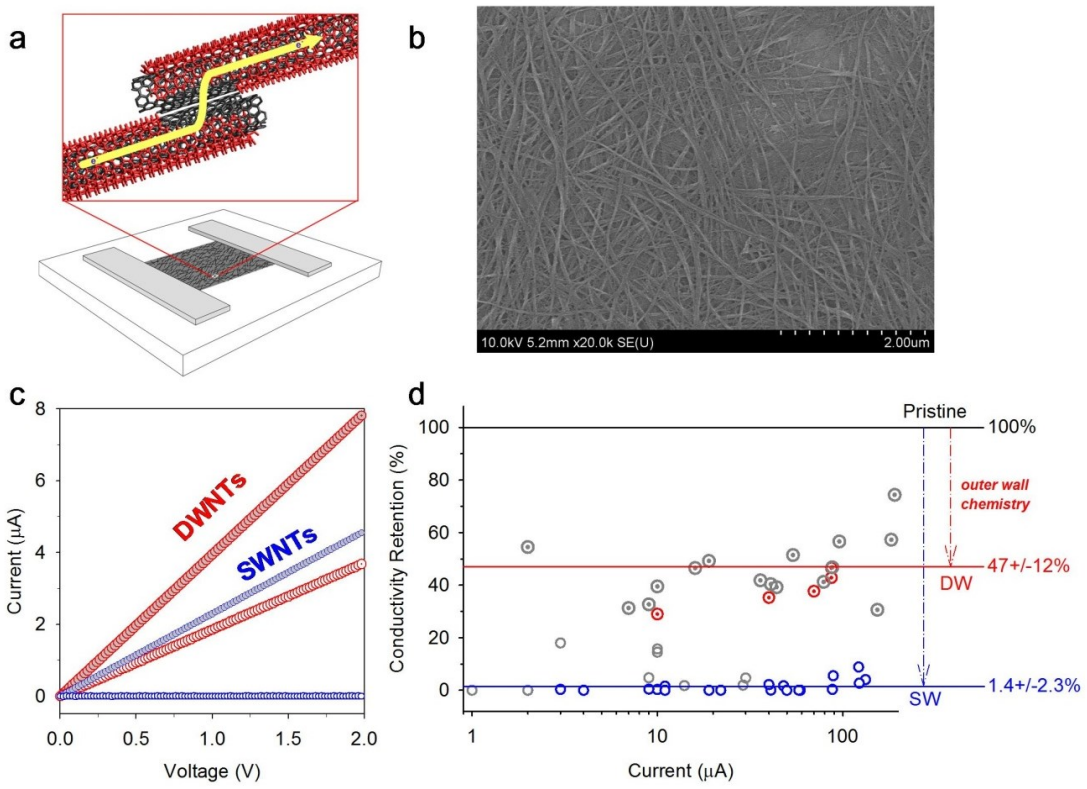

Figure 3-7 DWCNT thin films retain approximately 50% of the initial conductivity after extensive diazonium functionalization, in stark contrast to SWCNTs which became electrically insulating. (a) Schematic of a DWCNT thin film device with a conductive interface between two DWCNTs. (b) SEM image of the DWCNT network within a thin film device. (c) Representative *I-V* curves of DWCNTs and SWCNTs (HiPco) before and after diazonium functionalization. (d) The conductivity retention shows little dependence on the current level (at an applied voltage of 1.5 V) and the electrodes (gray circles: Pd electrodes; colored circles: gold electrodes). Shown are devices with nanotube channels of 200 μm (length) by 25 μm (width).

3.4 Conclusions

We have previously observed similar conductivity retention effects from outer wall selectively oxidized DWCNTs[128]. However, the contrast between DWCNTs and SWCNTs is 20 times higher than what we observed with oxidized DWCNTs. We attribute this improvement to two factors: (1) SWCNT-free, high purity DWCNT samples ensure the inner tube conductive pathway. (2) The contact between two bundled/branching DWCNTs is protected from diazonium attacks, providing better electrical contacts than is possible by post-functionalization assembly (Fig 4a). This picture is consistent with previous theoretical prediction based on density functional theory that the unoccupied molecular orbital at the edge of a functionalized region is delocalized between the inner and outer shell providing a low energy pathway for electrons to transport between the outer and inner tubes[133]. Interestingly, although inhomogeneity in thin films is unavoidable, most of the 94 DWCNT devices measured show similar electrical retention after diazonium reaction. This suggests DWCNT thin film devices are relatively heterogeneity tolerant and chemically robust, attributes that are essential for high fidelity performance across large numbers of devices. Furthermore, electrical contact between chemically functionalized carbon nanostructures is a recognized critical issue for the use of these types of nanomaterials as conductive, functional electrodes for high performance electrical energy storages and solar energy harvesting[134,135]. The high conductivity retention observed in functionalized DWCNT networks suggests a promising "outer wall" materials strategy to address the electrical contact problem, for example, by self-assembly and spatially controlled functionalization[136] of DWCNT structures.

4 Double Wall Optical Lithography

4.1 Introduction

Nanomaterials possess unique properties on the nanoscale when compared with their bulk counterparts[137]. Many nanomaterials, such as single-walled carbon nanotubes, graphene, silicon nanowires, etc., combine desirable and diverse features that include optical, electrical, and mechanical properties; the unique optical bands and remarkable conductivity/mobility of SWCNTs[138], for instance, have reinvigorated advancements in biotechnology, electronics and optoelectronics[139, 140].

A major challenge of integrating nanomaterials in electronics and optoelectronics applications is to pattern and manipulate nanomaterials with high spatial precision and structural selectivity. For the past decades, photolithography has been commonly used to pattern extremely small features producing increasingly sophisticated integrated circuits. However, there is little success in extending photolithography to nanomaterials because materials compatibility issues arise in the multiple step lithographic processing.

Alternative patterning methods such as direct assembly and guided growth have been proposed to address the pitfalls of photolithography[141,142]. These methods possess distinct advantages, but both methods are still too sophisticated to integrate into real-life applications. Direct assembly while capable of creating dense structure specific patterns, like highly semiconducting yield CNT arrays, it requires the substrate to be pre-patterned[141]. On the other hand, guided growth produces highly aligned, dense

arrays, but utilize substrates that are not conventionally used for semiconductor electronics fabrication therefore need extra transfer steps afterwards[142].

Recently, SWCNTs, and lately, *f*-DWCNTs have proven to be great candidates for high performance semiconductor electronics due to their unparalleled sensitivity derived from a semiconducting SWCNT electrical circuit. As a demonstration of this feature, our group recently demonstrated that *f*-DWCNT TFT can attain ultrahigh simultaneous sensitivity and selectivity by detecting ammonia down to 60 nM with a chemical selectivity over other small molecules by a factor of 6000 [ref. 143]. While promising, the realization of CNT electronics was hindered by two major challenges common to carbon nanotubes: (1) the inability to pattern carbon nanotubes using a simple, scalable, and mostly importantly rapid technique and (2) the heterogeneity of electrical properties stemming from various SWCNT chiralities.

A separate, but also critical challenge for CNT semiconductor electronics are metallic CNT populations, which arise for chiralities where their (n,m) indices fulfill the condition n-m (mod 3) = 0. Metallic CNTs and circuits cannot be turned off because they possess no band gap, making them incapable of gating and operating as a transistor. Purification strategies have been developed to achieve higher semiconductor yields, but there has been yet been a method to produce completely semiconducting CNTs[114]. This challenge is compounded for DWCNTs, which require semiconducting sorting based on their inner wall.

We demonstrate a novel method to pattern arbitrary electronic pathways on an insulating *f*-DWCNT thin film. Optical excitation of a f-DWCNT in a thin film with a laser tuned in resonance with the inner tube selectively removes the functional groups

from the outer tube. By using two different lasers that selectively excited metallic and semiconducting inner tubes, both conducting path and semiconducting channels can be created.

4.2 Materials and Methods:

4.2.1 Materials

DWCNTs: individually suspended by 1 wt.% SDS in nanopure water.

High-purity DWCNTs were separated from a CVD-grown sample (Unidym DW411UA) using DGU, as previously reported[37]. The sorted DWCNTs have an average diameter of 0.86 and 1.61 nm for the inner and outer wall nanotubes, respectively. 1mL of the DWCNT solution was dialysis against 500mL 1wt.% SDS/water solution (freshly changed at 2 hours, 12 hours and 24 hours) for 48 hours. The DWCNT solution then was diluted by 1% SDS/water to a concentration at which the optical absorbance (O.D.) is about 0.2 @ 1000 nm.

SWCNTs: individually suspended by 1 wt.% SDS in nanopure water.

SWCNTs were individually dispersed in an aqueous solution of 2 wt.% SDS by ultrasonication for two hours at 10°C (Misonex, S-4000) followed by ultracentrifugation (170,499g at 20°C for 4 hours) to remove nanotube bundles and metal impurities. One third of the upper solution in the centrifuge tube was collected and diluted with 1wt.% SDS/water. The concentration of SWCNT solution was adjusted so that the absorption base line overlaps with that of DWCNT solution.

Diazonium Salts: 4-nitrobenzenediazonium tetrafluoroborate

4.8 mmol of 4-nitroaniline was added to a round bottom flask (RBF), which was cooled in an ice bath. 9.71 mmol of sodium nitrite (Sigma Aldrich, ≥97.0%) was dissolved in 2 mL of Nanopure^{TM} water and added dropwise to the RBF with stirring. The precipitated 4-nitrobenzenediazonium tetrafluoroborate was washed with 200 mL of cool diethyl ether under vacuum filtration for ~20 minutes while being protected from light. The salts were stored at 4°C and used within a week after synthesis.

Chemicals and other materials:

HiPco SWCNTs, lot. no. 194.3, Rice University

(1) Sodium dodecyl sulfate (SDS): Sigma Aldrich, ≥98.5%

(2) Sodium Nitrite: Sigma Aldrich, ≥97.0%

(3) Tetrafluoroboric acid solution: Sigma Aldrich, 48 wt. % in H_2O

(4) Diethyl ether: Fisher Chemical, anhydrous, BHT-stabilized

(5) 4-niroaniline (Sigma Aldrich, ≥99%)

(6) 4-bromobenzenediazonium tetrafluoroborate: Sigma Aldrich, 96%

(7) Sodium Hydroxide: Sigma Aldrich, 99%

(8) Whatman Anodisc 47 (200nm pore size)

4.2.2 Instruments

Raman Spectroscopy: Raman spectra and Raman map were collected on a Horiba Jobin Yvon Lab RAM Raman microscope (model ARAMIS) using all available excitation lines, 633 nm and 532 nm. In this study, the laser power density is an important parameter which is affected by laser power and focus area. The output of 633 nm and 532 nm laser are 100mW and 10mW. A x100 objective was used in this

study to produce a focus spot with a diameter of approximately 720 nm for the 532 nm laser and 860 nm for the 633nm laser. The spot sizes of the laser were calculated according to the equation $d = 1.22\ \lambda$ /N.A., where λ is the wavelength of the laser and N.A. is the numerical aperture of the lens. Laser power can be tuned by changing the power output. The other condition for taking Raman spectra are listed below: 1 second exposure time, 600 grating and 400nm slit width.

UV-vis-NIR absorption spectroscopy: Absorption spectra were measured using a PerkinElmer Lambda 1050 UV-vis-NIR spectrophotometer equipped with a photomultiplier tube (PMT; σ=2.03% over 48 hours of continuous run) and a broadband InGaAs (σ=1.56% over 48 hours of continuous run) detector. The instrument was warmed up for 15 minutes prior to each use.

Ultrasonicator: MISONIX, model S4000

Bath sonicator: VWR, model B2500A-DTH

Ultracentrifuge: Beckman Coulter Optima LE-80K; 70 Ti rotor

Centrifuge: Beckman Coulter, Microfuge® 16

Nanopure water: Barnstead NANOpure DIamond Life Science (UV/UF) ultrapure water system, Thermo Scientific, Model D11931

4.2.3 Methods

Diazonium Reaction of CNTs:

DWCNTs/SWCNTs solution (15 mL) was kept in a glass vial, to which 70.8 μL of 0.10 M diazonium solution was added to reach a final concentration of ~0.5 mM or ~1 mol equiv of nanotube carbon. The diazonium solution was freshly prepared from 4-nitrobenzenediazonium tetrafluoroborate and water. At reaction time of 24, 48, and 72

hours, one equivalent amounts of diazonium salt were added each time. Exposure to light was limited by covering the vials with aluminum foil.

CNT thin film fabrication:

3 mL of CNT solution (O.D. = 0.2 @ 1000nm) was carefully vacuum filtrated through an AAO membrane. After 60 minutes with vacuum, add 500 mL nanoputer water to wash away surfactant. Carefully load the DWCNT-on-AAO membrane on to a Petri dish containing 40 mL 3M sodium hydroxide solution. After 15 minutes, the AAO membrane dissolved while the CNT film floats on the solution. Transfer the film to fresh water 4 times and finally pick up the film with a clean quartz substrate. Let the film air dry overnight. If the CNT solution is diazonium functionalized, before fabricate films, first dialysis the *f*-CNT solution against 1% SDS/water for 24 hours (freshly changed at 2 hours and 12 hours) to remove excess diazonium reaction byproducts. Because the area of the membrane is fixed, the film thickness can be tuned by the CNT solution volume.

4.2.4 Factors Affecting Laser Writing

4.2.4.1 Laser power density

The 532 nm laser power is gradually increased from 0 to 54 mW by changing the power output (40% to 100%, every 2.5%). At each power take the Raman spectra of *f*-DWCNT in the same spot and record the intensity of outer wall RBM. When the laser power density is lower than a minumim value, the outer wall RBM intensity did not change. When the power density is higher than the minimum value, the outer wall RBM intensity increased almost linearly with the laser power density.

4.2.4.2 *CNT film thickness vs. minimum laser power density*

Six *f*-DWCNT films with different thickness were prepared and Raman spectra were measured with a 0.5 mW/μm^2 laser power density. The G_{in} peak Raman intensity was use as thickness indicating parameter. For each film, the laser power was tuned from 0 to 54 mW to find the minimum laser power density needed to anneal the *f*-DCWNT.

4.2.4.3 *Irradiation time*

When the laser power density is smaller than minimum value that needed for annealing, the *f*-DWCNT will not be annealed by increasing the irradiation time. When the laser power density is right at the minimum value (or slightly higher), the de-functional degree will increase as irradiation time increased, indicated by the rising outer wall RBM intensity.

4.3 Results and Discussions

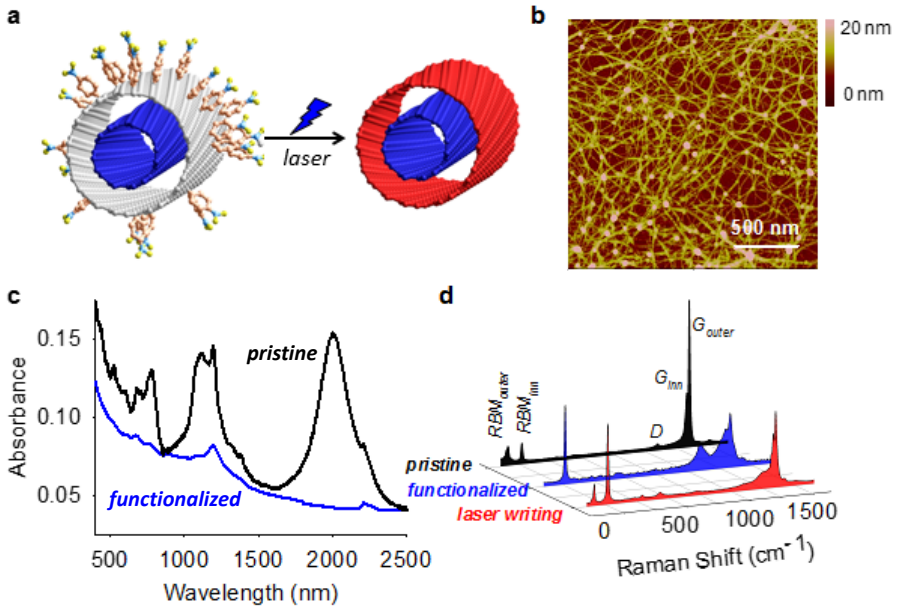

Figure 4-1 Laser writing of *f*-DWCNT networks. (a) Schematic illustration of optical laser annealing of *f*-DWCNT. (b) AFM image of *f*-DWCNT network on quartz substrate (c) Visible-NIR absorption spectra of pristine and functionalized DWCNT films on quartz substrates. (d) Raman spectra showing recovery of pristine, functionalized and laser annealed DWCNTs. Excitation line is 532nm.

The outer walls of DWCNTs were selectively functionalized with C_6H_4Br or $C_6H_4NO_2$ to the exclusion of the inner tube using organic diazonium salts, as we previously reported (Figure 4-2)[144]. Individual *f*-DWCNTs, which is stabilized in water by 1 wt.% sodium dodecyl sulfate (SDS), were vacuum-filtered to make thin films. The visible-NIR absorption spectra of the *f*-DWCNT thin film confirmed intact inner tube features while the outer wall absorbance diminished (Figure 4-1 (c) and Figure 4-2). Raman spectroscopy corroborated this conclusion. A DWCNT is composed of two SWCNTs, each giving rise to a unique set of Raman features, including Radio Breathing Mode (RBM, 100-350 cm-1), tangential mode (G peak, ~1590 cm-1), and disorder mode (D peak, ~1350 cm^{-1})[68]. The DWCNTs used in this study have two sets of RBM at 100-260cm^{-1} and 260-350cm^{-1} that are assigned for inner tubes (d_{inn}~0.86nm) and outer walls (d_{out}~1.61nm), respectively. Upon covalent sidewall functionalization, both the RBM and G peaks of the outer wall diminished; concomitantly arose high D peak due to the sp^3 defects on the outer wall caused by functionalization. Successful removal of the aryl groups from the outer walls by laser annealing are signaled by the recovery of outer wall RBM and G peaks as well as concomitant dropping of the D band intensity (Figure 4-1 (d)).

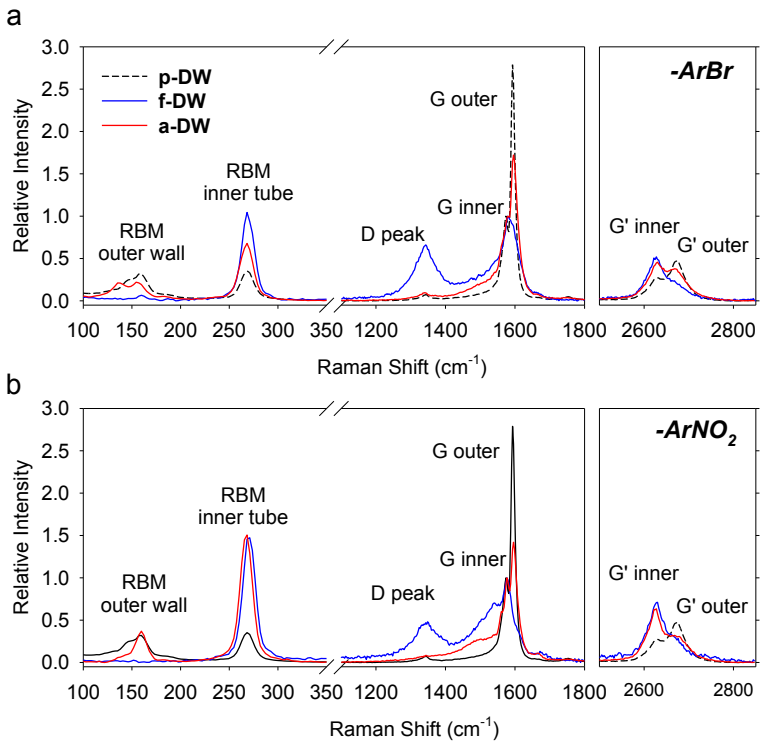

Figure 4-2 *In situ* Raman spectroscopy of (a) C_6H_4Br and (b) $C_6H_4NO_2$ functionalized DWCNT thin films before and after annealing with 532 nm argon ion laser. A laser power density of c.a. 50 mW/μm^2 was used to anneal the sample while the Raman spectra were taken with a power density of 0.5 mW/μm^2.

4.3.1 *Inner tube-selective, double-resonant laser writing*

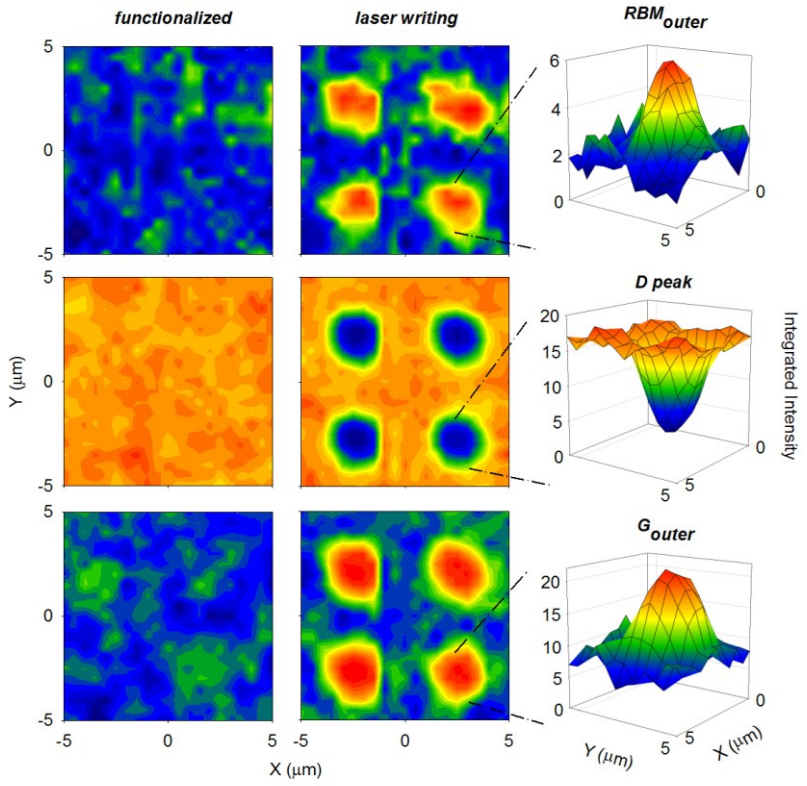

Figure 4-3 Raman mapping of dots arrays. Micro Raman mappings showing the creation of a 2x2 dot array by direct-write laser patterning on a *f*-DWCNT thin film. The laser used was 532nm (50 mW/μm^2) for 1 second per spot. Shown are the integrated Raman intensity of RBM_{inner}, D peak and G_{outer} before and after laser annealing.

This new technique demonstrated the high resolution patterning ability. A 532 nm laser beam with 50 mW/μm^2 power density was used to write a 2x2 array of 2.5 μm dots separated by 5 μm on a *f*-DWCNT thin film (Figure 4-3). Selective removal of functional groups from outer walls is unambiguously confirmed by the recovery of RBM and G peaks of outer wall and diminished D band. The sharp contrast of the dot array written with laser with the rest area on the Raman maps demonstrates the high quality patterning ability of this new technique. The created pattern was read in situ

with MicroRaman mapping using the same laser at a low power density (0.5 $mW/\mu m^2$) to avoid annealing occurring during the spectra reading. Raman spectra were recorded at 0.5 μm steps over a 10μm x 10 μm area.

After diazonium functionalization, all the outer walls were functionalized indiscriminately, as suggested by the completely lost RBM features for both peaks. However, laser annealing selectively recovered part of those covalently functionalized outer walls. This selectivity is highlighted in figure 4-4 where only the outer wall shaded as red color was recovered after laser annealing while the other peaks (shaded grey) remain functionalized. Figure 4-4 compares the Raman spectra of pristine, functionalized and 532 nm laser patterned *f*-DWCNT thin films. In pristine DWCNT samples, the outer wall RBM contains two features, 147 cm^{-1} and 160 cm^{-1}, from two different outer walls that can be simultaneously excited by the 532 nm laser. In the inner tube region, there is only one peak at 269 cm^{-1}, suggesting that only one electronic type inner tube is in resonance with 532nm laser excitation. Based on Kataura plot the grey and red color outer walls can be assigned to (21,1) and (13,9), respectively; the inner tube can be assigned to (9,3). After laser annealing only the RBM of (13,9) was recovered.

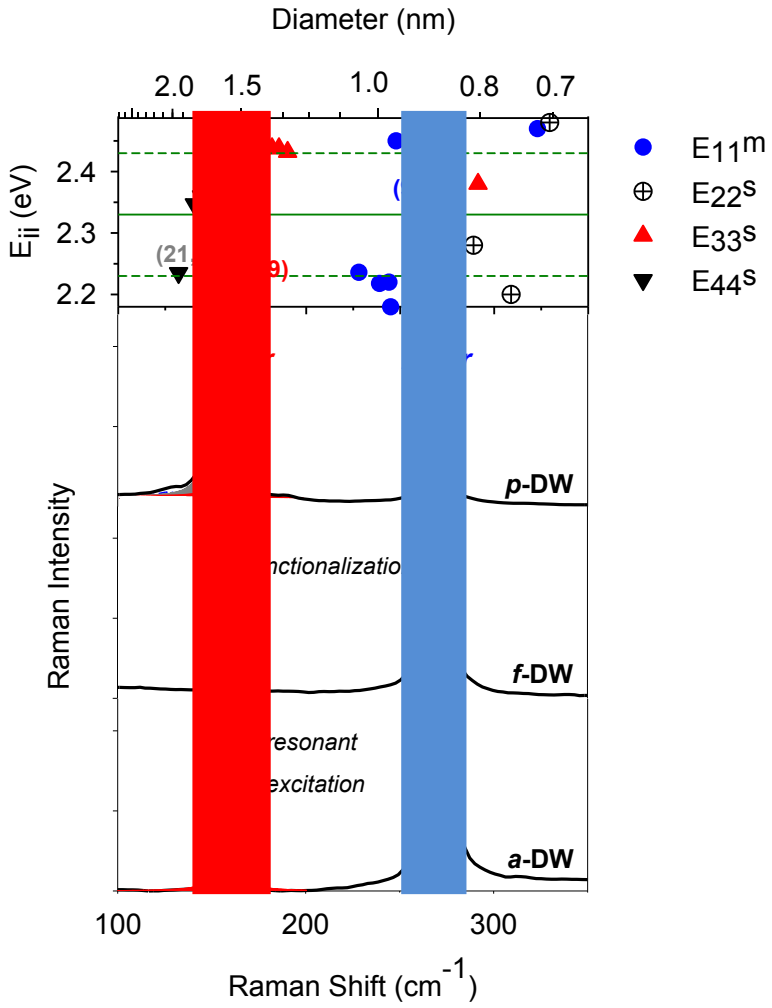

Figure 4-4 Inner tube-selective, double-resonant laser writing. Shown are the RBMs of pristine, functionalized and laser written DWCNTs, respectively. The peak in the outer wall BRM region is de-convoluted by peak fitting with Lorentzian shape into two peaks and are assigned to (21,1) and (13,9). The peaks are shaded as red and grey color for clarity. A Kataura plot in the resonant window of 532 nm excitation was also shown on the top. The inner tube at 160 cm^{-1} can be assigned to (9,3).

We attributed the selective recovery of outer wall RBM to the simultaneous-resonance enhancement of inner tube and outer wall vibrations upon the incident laser. A laser most efficiently excites the nanotubes with electronic transitions that match the

incident laser energy. That means in a DWCNT, the incident laser may only excite one of the nanotube components, or in some cases both inner tube and outer wall. In our experiment, the (9,3) and (13,9) should be the inner tube and outer wall of the same DWCNT, because the vibration of (9,3) is strongly coupled to that of (13,9). This observation was consistent with single nanotube Raman spectroscopy studies by Dresselhaus and co-workers, which identify (18,6)@(12,9) as a DWCNT with both outer wall and inner tube simultaneously in resonance with the same excitation line laser[115]. In our study, the peak positions of the outer wall and inner tube were 160 cm^{-1} (vs. 158 cm^{-1}) and 269 (vs. 265 cm^{-1}), which, according to Kataura plot, can be assigned to (9,3)@(13,9).

The inner tube at 269 cm^{-1} and outer wall at 160 cm^{-1} showed correlated features when excited by 532 nm laser (Figure 4-5). Continuous 40 seconds of irradiation caused the inner tube (9,3) and the (13,9) outer wall intensity increased synchronously. This observation confirms the simultaneous-resonance occurred in the (9,3)@(13,9) structure; *i.e.*, (9,3) and (13,9) are the outer wall and inner tube of the same DWCNT. For those outer walls encapsulating inner tubes that are not in resonance with 532 nm laser (grey shade in Figure 4-4), their RBM features were not recovered due to absence of the simultaneous-resonance condition.

When the 632.8 nm output of a $HeNe^{+}$ laser was used as the excitation line, similar simultaneous-resonance phenomenon was observed (Figure 4-5). In this case, two inner tube peaks, at 257 and 280 cm^{-1}, were observed in the pristine DWCNTs (Figure 4-5). According to Kataura plot, these two peaks can be signed to (10, 3) and

(7, 5). After annealing using the 632.8 nm laser, the RBM intensity of (7, 5) did not change at all while the (10,3) intensity increased along with appearance of the outer wall RBM peak at 156 cm^{-1} which was signed to either (19,6) or (20, 0). During the 55 seconds of laser irradiation, the RBM intensities of (10,3) and (19,6)/(20, 10) were correlated and grew in the same pace, strongly suggesting that in (10,3)@(19,6)/(20,0) DWCNT configuration both inner tube and outer wall were in resonance with 632.8 nm laser excitation and this simultaneous-resonance enhanced both outer wall and inner tube RBM signals. In contrast, the other inner tube (7,5) can also be excited by the 632.8 nm laser, without an outer wall that can be simultaneously excited by the same laser, intensity of (7,5) did not increased.

We observed increased relative RBM intensity of inner tube after functionalization. One of the possible reasons is that functionalization causes a considerable amount of the sp^2 lattice of the outer walls turned into sp^3 which are pyramid shape pointing outside of the tube axis. This enlarges outer wall leaving more room for the inner tube to vibrate. The outer wall functionalization also reduces the electronic coupling between the two walls, which may free the inner tube to some extent. After laser writing, the intensity of inner tube did not drop to the pristine level. Besides one obvious reason that the annealing process is not completely reversible, there are two other possibilities: 1) Only the outer walls containing the inner tubes that are resonant with the laser are effectively annealed. The rest of the outer walls which remain functionalized provide more room for inner tube vibration resulting in relatively high inner tube RBM. 2) In the annealing process simultaneous-resonance between inner tube and outer wall enhances the RBM signal.

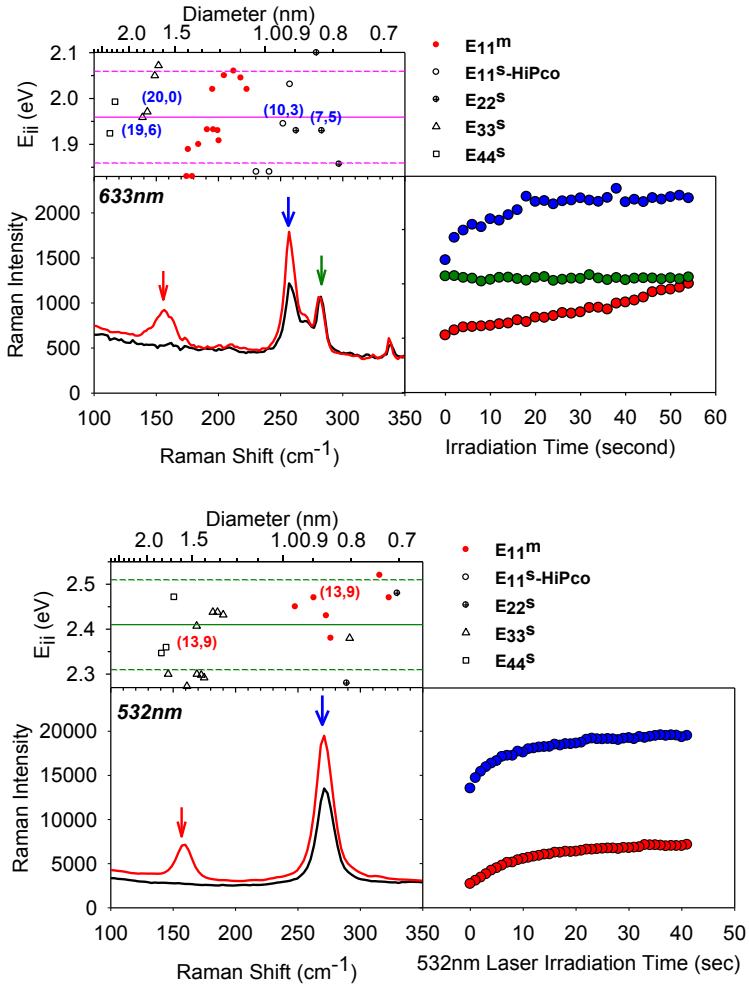

Figure 4-5 Inner-tube and outer wall correlation revealed by double-resonant Raman spectroscopy. Intensity of the two peaks marked by red and blue star increased as increasing 532nm/633nm laser irradiation time. The inner peak indicated by black star didn't show intensity change upon 633nm excitation.

Is it possible to control the semiconducting or metallic nature of the patterned pathway by tuning the writing laser to the resonance of the inner tube? To explore this concept, we exploited two laser lines, 532nm and 632.8 nm, in the experiments for writing and *in situ* reading by Raman spectroscopy. As shown in Figure 4-9 (b), we were able to selectively create semiconducting inner tube @ semiconducting outer wall

(S@S) and metallic inner tube @ semiconducting outer wall (M@S) patterns with 532nm and 633nm excitation lines, respectively. The inner tubes that are in resonance with 632.8 nm laser were excited by the laser, effectively restoring the outer wall as suggested by the same 632.8 nm reading laser. Those inner tubes beyond the resonance window of the 632.8nm laser didn't show the associated recovered outer wall feature in the spectrum. One may question whether the 532nm laser (or 633nm) can detect the outer walls annealed by inner tube that is in resonance with 633nm (or 532nm) laser. Although it cannot be completely ruled out, this possibility is small since there are only 20 configurations for CVD grown DWCNTs[145] and the DWCNT used in this study was further purified with DGU to afford only the nanotubes with similar density.

4.3.2 Laser annealing conditions

The inner tube selectivity was better achieved by controlling several coupled parameters. Firstly, there is a threshold power density of the laser, below which annealing does not occur no matter how long it takes (Figure 4-6). As a result, the Raman spectra did not change and the outer wall features were not recovered. This threshold feature ensures correct in situ reading with Raman spectroscopy of the patterned structures under the low power limit. The existence of threshold energy can be partially understood by balancing laser heating with heat dissipation. The CNT films convert photons to heat while the substrate beneath is a heat sink. The sharp transition in Figure 4-6 (a) is probably the point when the absorbed energy is balanced by heat dissipation. The energy at this point is the minimum power density needed to locally anneal the *f*-DWCNTs. Secondly, when the laser power density is higher than the

threshold energy, resonant excitation of the inner tubes anneal the outer wall and the annealing degree increases as a function of irradiation time (Figure 4-6 (a)). Finally, the DWCNT density in the network greatly affects the minimum power density needed (Figure 4-7). The relative areal density of *f*-DWCNTs in the thin films can be conveniently monitored using the intensity of the Raman G peak of *f*-DWCNTs. The higher G peak indicates higher nanotube density[146]. We plotted Raman intensity vs minimum power density needed to anneal the outer wall (Figure 4-7). We found that the higher nanotube density, as suggested by a higher Raman G-peak intensity, the lower threshold power density was needed to effect laser writing on the *f*-DWCNT thin films. This thickness dependence can be understood by thermal crosstalk at increasing tube density.

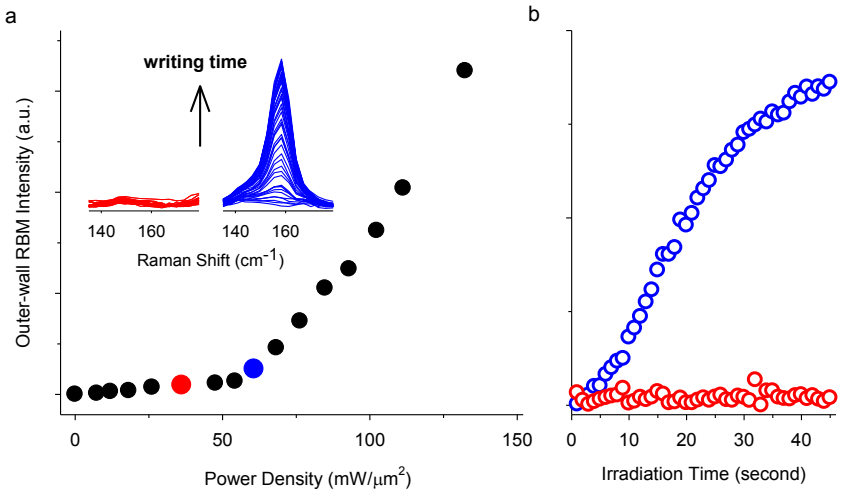

Figure 4-6 Critical power density. (a) Power density vs outer wall RBM intensity clearly shown existence of threshold power density for laser patterning of *f*-DWCNT thin films. The inset plot shows Raman spectral evolution of the RBM of outer walls as a function of laser irradiation time at the threshold power density (blue), and at a power density right below the threshold energy (red). (b) The RBM intensity of the inset plots in (a) vs irradiation time.

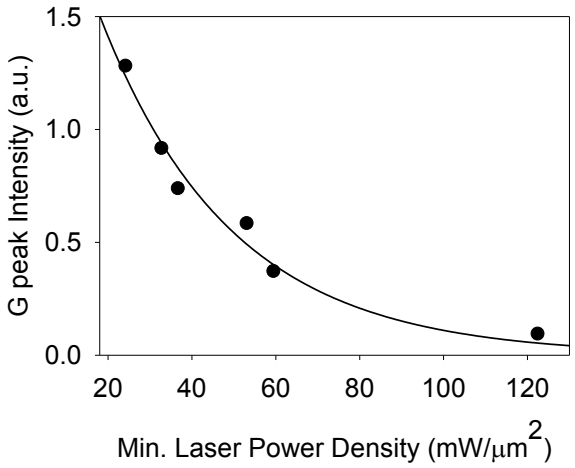

Figure 4-7 The minimum power density of laser required for patterning an *f*-DWCNT film of varying thickness, which is approximately proportional to the Raman intensity of the G-peak, measured using laser intensity well below the threshold energy.

Lastly, one more experiment was conducted to explicitly prove the inner tube was the essential part in the annealing process. To minimize the tube density differentiation, we started with *f*-DWCNT and *f*-SWCNT thin films with the similar functional degree and Raman G peak intensity. When irradiated by the 532 nm laser under the same condition, the *f*-DWCNT showed recovered outer wall while *f*-SWCNT RBM was still flat (Figure 4-8). The distinct difference was due to the presence of inner tubes in DWCNTs; without such energy absorbance source, the *f*-SWCNT cannot be effectively annealed. Keeping in mind the three factors that affecting annealing process, the experiment condition need to be well controlled at minimum power density and short irradiation time. We note that annealing of *f*-SWCNTs also occurred at high power density but little resonance effects were observed since the sidewall chemical

functionalization partially or completely destroys the characteristic nanotube optical absorption.

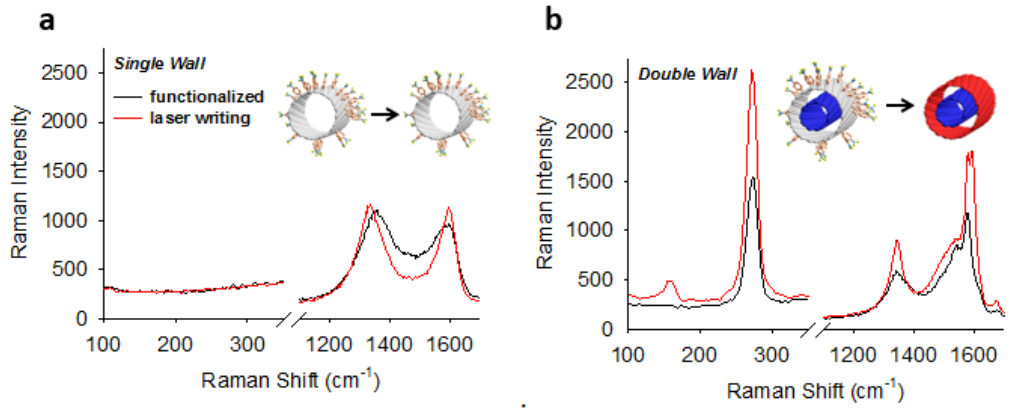

Figure 4-8 Raman spectra of *f*-DWCNT(a) and *f*-SWCNT(b) before and after patterning with 532nm laser at the same condition. Molecular models show how the tubes behave differently upon laser writing.

4.3.3 Electrical conductivity of laser patterned DWCNT channels.

To test the device properties, lines were patterned between electrodes on a *f*-DWCNT film. Laser writing generated a conducting pathway on the insulating *f*-DWCNT. Figure 4-9 (a) is a schematic illustration of the laser writing process. The *f*-DWCNT film was originally insulating with only 0.4 μA current (at an applied voltage of 1 V) between two electrodes separated 50 μm. That is because functionalized outer walls blocked the electronic interference among inner tubes. Upon laser annealing, the inner tubes accumulate the energy on the laser writing route and recover the outer walls therefore regenerate the conductivity between neighboring tubes. With a 17 μm channel created by laser writing, the conductivity increased to 87 μA, which is a 217 time

increase. If the width of electrodes is taken into consideration, which is 200 μm, the enhancement is even more significant. Furthermore, the conductivity increased linearly with the line width.

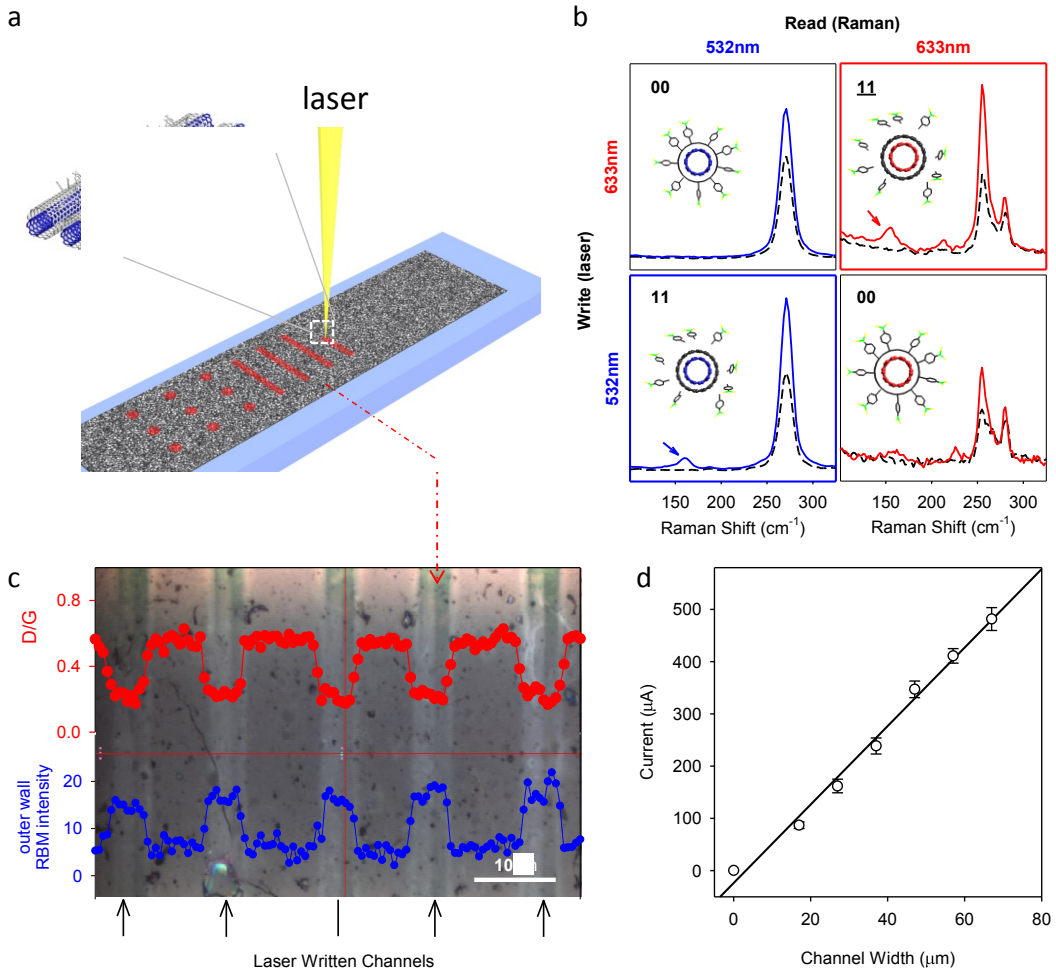

Figure 4-9 Electrical conductivity of laser patterned DWCNT channels. (a) schematic illustration of optical patterning on a *f*-DWCNT; the inset is the enlarged scheme showing the inner tube – annealed outer wall conducting pathway. (b) Optically selective encoding of *f*-DWCNTs. The f-DWCNT thin film was patterned with one laser and read with Raman spectroscopy. Two laser lines, 532 nm and 633 nm, one of which was in resonance with the inner tube, were used for the writing and reading, leading to four structure combinations. In the Raman spectra, *f*-DWCNTs were shown

in dashed lines and (f)-DWCNTs after laser annealing were shown in solid lines. The molecular models shown are the simplest scenario with only two tubes. (c) The patterned films reveal periodic intensity profiles of outer wall RBM and Raman D/G ratio. Shown is a parallel array of 7 μm wide channels, as indicated by the arrows. (d) Electrical conductivity vs. channel width of patterned DWCNT channels on an insulating *f*-DWCNT thin film.

4.4 Conclusion

We demonstrate optical recovery of *f*-DWCNTs using lasers tuned to resonant with the inner tubes. This phenomenon is exploited as the basis of a new lithography technique that allows one to create arbitrary conducting patterns on a *f*-DWCNTs thin film with high resolution and efficiency. When the excitation laser energy matches the excitonic transition energy of the inner tubes, simultaneous-resonance enhances the coupling of the inner tube vibration with laser, allowing the functional groups thermally detached from the outer wall. This double resonant excitation of the inner tube selectively recovers the outer wall. This work opens a route to carbon nanotube lithography and may greatly facilitate the application of carbon based electronic devices in biology techniques as well as other fields that desire both material compatibility with environment and carbon nanotube electronic properties.

5 Summary and Outlook

In summary, this thesis demonstrates two novel covalent chemical strategies that overcome fundamental challenges of CNT functionalization.

First, enhancement of CNT photoluminescence was achieved by controlled sidewall functionalization with aryl groups. The substantial brightening in PL is contributed to chemical creation of a new, defect induced and optically-allowed state that lies below the predicted energy levels of dark excitons. Both the emission energy and the maximum PL brightening are chemically tunable by changing electron withdrawing/donating substituents on the aryl functional group. This work also demonstrated the important role of defects in low dimensional materials[147].

Second, diazonium chemistry was successfully exploited to create outer wall-selectively functionalized double-walled carbon nanotubes ~~(*f*-DWCNTs)~~. At the saturation limit of diazonium functionalization, a SWCNT network becomes electrically insulating; in stark contrast, the *f*-DWCNT retains 50% of the initial conductivity, owing to the intact inner tube pathway.

Based on the *f*-DWCNT network, a laser patterning technique was developed. The structure and properties of functionalized outer wall were selectively restored by resonant excitation of the inner tube with laser. Conventional lithography typically involves multiple steps; in contrast, this new technique completes the patterning in only one step by direct writing with a laser beam.

These observations open new opportunities to address further questions of fundamental and technological importance. Below I will discuss several examples.

What is the upper limit of the quantum yield of a SWCNT? The intrinsically low QY of carbon nanotubes are due to the existence of dark states. In chapter 2, we demonstrated the creation of an optically allowed defect state lying lower in energy than dark state, thereby harnessing excitons and enhancing the quantum yield by up to 28 times. The quantum yield achieved was ~16%. We also discussed the relationship of the brightening factor with respect to electron withdrawing ability of the terminating groups in the benzene ring: the more electron withdrawing ability, the higher the enhancement factor. The most electron withdrawing group we tested is 3,5-dinitrobenzene. By using a trinitrobenzene group, one would expect even higher QY. But in order to use the trinitrobenzene group, two obstacles need to be considered: steric hindrance of the aryl compound itself and steric hindrance of trinitrobenzne with SWCNT. Little literature is found on 3,4,5-trinitrobenzene mostly due to the steric hindrance between neighboring nitro groups on the ring. 2,4,6-trinitrobenzene is available, however, the nitro groups on the meta position is simply too crowded for the reaction to occur. As discussed in chapter 1, the exact mechanism of diazonium reaction with the SWCNT is not completely understood. Ricci *et al.* suggested that this reaction will result in two different covalent bonds as seen in scheme 5-1: the benzene ring will attach to the SWCNT side wall through C-C or C-N=N-C bond[148]. In the case of the latter, the steric hindrance of the aryl group and SWCNT is minimal. Moreover because the N=N bond added electron withdrawing effects onto the aryl group, even higher enhancement or more red-shift may be achieved.

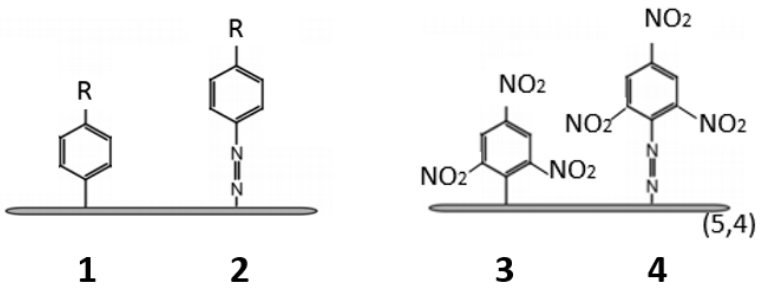

Scheme 5-1 Two possible covalent bonds between the aryl groups and SWCNTs (1, 2). Specifically two possibilities of covalent bonds that can be formed via trinitrobenzene diazonium reaction with (5,4) are shown in 3 and 4.

SWCNT is one of very few fluorophores that emit within the second near-IR region (1000-1400 nm)[18,149,150]. The second NIR emission is particularly interesting for bio-imaging applications because of little background in bio-tissue at this energy. However, due to the limited amount of second NIR fluorophores and biocompatibility of the fluorophores, so far only SWCNTs and very few quantum dots are available for such use. The new *f*-SWCNTs with red-shifted and enhanced emission features, is an excellent candidate for this imaging application.

Fluorescence from inner tubes in outer wall functionalized *f*-DWCNTs has been widely studied[122,151]. In chapter 3, it was shown that inner tube optical properties can be resolved clearly with Raman and absorption spectra for diazonium functionalized DWCNT with 6% of carbons on the outer wall converted to sp^3 bonds. This leads one to ask whether we can electronically decouple the inter-tube interaction in DWCNT and resolve the inner tube fluorescence. To achieve this goal, the functional degree on the outer walls has to be further increased. Theoretically, one could expect the functional degree from diazonium chemistry to be beyond 6.9%. The reason why this

number stops growing is believed to be due to polymerization of the diazonium compounds. More specifically, aryl radicals generated in diazonium chemistry tend to react with the carbon nanotubes as well as the aryl groups that are already covalently bonded to the carbon nanotubes[152]. This polymerization will result in a huge functional group on the tube surface shadowing the neighboring sp^2 carbon atoms from further reaction. To avoid this problem, an aryl group with the 3,4,5-position occupied is an ideal candidate since polymerization is hindered.

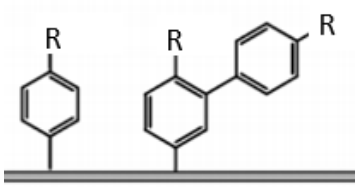

Scheme 5-2 Possibility of polymerization from diazonium reaction is shown in the right structure.

f-DWCNT with inner tube and outer wall completely decoupled is expected to be a revolutionary type of nanomaterial. Scientifically, this would be a perfect structure to study the electronic properties of free standing one dimensional nanomaterials. From an application point of view, this would be a solution for solving the functionality vs. property issue that is unavoidable in SWCNTs.

Beyond the scope of this thesis, carbon nanotube is of interest in many other fields, like electronics, display and energy[11]. The first carbon nanotube computer has recently been reported, with performance comparable to the first Intel 4004 chip; it may be the first step towards moving beyond silicon electronics[153]. Additionally, high-quality SWCNT transistors on flexible plastic are used to create flexible and low-power displays for a variety of applications in smartphones and TVs[154]. Beaded electrodes

made from the incorporation of CNTs with silicon improved durability by at least 20 times compared to that of silicon electrode [23].

Many novel nanomaterials have been synthesized over the last two decades. However, the unique structure and amazing properties of carbon nanotube continue to fuel innovation. This thesis illustrates some unexpected observations from my research in the Wang group at the University of Maryland. We hope this work will help take carbon nanoscience in new directions.

References

1. O'Connell, M. J. *et al.* Band gap fluorescence from individual single-walled carbon nanotubes. *Science.* **297,** 593–596 (2002).

2. Krishnan, a., Dujardin, E., Ebbesen, T., Yianilos, P. & Treacy, M. Young's modulus of single-walled nanotubes. *Phys. Rev. B* **58,** 14013–14019 (1998).

3. Treacy, M. M., Ebbesen, T. W. & Gibson, J. M. Exceptionally high Young's modulus observed for individual carbon nanotubes. *Nature* **381,** 678–680 (1996).

4. Dürkop, T., Getty, S. a., Cobas, E. & Fuhrer, M. S. Extraordinary mobility in semiconducting carbon nanotubes. *Nano Lett.* **4,** 35–39 (2004).

5. Han, Z. & Fina, A. Thermal conductivity of carbon nanotubes and their polymer nanocomposites: A review. *Prog. Polym. Sci.* **36,** 914–944 (2011).

6. J. Hone, Carbon nanotubes: thermal properties, *In Dekker Encyclopedia of Nanoscience and Nanotechnology*, 603-610, New York: Marcel Dekker, Inc. (2004)

7. Frank, B., Rinaldi, A., Blume, R., Schlögl, R. & Su, D. S. Oxidation stability of multiwalled carbon nanotubes for catalytic applications. *Chem. Mater.* **22,** 4462–4470 (2010).

8. Deng, C., Zhang, X., Wang, D. Chemical stability of carbon nanotubes in the 2024Al matrix. *Mater. Lett.* **61**, 904–907 (2007).

9. Iijima, Sumio; Ichihashi, T. Single shell carbon nanotubes of 1-nm diameter. *Nature* **363**, 603 (1993).

10. Benthune, D. S. *et al.* Colbalt-catalysed grouth of carbon nanotubes with single-atomic-layer walls. *Nature* **363**, 605–607 (1993).

11. Volder, M. F. L. De, Tawfick, S. H., Baughman, R. H. & Hart, A. J. Carbon nanotubes: present and future commercial applications. *Science* **339**, 535–539 (2013).

12. Franklin, A. D. *et al.* Sub-10 nm carbon nanotube transistor. *Nano Lett.* **12**, 758–762 (2012).

13. Chen, Z. *et al.* An integrated logic circuit assembled on a single carbon nanotube. *Science* **311**, 1735 (2006).

14. Henzie, J., Barton, J. E., Stender, C. L. & Odom, T. W. Large-area nanoscale patterning: chemistry meets fabrication. *Acc. Chem. Res.* **39**, 249–257 (2006).

15. Nanot, S., Hároz, E. H., Kim, J.-H., Hauge, R. H. & Kono, J. Optoelectronic properties of single-wall carbon nanotubes. *Adv. Mater.* **24**, 4977–4994 (2012).

16. Hu, C., Liu, C., Chen, L., Meng, C. & Fan, S. A Demo opto-electronic power source based on single-walled carbon nanotube sheets. *ACS Nano* **4**, 4701–4706 (2010).

17. Laiho, P., Susi, T., Kaskela, A., Nasibulin, A. G. & Kauppinen, E. I. Optoelectronic performance of nitrogen-doped single-walled carbon nanotube films. *J. Nanoelectron. Optoelectron.* **7**, 68–72 (2012).

18. Hong, G. *et al.* Multifunctional in vivo vascular imaging using near-infrared II fluorescence. *Nat. Med.* **18**, 1841–1846 (2012).

19. Sun, X., Sun, H., Li, H. & Peng, H. Developing polymer composite materials: carbon nanotubes or graphene? *Adv. Mater.* **25**, 5153–5176 (2013).

20. Andrews, R. & Weisenberger, M. . Carbon nanotube polymer composites. *Solid State Mater. Sci.* **8**, 31–37 (2004).

21. Wong, S. S. *et al.* Single-walled carbon nanotube probes for high-resolution nanostructure imaging. *Appl. Phys. Lett.* **73**, 3465–3467 (1998).

22. Kumar, S. *et al.* Atomic force microscope manipulation of multiwalled and single walled carbon nanotubes with reflux and ultrasonic treatments. *Appl. Nanosci.* ***4***, 19-26 (2012).

23. Sun, C. *et al.* A beaded-string silicon anode. *ACS Nano* **7**, 2717–2724 (2013).

24. Assfour, B., Leoni, S., Seifert, G. & Baburin, I. A. Packings of carbon nanotubes--new materials for hydrogen storage. *Adv. Mater.* **23**, 1237–1241 (2011).

25. Tu, X., Manohar, S., Jagota, A. & Zheng, M. DNA sequence motifs for structure-specific recognition and separation of carbon nanotubes. *Nature* **460**, 250–253 (2009).

26. Liu, H., Nishide, D., Tanaka, T. & Kataura, H. Large-scale single-chirality separation of single-wall carbon nanotubes by simple gel chromatography. *Nat. Commun.* **2**, 1–7 (2011).

27. Arnold, M. S., Green, A. a, Hulvat, J. F., Stupp, S. I. & Hersam, M. C. Sorting carbon nanotubes by electronic structure using density differentiation. *Nat. Nanotechnol.* **1**, 60–65 (2006).

28. Carlson, L. J., Maccagnano, S. E., Zheng, M., Silcox, J. & Krauss, T. D. Fluorescence efficiency of individual carbon nanotubes. *Nano Lett.* **7**, 3698–3703 (2007).

29. Ju, S., Kopcha, W. P. & Papadimitrakopoulos, F. Brightly fluorescent single-walled carbon nanotubes via an oxygen- excluding surfactant organization. *Science.* **323**, 1319–1323 (2009).

30. Goldsmith, B. R. *et al.* Conductance-controlled point functionalization of single-walled carbon nanotubes. *Science* **315**, 77–81 (2007).

31. Monthioux, M. & Kuznetsov, V. L. Who should be given the credit for the discovery of carbon nanotubes? *Carbon* **44**, 1621–1623 (2006).

32. Radushkevich, L. V., Lukyanovich, V. M. & Ugleroda, O. strukture. obrazujucegosja pri termiceskom razlozenii okisi ugleroda na zeleznom kontakte. *Zurn Fis. Chim* **26**, 88–95 (1952).

33. Iijima, S. Helical microtubules of graphitic carbon. *Nature* **354**, 56–58 (1991).

34. Palser, A. Interlayer interactions in graphite and carbon nanotubes. *Phys. Chem. Chem. Phys.* 4459–4464 (1999).

35. Ge, M. & Sattler, K. Vapor-Condensation Generation and STM Analysis of Fullerene Tubes. *Science* **260**, 515–518 (1993).

36. Shen, C., Brozena, A. H. & Wang, Y. Double-walled carbon nanotubes: Challenges and opportunities. *Nanoscale* **3**, 503–518 (2010).

37. Green, A. A. & Hersam, M. C. Processing and properties of highly enriched double-wall carbon nanotubes. *Nat. Nanotechnol.* **4**, 64–70 (2009).

38. Jamada, N., Sawada, S. & Oshiyama, A. New one-dimendioanl conductors: Graphitic microtubules. *Phys. Rev. Lett.* **68**, 1597–1581 (1992).

39. Bachilo, S. M. *et al.* Structure-assigned optical spectra of single-walled carbon nanotubes. *Science.* **298**, 2361–2366 (2002).

40. Dresselhaus, M. S., Dresselhaus, G., Saito, R. & Jorio, A. Exciton photophysics of carbon nanotubes. *Annu. Rev. Phys. Chem.* **58**, 719–747 (2007).

41. Hofmann, M. S. *et al.* Bright, long-lived and coherent excitons in carbon nanotube quantum dots. *Nat. Nanotechnol.* **8**, 502–505 (2013).

42. Wang, F., Dukovic, G., Brus, L. E. & Heinz, T. F. The optical resonances in carbon nanotubes arise from excitons. *Science.* **308**, 838–841 (2005).

43. Chang, E., Bussi, G., Ruini, A. & Molinari, E. Excitons in carbon nanotubes: an ab initio symmetry-based approach. *Phys. Rev. Lett.* **92**, 196401 (2004).

44. Kane, C. & Mele, E. Ratio Problem in single carbon nanotube fluorescence spectroscopy. *Phys. Rev. Lett.* **90**, 207401 (2003).

45. Hafner, J. H. *et al.* Catalytic growth of single-wall carbon nanotubes from metal particles. *Chem. Phys. Lett.* **296**, 195–202 (1998).

46. Nikolaev, P. *et al.* Gas-phase catalytic growth of single-walled carbon nanotubes from carbon monoxide. *Chem. Phys. Lett.* 91–97 (1999).

47. Bronikowski, M. J., Willis, P. a., Colbert, D. T., Smith, K. a. & Smalley, R. E. Gas-phase production of carbon single-walled nanotubes from carbon monoxide via the HiPco process: A parametric study. *J. Vac. Sci. Technol. A Vacuum, Surfaces, Film.* **19**, 1800–1805 (2001).

48. Kitiyanan, B., Alvarez, W. E., Harwell, J. H. & Resasco, D. E. Controlled production of single-wall carbon nanotubes by catalytic decomposition of CO on bimetallic Co – Mo catalysts. *Chem. Phys. Lett.* **317**, 497–503 (2000).

49. Journet, C. *et al.* Large-scale production of single-walled carbon nanotubes by the electric-arc technique. *Nature* **388**, 756–758 (1997).

50. Thess, A. *et al.* Crystalline ropes of metallic carbon nanotubes. *Science.* **273**, 483–487 (1996).

51. Kitiyanan, B., Alvarez, W. E., Harwell, J. H. & Resasco, D. E. Controlled production of single-wall carbon nanotubes by catalytic decomposition of CO on bimetallic Co – Mo catalysts. **317**, *Chem. Phys. Lett.* 497–503 (2000).

52. Bachilo, S. M. *et al.* Narrow (n,m)-distribution of single-walled carbon nanotubes grown using a solid supported catalyst. *J. Am. Chem. Soc.* **125**, 11186–111877 (2003).

53. Samsonidze, G. G. *et al.* The concept of cutting lines in carbon nanotube science. *J. Nanosci. Nanotechnol.* **3**, 431–458 (2003).

54. Fathi, D. A Review of electronic band structure of graphene and carbon nanotubes using tight binding. *J. Nanotechnol.* **2011**, 1–6 (2011).

55. Ando, T. The electronic properties of graphene and carbon nanotubes. *NPG Asia Mater.* **1**, 17–21 (2009).

56. Castro Neto, a. H., Peres, N. M. R., Novoselov, K. S. & Geim, a. K. The electronic properties of graphene. *Rev. Mod. Phys.* **81**, 109–162 (2009).

57. Nagatsu, K., Chiashi, S., Konabe, S. & Homma, Y. Brightening of triplet dark excitons by atomich hydrogen adsorption in single-walled carbon nanotubes observed by photoluminescence spectroscopy. *Phys. Rev. Lett.* **105**, 157403 (2010).

58. Katsnelson, M. I. Graphene : carbon in two dimensions. *Mater. Today* **10**, 20–27 (2007).

59. Chen, Y. *et al.* Helicity-dependent single-walled carbon nanotube alignment on graphite for helical angle and handedness recognition. *Nat. Commun.* **4**, 2205 (2013).

60. Leeds, J. D., Fourkas, J. T. & Wang, Y. Achieving ultrahigh concentrations of fluorescent single-walled carbon nanotubes using small-molecule viscosity modifiers. *Small* **9**, 241–247 (2013).

61. Oh, H., Sim, J. & Ju, S.-Y. Binding affinities and thermodynamics of noncovalent functionalization of carbon nanotubes with surfactants. *Langmuir* **29**, 11154–11162 (2013).

62. Moore, V. C. *et al.* Individually Suspended Single-Walled Carbon Nanotubes in Various Surfactants. *Nano Lett.* **3**, 1379–1382 (2003).

63. Yurekli, K., Mitchell, C. a & Krishnamoorti, R. Small-angle neutron scattering from surfactant-assisted aqueous dispersions of carbon nanotubes. *J. Am. Chem. Soc.* **126**, 9902–9903 (2004).

64. Usrey, M. L., Lippmann, E. S. & Strano, M. S. Evidence for a two-step mechanism in electronically selective single-walled carbon nanotube reactions. *J. Am. Chem. Soc.* **127**, 16129–16135 (2005).

65. Clark, M. D., Subramanian, S. & Krishnamoorti, R. Understanding surfactant aided aqueous dispersion of multi-walled carbon nanotubes. *J. Colloid Interface Sci.* **354**, 144–51 (2011).

66. Imura, Y., Morita, C. & Kawai, T. Reversible dispersion–precipitation of single-walled carbon nanotubes by pH change and addition of organic components. *New J. Chem.* **37**, 3607 (2013).

67. Yang, B. *et al.* The characterization of the concentration of the single-walled carbon nanotubes in aqueous dispersion by UV-Vis-NIR absorption spectroscopy. *Analyst* **138**, 6671–6 (2013).

68. Dresselhaus, M. S., Dresselhaus, G., Saito, R. & Jorio, a. Raman spectroscopy of carbon nanotubes. *Phys. Rep.* **409**, 47–99 (2005).

69. Pimenta, M. *et al.* Raman modes of metallic carbon nanotubes. *Phys. Rev. B* **58**, R16016–R16019 (1998).

70. Dresselhaus, M. Quantum Transport and Dynamics in Nanostructures. in *4th Wind. Summer Sch. Condens. Matter Theory* (2007).

71. Kataura, H. *et al.* Optical properties of single-wall carbon nanotubes. *Synth. Met.* **103**, 2555–2558 (1999).

72. Kataura-Plot for Resonant Raman. Online information available at *http://www.photon.t.u-tokyo.ac.jp/~maruyama/kataura/kataura.html* (accessed Nov. 2013)

73. Zhou, G., Duan, W. & Gu, B. First-principles study on morphology and mechanical properties of single-walled carbon nanotube. *Chem. Phys. Lett.* **333**, 344–349 (2001).

74. Tan, P. *et al.* Photoluminescence Spectroscopy of Carbon Nanotube Bundles: Evidence for Exciton Energy Transfer. *Phys. Rev. Lett.* **99**, 137402 (2007).

75. Niyogi, S. *et al.* Chemistry of single-walled carbon nanotubes. *Acc. Chem. Res.* **35**, 1105–1113 (2002).

76. Strano, M. S. *et al.* Electronic structure control of single-walled carbon nanotube functionalization. *Science* **301**, 1519–1522 (2003).

77. Allongue, P. *et al.* Covalent modification of carbon surfaces by aryl radicals generated from the electrochemical reduction of diazonium salts. *J. Am. Chem. Soc.* **7863**, 201–207 (1997).

78. Picot, M., Lapinsonnière, L., Rothballer, M. & Barrière, F. Graphite anode surface modification with controlled reduction of specific aryl diazonium salts for improved microbial fuel cells power output. *Biosens. Bioelectron.* **28**, 181–188 (2011).

79. Busson, M., Berisha, A., Combellas, C., Kanoufi, F. & Pinson, J. Photochemical grafting of diazonium salts on metals. *Chem. Commun.* **47**, 12631–12633 (2011).

80. Flavin, K., Chaur, M. N., Echegoyen, L. & Giordani, S. Functionalization of multilayer fullerenes (carbon nano-onions) using diazonium compounds and "click" chemistry. *Org. Lett.* **12**, 840–843 (2010).

81. Christopher, D., Dyke, A., Stewart, M. P., Maya, F. & Tour, J. M. Diazonium-based functionalization of carbon nanotubes : XPS and GC – MS analysis and mechanistic implications. *SynLett* 155–160 (2004).

82. Doyle, C. D., Rocha, J.-D. R., Weisman, R. B. & Tour, J. M. Structure-dependent reactivity of semiconducting single-walled carbon nanotubes with benzenediazonium salts. *J. Am. Chem. Soc.* **130**, 6795–800 (2008).

83. Kuzmany, H. Functionalization of carbon nanotubes. *Synth. Met.* **141**, 113–122 (2004).

84. Wang, H. & Xu, J. Theoretical evidence for a two-step mechanism in the functionalization single-walled carbon nanotube by aryl diazonium salts:

Comparing effect of different substituent group. *Chem. Phys. Lett.* **477**, 176–178 (2009).

85. Hilmer, A. J. *et al.* Role of adsorbed surfactant in the reaction of aryl diazonium salts with single-walled carbon nanotubes. *Langmuir* **28**, 1309–1321 (2012).

86. Högele, A., Galland, C., Winger, M. & Imamoğlu, A. photon antibunching in the photoluminescence spectra of a single carbon nanotube. *Phys. Rev. Lett.* **100**, 217401 (2008).

87. Chen, J. *et al.* Bright infrared emission from electrically induced excitons in carbon nanotubes. *Science.* **310**, 1171–1174 (2005).

88. Heller, D. a., Baik, S., Eurell, T. E. & Strano, M. S. Single-walled carbon nanotube spectroscopy in live cells: Towards long-term labels and optical Sensors. *Adv. Mater.* **17**, 2793–2799 (2005).

89. Crochet, J., Clemens, M. & Hertel, T. Quantum yield heterogeneities of aqueous single-wall carbon nanotube suspensions. *J. Am. Chem. Soc.* **129**, 8058–8059 (2007).

90. Nozik, A. J. Spectroscopy and hot electron relaxation dynanics in semiconductor quantum wells and quantum dots. *Annu. Rev. Phys. Chem.* **52**, 193–231 (2001).

91. Lee, A. J. *et al.* Bright fluorescence from individual single-walled carbon nanotubes. *Nano Lett.* **11**, 1636–1640 (2011).

92. Ando, T. Effects of valley mixing and exchange on excitons in carbon nanotubes with aharonov-bohm flux. *J. Phys. Soc. Japan* **75**, 024707 (2006).

93. Capaz, R., Spataru, C., Ismail-Beigi, S. & Louie, S. Diameter and chirality dependence of exciton properties in carbon nanotubes. *Phys. Rev. B* **74**, 121401 (2006).

94. Spataru, C., Ismail-Beigi, S., Capaz, R. & Louie, S. Theory and ab initio calculation of radiative lifetime of excitons in semiconducting carbon nanotubes. *Phys. Rev. Lett.* **95**, 247402 (2005).

95. Zhao, H. & Mazumdar, S. Electron-electron interaction effects on the optical excitations of semiconducting single-walled carbon nanotubes. *Phys. Rev. Lett.* **93**, 157402 (2004).

96. Scholes, G. D. *et al.* Low-lying exciton states determine the photophysics of semiconducting single wall carbon nanotubes. *J. Phys. Chem. C* **111**, 11139–11149 (2007).

97. Karousis, N., Tagmatarchis, N. & Tasis, D. Current progress on the chemical modification of carbon nanotubes. *Chem. Rev.* **110**, 5366–97 (2010).

98. Peng, B. X. & Wong, S. S. Functional covalent chemistry of carbon nanotube surfaces. *Adv. Mater.* **21**, 625–642 (2009).

99. Ghosh, S., Bachilo, S. M., Simonette, R. a, Beckingham, K. M. & Weisman, R. B. Oxygen doping modifies near-infrared band gaps in fluorescent single-walled carbon nanotubes. *Science* **330**, 1656–1659 (2010).

100. Cognet, L. *et al.* Stepwise quenching of exciton fluorescence in carbon nanotubes by single-molecule reactions. *Science* **316**, 1465–1468 (2007).

101. Harutyunyan, H. *et al.* Defect-induced photoluminescence from dark excitonic states in individual single-walled carbon nanotubes. *Nano Lett.* **9**, 2010–2014 (2009).

102. Kilina, S., Ramirez, J. & Tretiak, S. Brightening of the lowest exciton in carbon nanotubes via chemical functionalization. *Nano Lett.* **12**, 2306–2312 (2012).

103. Zhang, Y. *et al.* Propagative Sidewall Alkylcarboxylation that Induces red-shifted near-IR photoluminescence in single-walled carbon nanotubes. *J. Phys. Chem. Lett.* **4**, 826–830 (2013).

104. Deng, S. *et al.* Confined propagation of covalent chemical reactions on single-walled carbon nanotubes. *Nat. Commun.* **2**, 382 (2011).

105. Dresselhaus, M. S., Dresselhaus, G. & Jorio, a. Raman spectroscopy of carbon nanotubes in 1997 and 2007. *J. Phys. Chem. C* **111**, 17887–17893 (2007).

106. Blackburn, J. L., Holt, J. M., Irurzun, V. M., Resasco, D. E. & Rumbles, G. confirmation of K-momentum dark exciton vibronic sidebands using 13C-

labeled, highly enriched (6,5) single-walled carbon nanotubes. *Nano Lett.* **12**, 1398–403 (2012).

107. Torrens, O., Zheng, M. & Kikkawa, J. Energy of K-momentum dark excitons in carbon nanotubes by optical spectroscopy. *Phys. Rev. Lett.* **101**, 157401 (2008).

108. Corwin Hansch, A. Leo, R. W. T. A Survey of hammett substituent constants and resonance and field parameters. *Chem. Rev.* **91**, 165–195 (1991).

109. J. L. Bredas, A. J. H. Influence of donor and acceptor substituents on the electronic characteistics of poly(paraphenylene vinylene) and poly(paraphenylene). *Chem. Phys. Lett.* **217**, 507–512 (1994).

110. Ramirez, J., Mayo, M. L., Kilina, S. & Tretiak, S. Electronic structure and optical spectra of semiconducting carbon nanotubes functionalized by diazonium salts. *Chem. Phys.* **413**, 89–101 (2013).

111. Engel, M. *et al.* Thin film nanotube transistors based on self-assembled, aligned, semiconducting carbon nanotube arrays. *ACS Nano* **2**, 2445–2452 (2008).

112. Kim, Y. a. *et al.* Thermal stability and structural changes of double-walled carbon nanotubes by heat treatment. *Chem. Phys. Lett.* **398**, 87–92 (2004).

113. Peng, B. *et al.* Measurements of near-ultimate strength for multiwalled carbon nanotubes and irradiation-induced crosslinking improvements. *Nat. Nanotechnol.* **3**, 626–631 (2008).

114. Green, A. a & Hersam, M. C. Properties and application of double-walled carbon nanotubes sorted by outer-wall electronic type. *ACS Nano* **5,** 1459–1467 (2011).

115. Villalpando-Paez, F. *et al.* Raman spectroscopy study of isolated double-walled carbon nanotubes with different metallic and semiconducting configurations. *Nano Lett.* **8**, 3879–3886 (2008).

116. Kalbac, M., Green, A. a, Hersam, M. C. & Kavan, L. Tuning of sorted double-walled carbon nanotubes by electrochemical charging. *ACS Nano* **4**, 459–469 (2010).

117. Okada, S. & Oshiyama, A. Curvature-induced metallization of double-walled semiconducting zigzag carbon nanotubes. *Phys. Rev. Lett.* **91**, 216801 (2003).

118. Tison, Y., Giusca, C. E., Stolojan, V., Hayashi, Y. & Silva, S. R. P. The inner shell influence on the electronic structure of double-walled carbon nanotubes. *Adv. Mater.* **20**, 189–194 (2008).

119. Nair, N., Kim, W.-J., Usrey, M. L. & Strano, M. S. A structure-reactivity relationship for single walled carbon nanotubes reacting with 4-hydroxybenzene diazonium salt. *J. Am. Chem. Soc.* **129,** 3946–3954 (2007).

120. Bahr, J. L. *et al.* Functionalization of carbon nanotubes by electrochemical reduction of aryl diazonium salts: a bucky paper electrode. *J. Am. Chem. Soc.* **123,** 6536–6542 (2001).

121. An, L., Fu, Q., Lu, C. & Liu, J. A simple chemical route to selectively eliminate metallic carbon nanotubes in nanotube network devices. *J. Am. Chem. Soc.* **126,** 10520–10521 (2004).

122. Tsyboulski, D. a *et al.* Do inner shells of double-walled carbon nanotubes fluoresce? *Nano Lett.* **9,** 3282–3289 (2009).

123. Telg, H., Maultzsch, J., Reich, S. & Thomsen, C. Resonant-Raman intensities and transition energies of the E11 transition in carbon nanotubes. *Phys. Rev. B* **74,** 115415 (2006).

124. Maultzsch, J., Telg, H., Reich, S. & Thomsen, C. Radial breathing mode of single-walled carbon nanotubes: Optical transition energies and chiral-index assignment. *Phys. Rev. B* **72,** 205438 (2005).

125. Araujo, P. *et al.* Third and fourth optical transitions in semiconducting carbon nanotubes. *Phys. Rev. Lett.* **98,** 067401 (2007).

126. Filho, A. G. S. *et al.* Selective tuning of the electronic properties of coaxial nanocables through exohedral doping. *Nano Lett.* **7,** 2383–2388 (2007).

127. Hayashi, T. *et al.* Selective optical property modification of double-walled carbon nanotubes by fluorination. *ACS Nano* **2,** 485–488 (2008).

128. Brozena, A. H. *et al.* Outer wall selectively oxidized, water-soluble double-walled carbon nanotubes. *J. Am. Chem. Soc.* **132**, 3932–3938 (2010).

129. Khlobystov, A. N. Endohedral modification of carbon nanotubes. *Chem. Carbon Nanotub.* **3**, 87–111 (2008).

130. Mann, D., Javey, A., Kong, J., Wang, Q. & Dai, H. Ballistic transport in metallic nanotubes with reliable Pd ohmic contacts. *Nano Lett.* **3**, 1541–1544 (2003).

131. Collins, P., Hersam, M., Arnold, M., Martel, R. & Avouris, P. Current saturation and electrical breakdown in multiwalled carbon nanotubes. *Phys. Rev. Lett.* **86**, 3128–3131 (2001).

132. Bouilly, D. *et al.* Wall-selective probing of double- walled carbon nanotubes using covalent functionalization. *ACS Nano* **5**, 4927–4934 (2011).

133. Chung, J., Lee, K.-H., Lee, J., Troya, D. & Schatz, G. C. Multi-walled carbon nanotubes experiencing electrical breakdown as gas sensors. *Nanotechnology* **15**, 1596–1602 (2004).

134. Lu, W., Hartman, R., Qu, L. & Dai, L. Nanocomposite electrodes for high-performance supercapacitors. *J. Phys. Chem. Lett.* **2**, 655–660 (2011).

135. Kamat, P. V. Graphene-based nanoarchitectures. anchoring semiconductor and metal nanoparticles on a two-dimensional carbon support. *J. Phys. Chem. Lett.* **1**, 520–527 (2010).

136. Zhang, Y. & Wang, Y. Gold-substrate-enhanced scanning electron microscopy of functionalized single-wall carbon nanotubes. *J. Phys. Chem. Lett.* **2**, 885–888 (2011).

137. Dresselhaus, M. S. Fifty years in studying carbon-based materials. *Phys. Scr.***,** 014002 (2012).

138. Zhang, D., Yang, J. & Li, Y. Spectroscopic characterization of the chiral structure of individual single-walled carbon nanotubes and the edge structure of isolated graphene nanoribbons. *Small* **9**, 1284–304 (2013).

139. Krumer, Z. *et al.* Tackling self-absorption in luminescent solar concentrators with type-II colloidal quantum dots. *Sol. Energy Mater. Sol. Cells* **111**, 57–65 (2013).

140. Zhou, Z. *et al.* Engineered iron-oxide-based nanoparticles as enhanced T1 contrast agents for efficient tumor imaging. *ACS Nano* **7**, 3287–2396 (2013).

141. Park, H. *et al.* High-density integration of carbon nanotubes via chemical self-assembly. *Nat. Nanotechnol.* **7**, 787–791 (2012).

142. Li, J. *et al.* Growth of high-density-aligned and semiconducting-enriched single-walled carbon nanotubes : decoupling the conflict between density and selectivity. *ACS Nano* **1**, 554-562 (2013).

143. Huang, J. *et al.* Covalently functionalized double-walled carbon nanotubes combine high sensitivity and selectivity in the electrical detection of small molecules. *J. Am. Chem. Soc.* **135**, 2306–2312 (2013).

144. Piao, Y. *et al.* Optical and electrical properties of inner tubes in outer wall-selectively functionalized double-wall carbon nanotubes. *J. Phys. Chem. Lett.* **2**, 1577–1582 (2011).

145. Fujisawa, K. *et al.* Chirality-dependent transport in double-walled carbon nanotube assemblies: the role of inner tubes. *ACS Nano* **5**, 7547–7554 (2011).

146. Mandal, H. S., Ward, A. & Tang, X. S. Transferable thin films of pristine carbon nanotubes. *J. Nanosci. Nanotechnol.* **11**, 3265–3272 (2011).

147. Wang, Q. H. & Strano, M. S. Carbon nanotubes: A bright future for defects. *Nat. Chem.* **5**, 812–813 (2013).

148. Ricci, A. M., Méndez De Leo, L. P., Williams, F. J. & Calvo, E. J. Some evidence for the formation of an azo bond during the electroreduction of diazonium salts on Au substrates. *Chem. Phys. Chem.* **13**, 2119–2127 (2012).

149. Hong, G. *et al.* In vivo fluorescence imaging with Ag 2 S quantum dots in the second near-infrared region. *Angew. Chemie* **124**, 9956–9959 (2012).

150. Kosuge, H. *et al.* Near infrared imaging and photothermal ablation of vascular inflammation using single-walled carbon nanotubes. *J. Am. Heart Assoc.* **1**, e002568 (2012).

151. Yang, S., Parks, A. N., Saba, S. a, Ferguson, P. L. & Liu, J. Photoluminescence from inner walls in double-walled carbon nanotubes: some do, some do not. *Nano Lett.* **11**, 4405–4410 (2011).

152. Gohier, A. *et al.* Tunable grafting of functional polymers onto carbon nanotubes using diazonium chemistry in aqueous media. *J. Mater. Chem.* **21**, 4615 (2011).

153. Shulaker, M. M. *et al.* Carbon nanotube computer. *Nature* **501**, 526–530 (2013).

154. Chen, P. *et al.* Fully printed separated carbon nanotube thin film transistor circuits and its application in organic light emitting diode control. *Nano Lett.* 5301–5308 (2011).